
Louisiana Transportation Research Center

Final Report 609

Live Load Monitoring of the I-10 Twin Span Bridge

by

Steve C.S. Cai, Ph.D., P.E. (MD)

Yang Yu, Research Assistant

Louisiana State University



4101 Gourrier Avenue | Baton Rouge, Louisiana 70808
(225) 767-9131 | (225) 767-9108 fax | www.ltrc.lsu.edu

TECHNICAL REPORT STANDARD PAGE

1. Report No. FHWA/LA.17/609		2. Government Accession No.	3. Recipient's Catalog No.
4. Title and Subtitle Live Load Monitoring of the I-10 Twin Span Bridge		5. Report Date January 2020	
		6. Performing Organization Code LTRC Project Number: 13-2ST State Project Number: 30001123	
7. Author(s) Steve Cai, Ph.D., P.E. (MD) Yang Yu, Research Assistant		8. Performing Organization Report No.	
9. Performing Organization Name and Address Department of Civil and Environmental Engineering Louisiana State University Baton Rouge, LA 70803		10. Work Unit No.	
		11. Contract or Grant No.	
12. Sponsoring Agency Name and Address Louisiana Department of Transportation and Development P.O. Box 94245 Baton Rouge, LA 70804-9245		13. Type of Report and Period Covered Final Report Aug. 2014-May 2017	
		14. Sponsoring Agency Code	
15. Supplementary Notes Conducted in Cooperation with the U.S. Department of Transportation, Federal Highway Administration			
16. Abstract The reduction of capacity caused by the deterioration of materials and the increasing traffic volumes have raised serious safety concerns for field bridges. The main objective of this project is to develop a strategy for truck characterization and develop a methodology for performance assessment of the instrumented bridge. To achieve the research objective, a methodology is developed including three parts: (1) bridge condition assessment based on strain monitoring where the Bayesian theory is used to predict live load effect based on monitored strains, (2) framework for bridge condition assessment where the measured and predicted strains are compared with the developed service and capacity envelopes, and (3) live load monitoring using the current instrumentation system where a strategy to identify vehicle information is explored. Using the developed methodology, condition assessment of the I-10 Twin Span Bridge is conducted. It is found that the bridge is safe and performing as designed. Nevertheless, results also indicate that the exterior girders under the slow lane could be overstressed in the future. The developed methodology can be adopted for long-term performance assessment for other field bridges in order to more accurately account for the traffic effects, which can help reduce the uncertainty and achieve more reliable condition assessment of bridges for bridge maintenance decision-making.			
17. Key Words Live load effect monitoring; Bridge condition assessment; Bridge weigh-in-motion		18. Distribution Statement Unrestricted. This document is available through the National Technical Information Service, Springfield, VA 21161.	
19. Security Classif. (of this report) N/A	20. Security Classif. (of this page) N/A	21. No. of Pages 142	22. Price

Project Review Committee

Each research project will have an advisory committee appointed by the LTRC Director. The Project Review Committee is responsible for assisting the LTRC Administrator or Manager in the development of acceptable research problem statements, requests for proposals, review of research proposals, oversight of approved research projects, and implementation of findings.

LTRC appreciates the dedication of the following Project Review Committee Members in guiding this research study to fruition.

LTRC Administrator/ Manager

Walid Alaywan, Ph.D., PE
Structures Research Manager

Members

Arthur D'Andrea	DOTD Bridge Design Section
Holly Thomas	DOTD Bridge Design Section
David Miller	DOTD Bridge Maintenance Section
Art Aguirre	FHWA-Louisiana Office

Directorate Implementation Sponsor

Christopher P. Knotts, P.E.
DOTD Chief Engineer

Live Load Monitoring of the I-10 Twin Span Bridge

by

Steve C.S. Cai, Ph.D., P.E. (MD)

Yang Yu, Research Assistant

Department of Civil Engineering

Louisiana State University

Baton Rouge, Louisiana 70803

LTRC Project No. 13-2ST

State Project No. 30001123

conducted for

Louisiana Department of Transportation and Development

Louisiana Transportation Research Center

The contents of this report reflect the views of the author/principal investigator who is responsible for the facts and the accuracy of the data presented herein. The contents do not necessarily reflect the views or policies of the Louisiana Department of Transportation and Development or the Louisiana Transportation Research Center. This report does not constitute a standard, specification, or regulation.

January 2020

ABSTRACT

The reduction of capacity caused by the deterioration of materials and the increasing traffic volumes have raised serious safety concerns for field bridges. The main objective of this project is to develop a strategy for truck characterization and develop a methodology for performance assessment of the instrumented bridge. To achieve the research objective, a methodology is developed including three parts: (1) bridge condition assessment based on strain monitoring where the Bayesian theory is used to predict live load effect based on monitored strains, (2) framework for bridge condition assessment where the measured and predicted strains are compared with the developed service and capacity envelopes, and (3) live load monitoring using the current instrumentation system where a strategy to identify vehicle information is explored. Using the developed methodology, condition assessment of the I-10 Twin Span Bridge is conducted. It is found that the bridge is safe and performing as designed. Nevertheless, results also indicate that the exterior girders under the slow lane could be overstressed in the future. The developed methodology can be adopted for long-term performance assessment for other field bridges in order to more accurately account for the traffic effects, which can help reduce the uncertainty and achieve more reliable condition assessment of bridges for bridge maintenance decision-making.

ACKNOWLEDGMENTS

The investigators are grateful to the Federal Highway Administration, the Louisiana Transportation Research Center (LTRC), and the Louisiana Department of Transportation and Development (DOTD) for funding this project. The contents of this report reflect only the views of the authors who are responsible for the facts and the accuracy of the data presented herein. The authors would like to thank those who provided help during the development of the initial tasks of this research program. Special thanks go to the project manager Walid Alaywan, Ph.D., the Geocomp company, and graduate students at Louisiana State University (LSU) for their hard work during the implementation of this project

IMPLEMENTATION STATEMENT

The findings from this study provide insight into the performance of the instrumented field bridge under site specific live loads. Based on the condition assessment results, the I-10 Twin Span Bridge is currently safe and performing as designed. Nevertheless, results also indicate that the exterior girders under the slow lane could be overstressed in the future. The developed methodology can be adopted for long-term performance assessment for other field bridges in order to more accurately account for the traffic effects, which can help reduce the uncertainty and achieve more reliable condition assessment of bridges for bridge maintenance decision-making.

TABLE OF CONTENTS

ABSTRACT	iii
ACKNOWLEDGMENTS	v
IMPLEMENTATION STATEMENT	vii
TABLE OF CONTENTS	ix
LIST OF TABLES	xi
LIST OF FIGURES	xiii
INTRODUCTION	1
OBJECTIVE	5
SCOPE	7
METHODOLOGY	9
Bridge Condition Assessment Based on Strain Monitoring	9
Bayesian Method for Extreme Value Analysis	9
Framework for Bridge Condition Assessment	14
Live Load Monitoring Using the Current Instrumentation System	16
Identification of the Vehicle's Longitudinal Position	16
Identification of the Vehicle's Transverse Position	17
Identification of the Vehicle's Axle Weight and GVW	19
DISCUSSION OF RESULTS	21
Condition Assessment of the I-10 Twin Span Bridge	21
Bridge and Instrumentation Description	21
Analysis of Monitoring Data	23
Prediction of Extreme Traffic LEs	24
Bridge Condition Assessment	33
Live Load Monitoring through Nothing-on-road BWIM	38
Numerical Simulation	38
Simulation Results	43
2D BWIM Algorithm	51
Verification by a Field Study	63
CONCLUSIONS	69
RECOMMENDATIONS	71
ACRONYMS, ABBREVIATIONS, AND SYMBOLS	71
REFERENCES	73
APPENDIX I	79
Review on Bridge Weigh-in-motion Technology	79
APPENDIX II	79
Sample Time History of Sensors	79

LIST OF TABLES

Table 1 Prediction results for the steel span using Bayesian method	29
Table 2 Prediction results for the concrete span using Bayesian method.....	30
Table 3 Calculation of design live load capacity of the steel and concrete span.....	34
Table 4 FE model calibration parameters	35
Table 5 Maximum measured stress and LE envelops for the steel span	36
Table 6 Maximum measured stress and LE envelops for the concrete span	36
Table 7 Axle configurations of truck models	39
Table 8 Identified results using wavelet transformation.....	45
Table 9 Identification errors using wavelet transformation.....	45
Table 10 Description of loading cases considered in the simulation.....	52
Table 11 Identification results using the proposed algorithm.....	55
Table 12 Comparison of identification errors between the Moses’s algorithm and the proposed algorithm	57
Table 13 Identification errors for Case 5 with Truck 4 traveling under different road surface conditions.....	59
Table 14 Identification errors for Case 5 with Truck 4 traveling under different road surface conditions using filtered responses	59
Table 15 Identification errors for Case 2 with Truck 2 traveling at different vehicle speeds	60
Table 16 Identification errors for Case 6 with Truck 2 using different vehicle widths.....	61
Table 17 Identification errors for Case 1 with Truck 2 using different weighing stations	63
Table 18 Description of testing cases	65
Table 19 Identification results and corresponding errors	66
Table 20 General layout schemes of BWIM sensors for typical bridges types	89

LIST OF FIGURES

Figure 1 Overall layout of WIM system	2
Figure 2 Flow chart of the framework for bridge condition assessment	15
Figure 3 Damaged original twin span and the new Twin Span: (a) original twin span bridge damaged by Hurricane Katrina; (b) the new I-10 Twin Span bridge	21
Figure 4 Instrumentation of the I-10 Twin Span Bridge; (a) longitudinal profile of instrumented spans; (b) sensor layout of the steel span (with traffic flow at mid- span); (c) sensor layout of the concrete span (with traffic flow at mid-span); (d) M19 pier	22
Figure 5 Sample time history of strain response at S4: (a) measured and temperature- induced strains; (b) traffic-induced strain	24
Figure 6 Normalized histogram of daily maxima of S4 and the corresponding GEV fit	24
Figure 7 Trace plots of GEV parameters	26
Figure 8 Marginal posterior distributions of the GEV distribution parameters: (a) shape parameter; (b) scale parameter; (c) location parameter	27
Figure 9 Distribution of 5-year and 75-year return levels of S4.....	27
Figure 10 Predictive distribution and fitted GEV distribution of S4.....	28
Figure 11 Prediction of maximum LEs of S4.....	29
Figure 12 Variation of measured and predicted maximum stresses with respect to sensor locations: (a) steel span; (b) concrete span	30
Figure 13 Typical stress responses of the concrete span at sensor C2.....	31
Figure 14 Distribution of daily maximum LEs: (a) S2; (b) S5	32
Figure 15 Marginal posterior distributions of shape parameters: (a) S2; (b) S5	32
Figure 16 FE models of the bridge: (a) the steel span; (b) the concrete span.....	35
Figure 17 Amplitude spectra of strain responses: (a) the steel span; (b) the concrete span ..	35
Figure 18 Assessment of current condition: (a) steel span; (b) concrete span.....	37
Figure 19 Assessment of future condition for the steel span: (a) 5-year; (b) 75-year	38
Figure 20 Assessment of future condition for the concrete span: (a) 5-year; (b) 75-year	38
Figure 21 Analytical model of the adopted truck	39
Figure 22 Cross section of the bridge used in the simulation	40
Figure 23 Finite element model of the bridge used in the simulation	40
Figure 24 Location of the measurement stations and traffic lanes	42
Figure 25 Contour plots of numerically calibrated influence surfaces: (a) S2; (b) S5 (unit: microstrain)	43
Figure 26 Typical strain signals and corresponding wavelet transformations at scale of 14: (a) Truck 2 (3-axle) traveling at 20 m/s and (b) Truck 4 (5-axle) traveling at 10	

m/s.....	44
Figure 27 Wavelet transformations of signals for Truck 3 traveling at 30 m/s: (a) sampling frequency of 200 Hz; (b) sampling frequency of 500 Hz	47
Figure 28 Wavelet transformations of signals under different road surface conditions	49
Figure 29 Wavelet transformations of signals under different levels of noise: (a) sampling frequency of 500 Hz; (b) sampling frequency of 200 Hz	51
Figure 30 Variation of the error function with respect to the possible TPs of the vehicle: (a) Case 2 with Truck 4; (b) Case 4 with Truck 1	52
Figure 31 Simulated and reconstructed bridge responses of different measurement stations for Case 2 with Truck 4: (a) S1; (b) S2; (c) S3; (d) S4; (e) S5	54
Figure 32 Variation of identification errors of axle weights and GVW with respect to the vehicle width for Case 6 with Truck 2.....	62
Figure 33 Longitudinal profile of the tested bridge.....	63
Figure 34 Cross section and lane arrangement of the tested bridge	64
Figure 35 The test vehicle.....	64
Figure 36 Contour plots of field calibrated influence surfaces: (a) S4; (b) S6 (unit: microstrain)	65
Figure 37 Comparison between the measured and reconstructed bridge responses of the weighing station: (a) Case 4; (b) Case 6	67
Figure 38 Weigh stations on the highway.....	80
Figure 39 The framework of BWIM and its applications.....	80
Figure 40 Components of an SiWIM system: (1) FAD sensors, (2) spider, (3) weighing sensors, (4) cabinet and panel, (5) batteries, (6) solar panels, (7) solar panel installation, (8) antenna, (9) camera, (10) PDA [30].....	85
Figure 41 Typical FAD signals of a five-axle truck crossing [30].....	87
Figure 42 Sensor layouts of a typical BWIM system (cm)[30].....	91
Figure 43 Pre-selection of overloaded trucks using pavement-based WIM [25].....	92
Figure 44 A typical WIM-based toll booth [43].....	93
Figure 45 Concept of WIM-based SHM [64]	96
Figure 46 Daily average EBWIM for different damage cases [64].....	96
Figure 47 Concept of the VA for damage detection [65].....	97
Figure 48 Inferred axle force for the same vehicle at health and damaged state of the bridge [66].....	98
Figure 49 Framework of the damage detection method proposed by [67].....	98
Figure 50 Sensor locations for the monitored spans of the I-10 Twin Span Bridge.....	79

INTRODUCTION

Overloaded trucks often cause serious damage and safety threats to bridges. Compared to the standard design traffic/live loads in the design specifications such as AASHTO HL 93 [1], the actual characteristics of overloaded trucks, such as truck weight and types, are very difficult to be predicted or defined in advance because they are site specific. Therefore, it is important to investigate the characteristics of overloaded trucks and their actual impact on bridges that were typically designed against the standard design traffic loads.

Bridge condition assessment and live load capacity evaluation are the principal components of the Federal Highway Administration's (FHWA) National Bridge Inspection Program (NBIP). The objective of the NBIP program is to more accurately evaluate bridge capacity in order to ensure the safety of traveling public. Accurate bridge load rating is also an important factor for decision-making regarding bridge rehabilitation/replacement, load posting, and overload truck permitting.

The American Association of State Highway and Transportation Officials (AASHTO) published the first edition of *Manual for Bridge Evaluation* (MBE) in 2008 to ensure the safety and serviceability of highway bridges. Louisiana Department of Transportation and Development (DOTD) implemented the MBE Load and Resistant Factor Rating (LRFR) methodology in 2009. The intent of LRFR is to be consistent with Load and Resistance Factor Design (LRFD) Specifications using a reliability-based philosophy and to extend the provisions of the LRFD Specifications to the areas of inspection, load rating, posting, and permitting of existing bridges [1]. In the LRFR methodology, structural performance is measured in terms of the reliability index, β . Though the LRFD specifications have been calibrated to provide a more uniform and acceptable level of safety and reliability, the application of reliability theory to bridge load rating is much more complex than the application of these principles in design due to site-specific conditions and time-dependent variations of existing bridges in service. In general, the bridge reliability index decreases with time due to deterioration, accident, fatigue and growing traffic. For a specific bridge, knowledge of the in situ traffic data, performance data, and material and dimension data will greatly reduce the uncertainties. Incorporating those data into bridge load rating will greatly increase the reliability index β and extend the operational life of bridges.

To establish a site-specific database for bridge evaluation and future bridge design, DOTD established a long-term health monitoring system at the I-10 Twin Span Bridge. As stated in the Request for Proposal (RFP), DOTD, through its contractor Geocomp Corporation, has installed a comprehensive health monitoring system at Pier M19 of the eastbound lanes. The

bridge is instrumented from deck to piles to capture bridge response (both substructure and superstructure) to live loads. The purpose of this instrumentation is to perform structural health monitoring (SHM) of the bridge during normal and regular traffic events as well as during extreme events, overloads, wave surges or ship collision. The proposed study is to provide field data-based supports to DOTD to fully implement the health monitoring system and determine the effects of traffic loads on instrumented components of the structure. In addition to instrumentations for structural response such as strains, an OSMOS weigh-in-motion (WIM) system has been installed adjacent to M19 to collect live load information, as shown in Figure 1(a) [2]. The OSMOS' WIM uses optical extensometers that are placed vertically nearby the bearings to measure the dynamic deformations caused by the impact of crossing traffic (Figure 1 (b)). This dynamic impact measurement is then used to weigh the traffic. The OSMOS monitoring station connected to the optical sensors collects and processes the signal to computerize the monitoring through its dashboard displays. The entire system is configured online to monitor real-time load data. The on-site monitoring station can synchronize the sensors and video information and upload it to an offsite server for real-time data processing (Figure 1(c)).

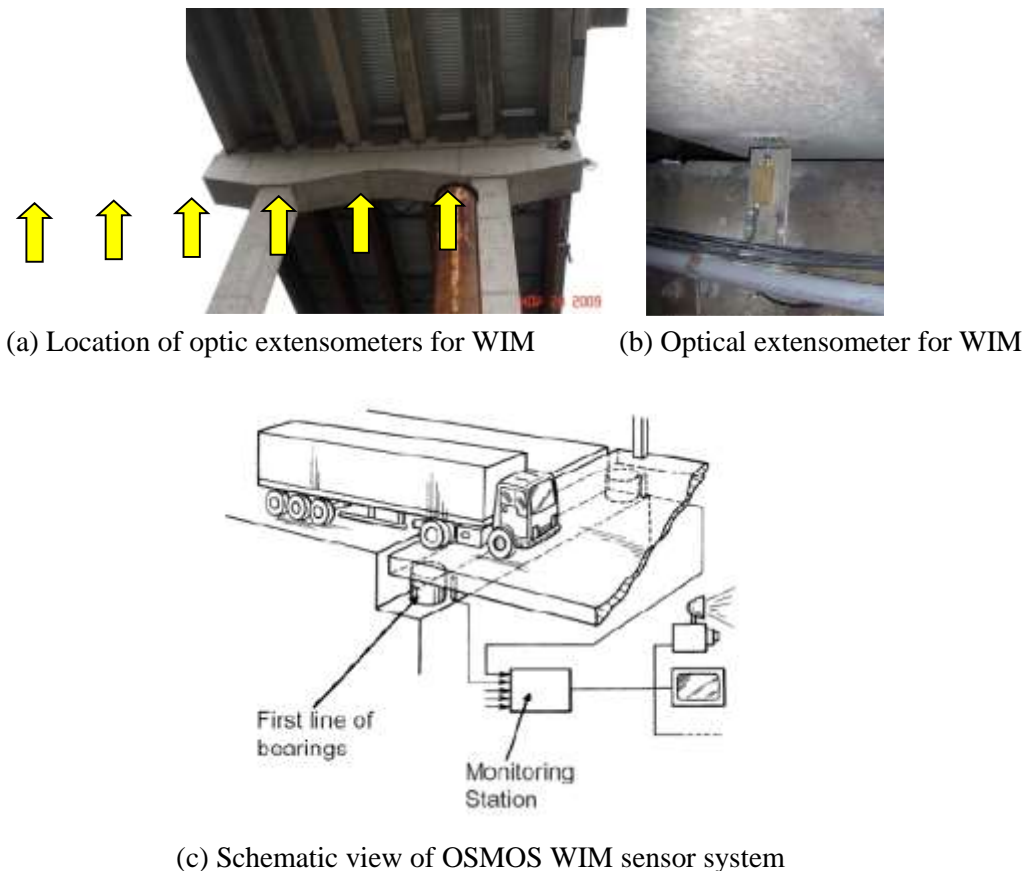


Figure 1
Overall layout of WIM system

By fully utilizing these instrumentations and field data resources, this project can be further used to develop a methodology to accurately evaluate the bridge reliability/safety based on the in-situ WIM data, live load testing data, long-term health monitoring data, and refined finite element models. To serve this purpose, the researchers of this proposed research project must have expertise in a deep understanding of bridge field instrumentation and testing, statistically characterizing and presenting the data in a useful and convenient format, and carrying out bridge performance evaluation and rating. The end goal will be to achieve a precise continuous real-time load rating which in turn will be used for load permitting and bridge maintenance. Therefore, the results of the proposed research will be directly implemented into the DOTD practice of bridge design and capacity rating, which is of great significance to the DOTD.

OBJECTIVE

The objectives of this project are the following:

1. Develop a data interface tool for data processing.
2. Develop a strategy for truck characterization.
3. Determine the effects of traffic loads on the instrumented components of the bridge.
4. Develop a methodology for performance assessment of the instrumented bridge.

SCOPE

The bridge selected for this study is the new I-10 Twin Span Bridge (TSB) located in southern Louisiana. The bridge was instrumented with strain gages for both the superstructure and the substructure. The main effort of this research is to validate the bridge performance monitoring system that is capable of capturing the live load information and its effects on the performance of the instrumented bridge components, through developing data interface tools. The tasks of this research includes literature review, assessing the existing instrumentation, collecting and processing data, analyzing data, developing a methodology to assess the performance of the bridge, and prediction of the future performance of the bridge using the developed strategy.

METHODOLOGY

The methodology developed in the present study includes three parts: (1) bridge condition assessment based on strain monitoring where the Bayesian theory is used to predict live load effect based on monitored strains, (2) framework for bridge condition assessment where the measured and predicted strains are compared with the developed service and capacity envelopes, and (3) live load monitoring using the current instrumentation system where a strategy to identify vehicle information is explored.

Bridge Condition Assessment Based on Strain Monitoring

Bayesian Method for Extreme Value Analysis

Modeling of Extreme Data. For a sequence of independent and identically (i.i.d.) distributed random variables (X_1, X_2, \dots, X_n) whose cumulative distribution function (CDF) is $F(x)$, let $M_n = \text{Max}(X_1, X_2, \dots, X_n)$ and the CDF of M_n can then be expressed as:

$$F_{M_n}(x) = P(M_n < x) = P(X_1 < x, X_2 < x, \dots, X_n < x) = F^n(x) \quad (1)$$

Based on the Fisher-Tippett-Gnedenko theorem, if there exists a sequence of real numbers (a_n, b_n) with $a_n > 0$ such that

$$\lim_{n \rightarrow \infty} P\left(\frac{M_n - b_n}{a_n} < x\right) = G(x) \quad (2)$$

where, $G(x)$ is a non-degenerate distribution function, then $G(x)$ must be in the form of the generalized extreme value (GEV) distribution whose CDF can be written as [3]:

$$G(x) = \exp\left\{-\left[1 + k\left(\frac{x - \mu}{\sigma}\right)\right]^{-1/k}\right\} \quad (3)$$

where, k is the shape parameter; σ is the scale parameter; and μ is the location parameter. The GEV distribution contains three types of extreme value distributions depending on the value of the shape parameter: (1) when $k > 0$, $G(x)$ corresponds to the heavy-tailed (Fréchet) distribution; (2) when $k < 0$, $G(x)$ corresponds to the short-tailed (Weibull) distribution; and (3) when k approaches to 0, $G(x)$ corresponds to the light-tailed (Gumbel) distribution.

In order to model the extreme traffic LEs using the extreme value theory, the maximum traffic LEs are assumed to be i.i.d. The maximum traffic LEs are obtained using the block maxima method where the observation is divided into non-overlapping time intervals

(blocks) of equal length and then the maximum traffic LE in each block is extracted. Based on the extreme value theory, the block maxima will converge to the GEV distribution.

In extreme value analysis, the future extreme is predicted by computing the return level corresponding to a certain return period. Under the i.i.d. assumption, the return level corresponding to a certain return period has an equal probability of exceedance in any block. Therefore, the return level can be calculated as the quantile of the GEV distribution:

$$x_{RL} = \mu + \frac{\sigma}{k} \times \left\{ \left[-\ln \left(1 - \frac{t}{T} \right) \right]^{-k} - 1 \right\} \quad (4)$$

where, t is the block length and T is the return period. The reliability of the prediction is affected by the block length because the return level is usually obtained at the tail region of the distribution where the distribution is typically less accurate. For example, if the block length is chosen as one day, then the 50-year return level corresponds to approximately 0.9999452 quantile of the distribution of the daily maximum LE, which would require very high precision of the daily maximum LE distribution. From this perspective, increasing the block length will make the prediction more reliable. Meanwhile, the data sample size should also be considered when choosing the block length as an overly large block length would render the effective data size too small. Besides, the reliability of long-term predictions needs to be taken into consideration during the decision making process.

For a conventional extreme value analysis, the block maxima data is first fitted to the GEV distribution and the point estimates of the distribution parameters are obtained using the maximum likelihood estimation (MLE). Then, the prediction can be made by computing the return levels using equation (4).

Bayesian Inference. Based on the Bayes theorem, the posterior distribution of the parameters to be inferred can be written as:

$$p(\boldsymbol{\theta} | \mathbf{x}) = \frac{L(\boldsymbol{\theta} | \mathbf{x})p(\boldsymbol{\theta})}{\int L(\boldsymbol{\theta} | \mathbf{x})p(\boldsymbol{\theta})d\boldsymbol{\theta}} \quad (5)$$

where, $\boldsymbol{\theta}$ is the parameters to be inferred; $p(\boldsymbol{\theta} | \mathbf{x})$ is the posterior distribution; \mathbf{x} is the data; $p(\boldsymbol{\theta})$ is the prior distribution of the parameters; and $L(\boldsymbol{\theta} | \mathbf{x})$ is the likelihood function that can be expressed as:

$$L(\boldsymbol{\theta} | \mathbf{x}) = \prod_{i=1}^{N_i} p(x_i | \boldsymbol{\theta}) \quad (6)$$

where, x_i is the value for the i th observation and N_i is the number of observations.

In Bayesian statistics, the prior distribution represents the prior knowledge of the parameters and it is independent from the existing observations. Generally speaking, the prior distribution can be classified into two types, i.e., the informative prior and the non-informative prior. The informative prior is specified based on the prior knowledge that is usually obtained from the previous studies and the knowledge of experts. A well-specified informative prior can help reduce the uncertainty of parameters and lead to more efficient Markov Chain Monte Carlo (MCMC) sampling. Nevertheless, the prior knowledge may be difficult to express in terms of probability distributions and it often contains a certain degree of subjectivity. The non-informative prior, on the other hand, is adopted when little or no prior knowledge of the parameters is known. The non-informative prior usually features a flat distribution to represent the lack of knowledge. For example, a uniform distribution with a wide support or a normal distribution with a large variance is commonly used as the non-informative prior. In addition, it is noted that there exist conjugate priors for some distribution families. The use of conjugate priors is convenient as it avoids using the MCMC sampling. However, the conjugate prior is not available for the GEV distribution [4].

In the present study, it is very difficult to elicit informative priors because the traffic LEs of bridges are highly site-specific due to the different traffic characteristics and bridge behaviors. Therefore, the non-informative prior is selected as the prior distribution. Three independent uniform distributions with wide supports are specified as the prior distribution as:

$$p(\boldsymbol{\theta}) = p(k)p(\sigma)p(\mu) \quad (7)$$

where, $p(k)$, $p(\sigma)$, and $p(\mu)$ are the prior distributions for the shape, scale, and location parameters, respectively. It should be noted that although the prior distributions are independent for each parameter, the obtained posterior distributions for each parameter will be dependent after the inference.

Markov Chain Monte Carlo (MCMC) Sampling. The denominator in equation (5) is a multi-dimensional integral that depends only on the data and its evaluation is often difficult. Nevertheless, the evaluation of this integral is usually not necessary since it can be treated as a normalizing constant and the posterior distribution can be written as:

$$p(\boldsymbol{\theta} | \mathbf{x}) \propto L(\boldsymbol{\theta} | \mathbf{x})p(\boldsymbol{\theta}) \quad (8)$$

The MCMC sampling can be used to directly sample from the posterior distribution using equation (8). In this study, the Metropolis-within-Gibbs (MG) sampler is adopted. The sampling procedures are described as follows:

1. Assigning initial values to the parameters: $\boldsymbol{\theta}^{(0)} = [k^{(0)} \ \sigma^{(0)} \ \mu^{(0)}]^T$ where k , σ , and μ are the shape, scale, and location parameters of the GEV distribution, respectively;

2. For $i=1:N$ (N =the number of iterations), first generate a candidate value for the shape parameter, k^* , from the normal proposal distribution conditional on $k^{(i-1)}$, i.e.,

$k^* \sim J(k^* | k^{(i-1)}) = N(k^{(i-1)}, s_k)$ where s_k is the scale of the proposal distribution. Then, calculate the acceptance ratio for k^* as:

$$\tau = \frac{f(k^* | \sigma^{(i-1)}, \mu^{(i-1)}, \mathbf{x})}{f(k^{(i-1)} | \sigma^{(i-1)}, \mu^{(i-1)}, \mathbf{x})} \quad (9)$$

where, $f(k | \sigma^{(i-1)}, \mu^{(i-1)}, \mathbf{x})$ is the non-normalized full conditional distribution of the shape parameter that is expressed as the product between the likelihood function and the prior distribution of the shape parameter as:

$$f(k | \sigma^{(i-1)}, \mu^{(i-1)}, \mathbf{x}) = L(k | \mathbf{x}, \sigma^{(i-1)}, \mu^{(i-1)}) = \prod_{i=1}^{N_i} p(x_i, \sigma^{(i-1)}, \mu^{(i-1)} | k) p(k) \quad (10)$$

Then, sample u from the uniform distribution $U(0,1)$; if $u < \min(1, \tau)$, accept k^* , i.e., $k^{(i)} = k^*$; otherwise, reject k^* , i.e., $k^{(i)} = k^{(i-1)}$;

3. Generate a candidate value for the scale parameter, σ^* , from the normal proposal distribution conditional on $\sigma^{(i-1)}$, i.e., $\sigma^* \sim J(\sigma^* | \sigma^{(i-1)}) = N(\sigma^{(i-1)}, s_\sigma)$ where s_σ is the scale of the proposal distribution. Then, calculate the acceptance ratio for σ^* as:

$$\tau = \frac{f(\sigma^* | k^{(i)}, \mu^{(i-1)}, \mathbf{x})}{f(\sigma^{(i-1)} | k^{(i)}, \mu^{(i-1)}, \mathbf{x})} \quad (11)$$

Similarly, $f(\sigma | k^{(i)}, \mu^{(i-1)}, \mathbf{x})$ is the non-normalized full conditional distribution of the scale parameter that is expressed as:

$$f(\sigma | k^{(i)}, \mu^{(i-1)}, \mathbf{x}) = \prod_{i=1}^{N_i} p(x_i, k^{(i)}, \mu^{(i-1)} | \sigma) p(\sigma) \quad (12)$$

Then, sample u from the uniform distribution $U(0,1)$; if $u < \min(1, \tau)$, accept σ^* , i.e., $\sigma^{(i)} = \sigma^*$; otherwise, reject σ^* , i.e., $\sigma^{(i)} = \sigma^{(i-1)}$;

4. Generate a candidate value for the location parameter, μ^* , from the normal proposal distribution conditional on $\mu^{(i-1)}$, i.e., $\mu^* \sim J(\mu^* | \mu^{(i-1)}) = N(\mu^{(i-1)}, s_\mu)$ where s_μ is the scale of the proposal distribution. Then, calculate the acceptance ratio for μ^* as:

$$\tau = \frac{f(\mu^* | k^{(i)}, \sigma^{(i)}, \mathbf{x})}{f(\mu^{(i-1)} | k^{(i)}, \sigma^{(i)}, \mathbf{x})} \quad (13)$$

Similarly, $f(\mu | k^{(i)}, \sigma^{(i)}, \mathbf{x})$ is the non-normalized full conditional distribution of the location parameter that is expressed as:

$$f(\mu | k^{(i)}, \sigma^{(i)}, \mathbf{x}) = \prod_{i=1}^{N_i} p(x_i, k^{(i)}, \sigma^{(i)} | \mu) p(\mu) \quad (14)$$

Then, sample u from the uniform distribution $U(0,1)$; if $u < \min(1, \tau)$, accept μ^* , i.e., $\mu^{(i)} = \mu^*$; otherwise, reject μ^* , i.e., $\mu^{(i)} = \mu^{(i-1)}$;

5. Repeat step 2 to 4 until i reaches N .

Following the above procedures, the parameter values generated by the MG sampler will asymptotically converge to the target distribution after a sufficient number of iterations. Nevertheless, the initial portion of the Markov Chain may not be a true realization from the target distribution because initial values of parameters have a significant influence on the initial portion. Therefore, in order to minimize the influence of the initial values, the initial portion of the Markov Chain is usually discarded and only the stabilized portion of the chain is used as the realization from the target distribution. The discarded portion is known as the burn-in period. Furthermore, the scale of the proposal distribution is a critical parameter that affects the sampling efficiency. On the one hand, if the scale is too small, then almost all proposed values will be accepted and the chain will move very slowly. On the other hand, if the scale is too large, then most proposed values will be rejected and the chain will hardly move at all. Both cases will cause the chain to mix poorly, leading to inefficient sampling. Thus, in order to achieve efficient sampling, the MG sampler needs to be tuned to obtain the optimal acceptance rate. For one-dimensional normal proposal distribution, the optimal acceptance rate was found to be approximately 0.44 [5].

Posterior Predictive Distribution. The ultimate goal of the extreme value analysis is the prediction of future extremes. In Bayesian statistics, the posterior predictive distribution is defined as:

$$p(y | \mathbf{x}) = \int p(y, \boldsymbol{\theta} | \mathbf{x}) d\boldsymbol{\theta} \quad (15)$$

where, y is the future outcome to be predicted. Since the future outcome is independent from the existing observations, the posterior predictive distribution can be rewritten based on the Bayes rule as:

$$p(y | \mathbf{x}) = \int p(y | \boldsymbol{\theta}) p(\boldsymbol{\theta} | \mathbf{x}) d\boldsymbol{\theta} \quad (16)$$

where, $p(y | \boldsymbol{\theta})$ is the GEV distribution and $p(\boldsymbol{\theta} | \mathbf{x})$ is the posterior distribution. Essentially, the posterior predictive distribution accounts for the parameter uncertainties by integrating the GEV distribution over all possible values of parameters specified by the posterior distribution. In fact, if the parameters are considered deterministic, then equation (16) becomes:

$$p(y | \mathbf{x}) = p(y | \boldsymbol{\theta}) \quad (17)$$

which is simply the case of the conventional method where point estimates of the parameters are adopted. Therefore, compared with the conventional method, the Bayesian method is able to incorporate the uncertainties inherent in the parameters into the prediction and provides more reliable estimate of future outcomes.

Framework for Bridge Condition Assessment

The objective of bridge condition assessment is to evaluate the performance of the bridge and check if the bridge can safely carry the operational loading. In order to achieve this objective, the response of the bridge needs to be measured first. Recent years have seen an increasing attention on the structural condition assessment via monitoring and the development of sensing technologies has facilitated the instrumentation of SHM systems. In SHM systems, sensors are installed at critical locations of the bridge to measure the typical responses such as the strain and acceleration. For bridge condition assessment, the maximum strain responses are probably the most important data since they can be used to determine the safety reserve of structural components [6]. In addition, while the measured responses of the bridge can be used to assess the current condition of the bridge, the bridge is designed to last for its design life and thus the future extreme responses of the bridge also need to be obtained to

assess the condition of the bridge during its remaining life. In this study, a framework of bridge condition assessment is proposed to evaluate the bridge condition at two levels. The flow chart for the proposed framework of bridge condition assessment is shown in Figure 2.

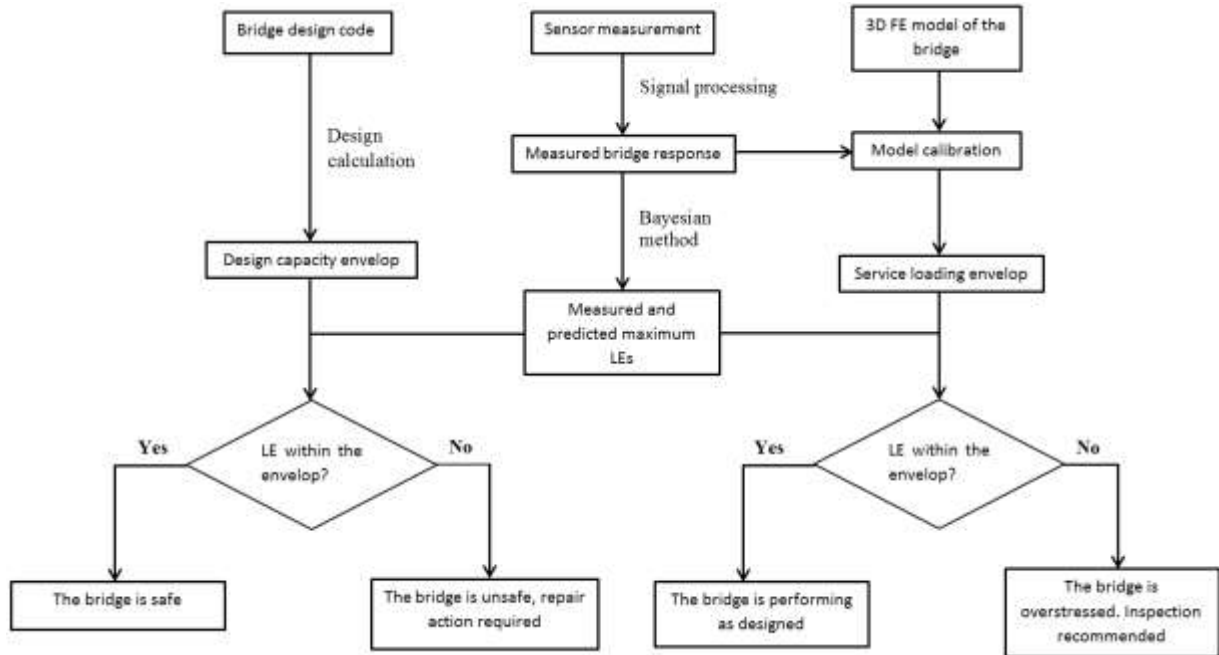


Figure 2
Flow chart of the framework for bridge condition assessment

After the measured and predicted bridge responses are obtained, they will be compared with the response envelops in order to determine the condition of the bridge. Two sets of response envelop are developed for two different loading levels. The first level is the ultimate loading level. The set of response envelops corresponding to this level reflects the capacity of the bridge that is determined based on the design codes and is thus named the design capacity envelop. The design capacity envelop should not be exceeded by the bridge response. Otherwise, the bridge will be severely damaged or even collapse. In this case, the bridge is considered unsafe and actions should be taken to repair and strengthen the bridge.

However, the design capacity of the bridge is usually considerably larger than the bridge response under the normal operational loading. This is because the bridge design capacity is determined for extreme loading conditions and bridge design codes are inevitably conservative due to the simplifications made during the design process and the requirement of covering a wide range of bridges. Therefore, comparing the bridge response with the design capacity envelops cannot reflect the expected bridge performance under the normal operational loading.

In order to see if the bridge under the assessment is performing as designed, another set of LE envelops, i.e., service LE envelop is developed. To determine the service loading envelop, the three-dimensional (3D) finite element (FE) model of the bridge is constructed. The 3D FE model can more accurately reflect the bridge behavior because it is specific to the bridge under the assessment and it avoids the design simplifications by the code by considering the spatial behavior of the bridge. By applying the design loading on the 3D FE model of the bridge, the set of service LE envelops can be obtained. The set of service LE envelops will be closer to the measured bridge response than the design capacity envelops and it can be used to evaluate the in-service performance of the bridge. If the bridge response is within the service loading envelops, then we can conclude that the bridge is performing as designed. Otherwise, the bridge is believed to be overstressed, which could either indicate that there exist structural damages or that the operational loading level is higher than expected. In this case, a bridge inspection is recommended to determine whether a repair is necessary.

Live Load Monitoring Using the Current Instrumentation System

Identification of the Vehicle's Longitudinal Position

Wavelet Theory. Fourier analysis allows the frequency information being extracted from the signal presented in the time domain. However, the time information is lost during the Fourier transformation (FT), i.e., it gives no information on the time occurrence of certain frequency components of the signal. In this sense, Fourier analysis is only suitable for stationary signals or cases where the time information is not of interest. To overcome this drawback, short-time Fourier analysis (STFT) was proposed [7]. The idea of the STFT is to divide the signal into many intervals and the signal in each small interval is assumed to be stationary. In this case, FT can be carried out at each time interval and a time-frequency representation of the signal can be obtained. However, the STFT is still not the perfect solution to analyze non-stationary signals since it has a fixed resolution, i.e., a satisfactory resolution with respect to both time and frequency cannot be achieved at the same time. Wavelet transformation was then developed on this basis to provide a multi-resolution analysis of the signal. The idea of the wavelet transformation is to expand the signal in terms of wavelets which are generated from dilations and translations with respect to the wavelet function that is compactly supported. An important feature of the wavelet transformation is that the width of the window can be changed to adapt to different frequency components of the signal. Therefore, wavelet analysis is very effective in analyzing non-stationary signals.

The continuous wavelet transformation (CWT) of a signal is defined as:

$$W_{\psi}(a, b) = \frac{1}{\sqrt{a}} \int_{-\infty}^{\infty} s(t) \psi\left(\frac{t-b}{a}\right) dt \quad (18)$$

where, a is the scaling factor; b is the shifting factor; $s(t)$ is the signal as a function of time; and $\psi(t)$ is the so-called mother wavelet that must satisfy the following criterion:

$$\int_{-\infty}^{\infty} \frac{|\hat{\psi}(\omega)|^2}{|\omega|} d\omega < \infty \quad (19)$$

where, $\hat{\psi}(\omega)$ is the Fourier transformation of $\psi(t)$. This is known as the admissibility condition which implies $\hat{\psi}(0) = 0$. If we define $\psi_{a,b}(t)$ as:

$$\psi_{a,b}(t) = \frac{1}{\sqrt{a}} \psi\left(\frac{t-b}{a}\right) \quad (20)$$

then equation (18) can be rewritten as the inner product of the signal $s(t)$ and $\psi_{a,b}(t)$ as:

$$W_{\psi}(a, b) = \int_{-\infty}^{\infty} s(t) \psi_{a,b}(t) dt \quad (21)$$

In terms of the application in the identification of vehicle axles, the presence or absence of a vehicle axle will cause a sudden change of the slope of the strain signal. While this abrupt change is very difficult to directly observe, a wavelet analysis may be able to amplify these slope discontinuities in the form of sharp peaks in the transformed signal. In the present study, the Morlet wavelet is used to conduct the CWT after comparing the performance with several alternatives such as the reverse biorthogonal wavelets and Daubechies wavelets. The Morlet wavelet can be considered as a modulated Gaussian wave formation. It has a good locality property in both the time and frequency domains. Technically, the Morlet wavelet is complex-valued. However, in many applications, only the real part is used. The complex version is more well-known as the Gabor wavelet. The wavelet function for the Morlet wavelet is given as:

$$\psi(t) = e^{-\frac{t^2}{2}} \cos(5t) \quad (22)$$

Identification of the Vehicle's Transverse Position

In the Moses's algorithm, the error function was defined as the squared difference between the predicated and the measured total responses of the beam-slab bridge [8]:

$$E = \sum_{k=1}^T \left(\sum_{i=1}^n M_{i,k}^p - \sum_{i=1}^n M_{i,k}^m \right)^2 \quad (23)$$

where, n is the number of girder; T is the number of scans; $M_{i,k}^m$ is the measured bending moment for the i th girder at time instant k ; and $M_{i,k}^p$ is the predicted bending moment for the i th girder at time instant k and can be calculated using the influence line concept:

$$M_{i,k}^p = \sum_j^N A_j \times IL_{i,j,k} \quad (24)$$

where, A_j is the axle weight of the j th axle; N is the number of axles of the vehicle; and $IL_{i,j,k}$ is the influence line ordinate for the i th girder corresponding to the position of the j th axle at time instant k . Essentially, the bridge was treated as a 1D beam and the transverse position (TP) of the vehicle was not considered. The error function given by equation (23) is not suitable for the identification of the vehicle's TP in that the total response of the bridge is not very sensitive to the TP of the vehicle. Nevertheless, the response of an individual girder is sensitive to the vehicle's TP.

Generally speaking, for a bridge with n parallel measurement stations in the transverse direction, the error function for the m th measurement station can be expressed as:

$$E_m = \sum_{k=1}^T (M_{m,k}^p - M_{m,k}^m)^2 \quad (25)$$

where, $M_{m,k}^p$ can be more accurately calculated using the influence surface concept than the influence line concept in equation (24) as:

$$M_{m,k}^p = \sum_j^N A_j \times IS_{m,j,k}(TP) \quad (26)$$

where, $IS_{m,j,k}(TP)$ is the influence surface ordinate for the m th measurement station corresponding to the transverse position of the vehicle at TP and the longitudinal position of j th axle at time instant k . Essentially, $M_{m,k}^p$ becomes a function of both the axle weights and the TP when the influence surface concept is adopted.

To identify the TP of the vehicle, a series of values for the TP covering all possible positions where the vehicle may present is first assumed and for each assumed TP, the measured response of the m th station is used to identify a set of axle weights corresponding to this TP

by using the least-squares method to minimize equation (25), i.e., the m th measurement station can be thought of as the weighing station in the proposed algorithm. Due to the response sensitivity of the weighing station to the TP of the vehicle, the obtained sets of axle weights will vary with different assumed TPs. Mathematically, the different sets of axle weights obtained are all solutions to the least-squares problem, i.e., all solutions can reproduce the measured response for the weighing station. However, only the solution corresponding to the true TP of the vehicle has physical meanings. In other words, only the set of axle weights identified at the true TP can reproduce the measured responses for all other measurement stations. Thus, if the assumed TP of the vehicle is not the true one, the set of axle weights identified from the weighing station will be either over- or underestimated and thus cannot simultaneously reproduce the measured responses for all other measurement stations, based on which the following error function can be defined:

$$E = \sum_{i=1}^{n-1} \sum_{k=1}^T (M_{i,k}^p - M_{i,k}^m)^2 \quad (27)$$

where, n is the number of measurement stations; $M_{i,k}^m$ and $M_{i,k}^p$ are the measured and the predicted responses for the i th non-weighing station at time instant k , respectively; and $i=1, \dots, m-1, m+1, \dots, n$ (totally $n-1$), i.e., the error of the m th measurement station (the weighing station) is excluded here. By substituting all solutions into equation (27), the value of the error function for each assumed TP can be calculated and the true TP of the vehicle will be the one that minimizes equation (27). The reason for not considering the error of the m th measurement station, i.e., the weighing station, in equation (27) is that although the measured and the predicted responses should match for the weighing station for all possible TPs, there still exist small errors caused by factors other than the vehicle's TP such as the dynamic effect and the measurement noise. Therefore, the error of the weighing station is excluded from equation (27) in order to reduce the unintended errors.

Identification of the Vehicle's Axle Weight and GVW

The error function for the total number of step T is defined as:

$$E = \sum_{k=1}^T (M_k^p - M_k^m)^2 \quad (28)$$

To minimize the error function, the least-squares method is used. The partial derivative with respect to the axle weight is set to zero:

$$\frac{\partial E}{\partial A_j} = 2 \sum_{k=1}^T (M_k^p - M_k^m) \frac{\partial (M_k^p - M_k^m)}{\partial A_j} = 0 \quad (29)$$

which leads to the following equation upon rearrangement and substitution:

$$\sum_{k=1}^T \sum_{i=1}^N A_i I_{i,(k-C_i)} I_{j,(k-C_j)} = \sum_{k=1}^T M_k^m I_{j,(k-C_j)} \quad (30)$$

Define:

$$F = [F_{ij}] = \sum_{k=1}^T I_{i,(k-C_i)} I_{j,(k-C_j)} \quad (31)$$

$$M = [M_j] = \sum_{k=1}^T M_k^m I_{j,(k-C_j)} \quad (32)$$

equation (30) can then be written in a matrix form as:

$$FA = M \quad (33)$$

Thus, the axle weight and gross vehicle weight (GVW) can be calculated as:

$$A = F^{-1}M \quad (34)$$

$$GVW = \sum_{i=1}^N A_i \quad (35)$$

DISCUSSION OF RESULTS

Condition Assessment of the I-10 Twin Span Bridge

Bridge and Instrumentation Description

The bridge selected for the case study is the new I-10 Twin Span Bridge (TSB) located in southern Louisiana. Being a vital part of the Interstate 10, the new TSB crosses the Lake Pontchartrain connecting Slidell and New Orleans. The new TSB was built after the original span suffered extensive damages from Hurricane Katrina in 2005. The strong storm surge brought by the hurricane lifted many precast segments off their piers as shown in Figure 3. Although one span was repaired shortly after the catastrophic hurricane, the original bridge was deemed too vulnerable to storm surges and it was decided that a new bridge with higher capacity to withstand extreme events such as hurricanes needs to be built to replace the existing bridge. The construction of the new TSB started in 2006 and was completed in 2011. It was the largest public work project in Louisiana history.

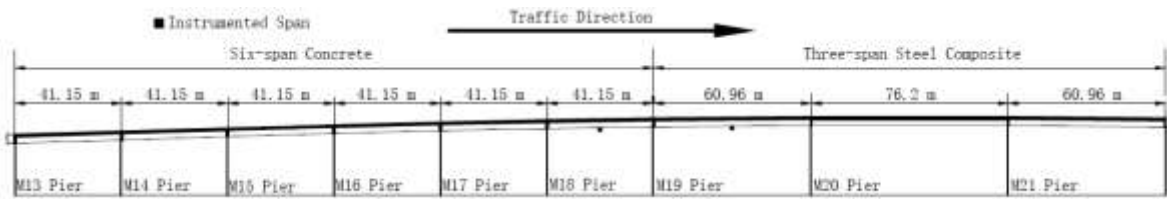


Figure 3

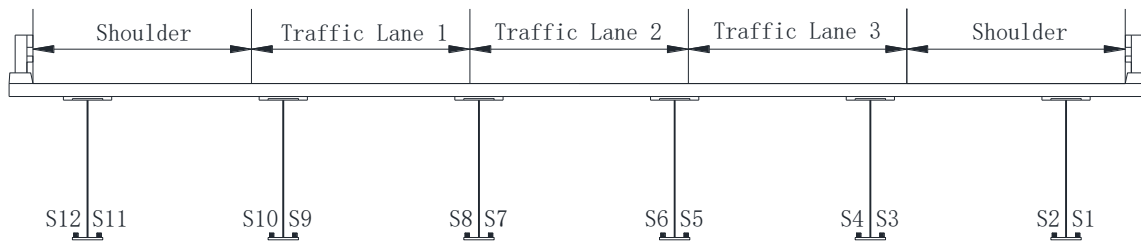
Damaged original twin span and the new Twin Span: (a) original twin span bridge damaged by Hurricane Katrina; (b) the new I-10 Twin Span bridge

The new TSB, constructed entirely using high performance concrete, is approximately 8690.5-m long and consists of two parallel spans, the Westbound and the Eastbound, each with three 3.66 m. traffic lanes and two 3.66-m shoulders on two sides, allowing for a fifty percent increase of traffic volume. The bridge has an elevation of 9.14 m (6.40 m higher than the original span) and a high-ribe span of 24.38 m for navigations. The superstructures of the bridge include units of continuous concrete spans and a three-span continuous steel-composite bridge for the high-ribe span. Each span consists of six identical girders with equal spacing of 3.28 m. A structural monitoring system (SHM) was installed on the M19 pier of the Eastbound, the pier south of the marine traffic underpass, and the two spans supported by

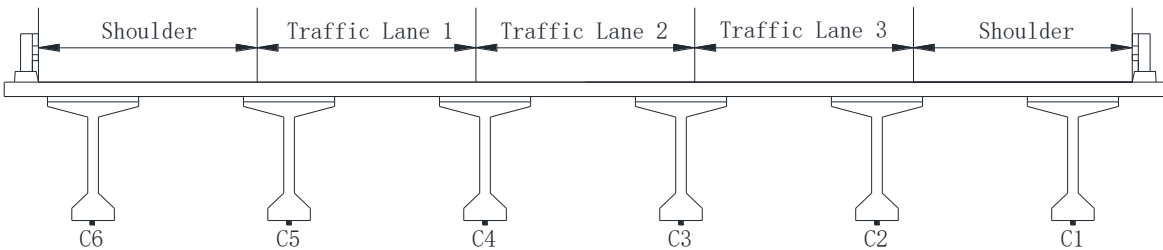
the pier. In this study, the data collected from the superstructure instrumentation were used. Figure 4 (a) shows the longitudinal profile of the instrumented spans. Strain sensors were installed on each girder of both spans at the mid-span. Figure 4 (b) and (c) show the sensor layouts on the cross-sections of the instrumented spans.



(a)



(b)



(c)



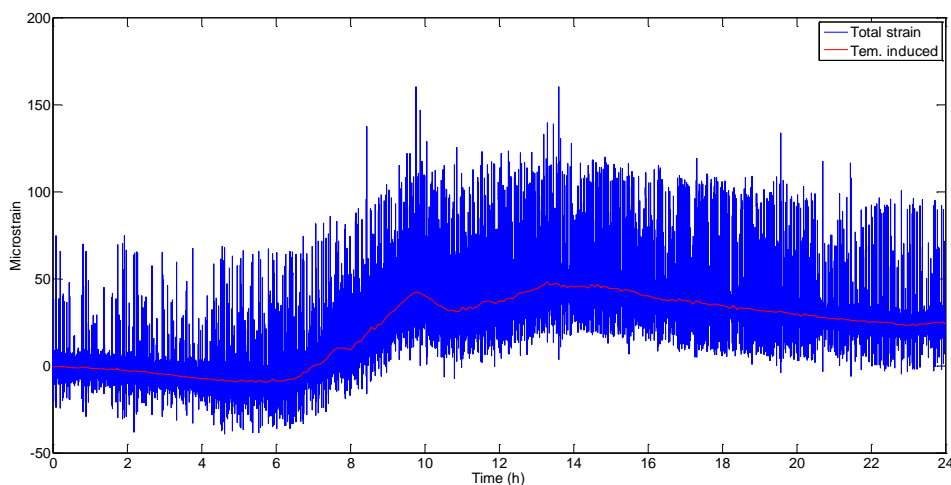
(d)

Figure 4
Instrumentation of the I-10 Twin Span Bridge; (a) longitudinal profile of instrumented spans; (b) sensor layout of the steel span (with traffic flow at mid-span); (c) sensor layout of the concrete span (with traffic flow at mid-span); (d) M19 pier

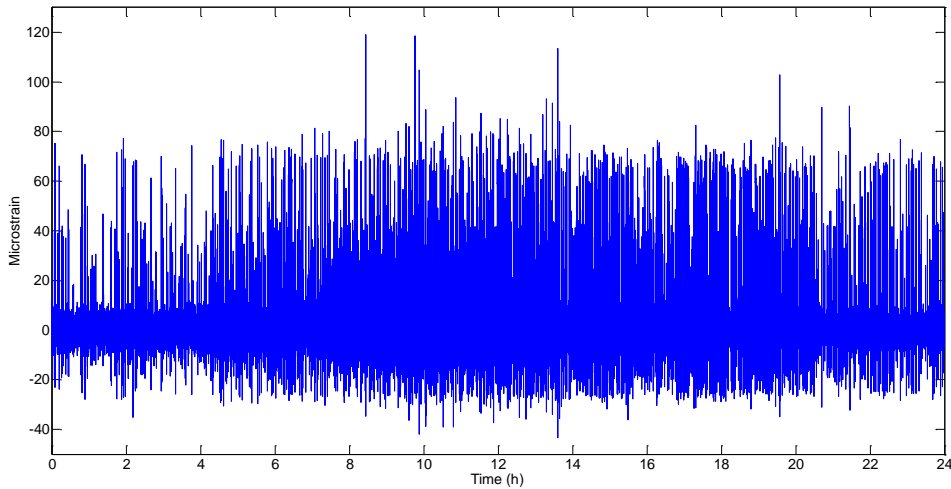
Analysis of Monitoring Data

Figure 5 (a) shows the sample time history of the measured strain response of S4 for one day from 0:00 to 24:00. The measured strain response of the bridge consists of temperature-induced and traffic-induced components. The variation of the temperature results in material deformations and causes the strain to vary slowly with time. The effect of traffic is more transient and thus causes peaks in the strain response as shown in Figure 5 (a). While the temperature-induced strain could be significant, its contribution to the stress is insignificant because the expansion joints of the bridge allow free movement in the longitudinal direction. For the selected bridge, the traffic loading causes the bending of the bridge and the traffic-induced strain is the main contribution of the stress. Thus, in order to obtain the stress response of the bridge, the traffic-induced strain responses need to be extracted from the measured strain response. This can be done by using the multi-resolution wavelet decomposition. Through wavelet decomposition, the signal is decomposed at multiple levels of resolution. At each level, the signal is divided into approximation coefficients and detail coefficients. The approximation coefficients contain the low-frequency components of the signal which correspond to temperature-induced strains. Thus, the traffic-induced strain can be obtained by subtracting the measured response with the temperature-induced strains.

In this study, the Symlets wavelet is used and the temperature-induced strain is successfully separated from the measured response at 14-level decomposition as can be seen from Figure 5 (a). Figure 5 (b) shows the traffic-induced strain response extracted as the difference between the measured and temperature-induced strains. It can be seen that the distribution of peaks is more concentrated from 8:00 to 18:00 because the traffic is denser at daytimes.



(a)



(b)

Figure 5

Sample time history of strain response at S4: (a) measured and temperature-induced strains; (b) traffic-induced strain

Prediction of Extreme Traffic LEs

The daily maximum strain responses are obtained from 65 days of monitoring data and the Bayesian method is used to predict the future maximum traffic load effects (LEs). For demonstration purposes, the prediction of the maximum positive strains of S4 is used as an example to illustrate the estimation procedures. Figure 6 shows the normalized histogram for the daily maxima of positive strains of S4 and the corresponding GEV fit. The MLE estimates of the shape, scale, and location parameters are obtained as -0.077, 15.91, and 102.93, respectively.

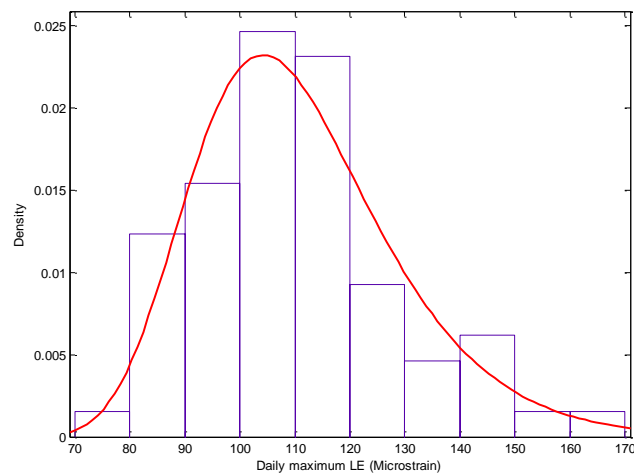


Figure 6

Normalized histogram of daily maxima of S4 and the corresponding GEV fit

Under the Bayesian framework, each distribution parameter is treated as a random variable and the posterior distribution of parameters can be obtained using the MCMC sampler. The MG sampler was first tuned to obtain the optimal acceptance rate and then 100,000 iterations were performed to ensure the prediction accuracy. Figure 7 shows the trace plots of parameters. It can be seen that the chain converged very quickly and that the chain mixed well. The burn-in period is chosen as 1,000, i.e., the first 1,000 iterations were discarded to ensure that the samples are generated from the true posterior distribution. Figure 8 shows the marginal posterior distributions using the kernel density estimation (KDE). From Figure 8, significant uncertainty of the parameters is observed, which is expected because of a relatively small sample size. Compared with the conventional method, the Bayesian method is able to quantify the uncertainty of parameters in terms of posterior distributions. In fact, it can be seen from Figure 8 that the modes of the marginal posterior distributions of shape, scale, and location parameters are roughly estimated as -0.08, 16, and 103, respectively, which are very close to the MLE estimates. This is because the uniform prior is adopted and the posterior distribution is essentially the normalized likelihood function. Furthermore, the uncertainty of return levels can be subsequently quantified using the obtained posterior distribution of parameters. For each set of GEV parameters obtained using the MG sampler, the corresponding T -year return level is calculated using equation (4) and thus the distribution of the T -year return levels can be obtained. Figure 9 shows the distribution of the 5-year and 75-year return levels of S4 using KDE. It can be seen that the distribution of the 75-year return level has longer tails than that of the 5-year return level, indicating that the extreme loadings are more likely to occur for longer return periods. The distribution of return levels can be used for reliability analysis.

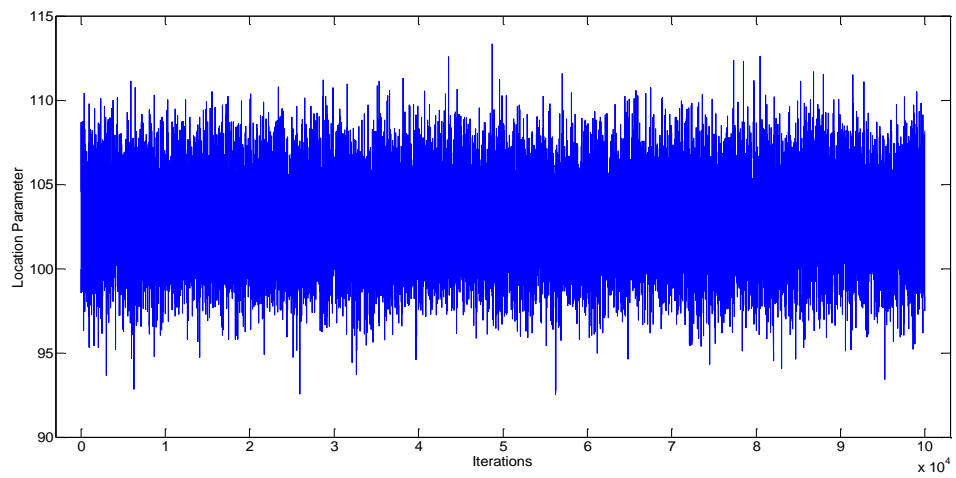
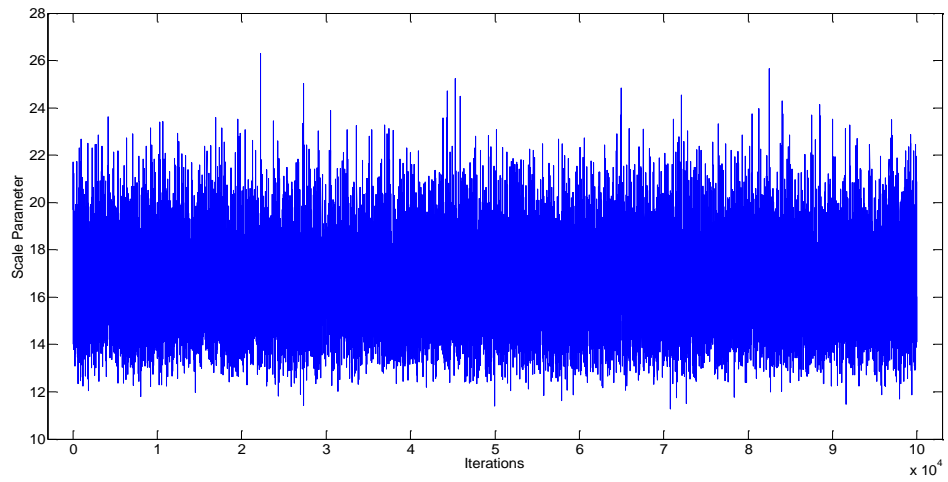
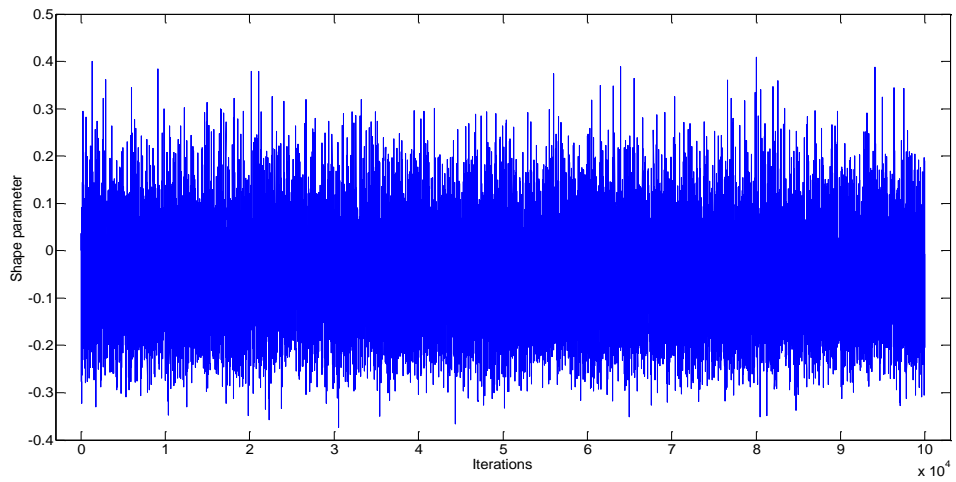


Figure 7
Trace plots of GEV parameters

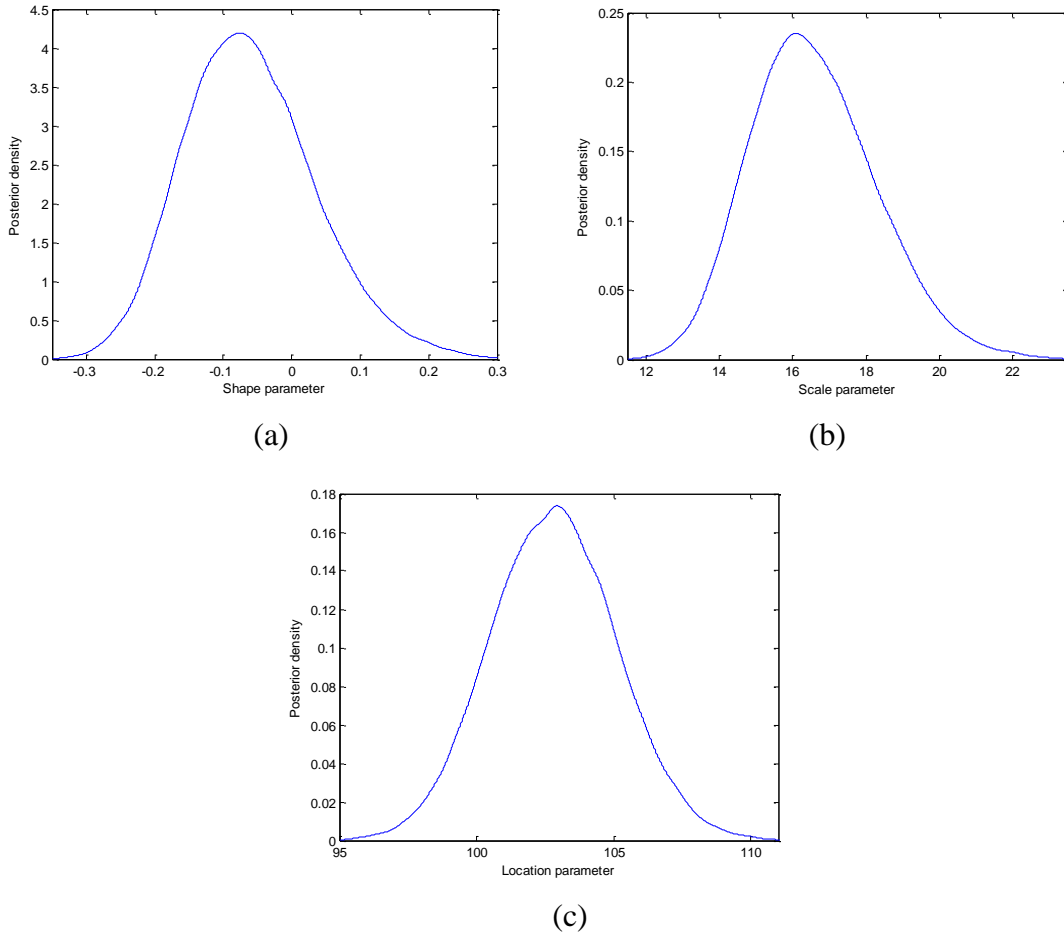


Figure 8
Marginal posterior distributions of the GEV distribution parameters: (a) shape parameter; (b) scale parameter; (c) location parameter

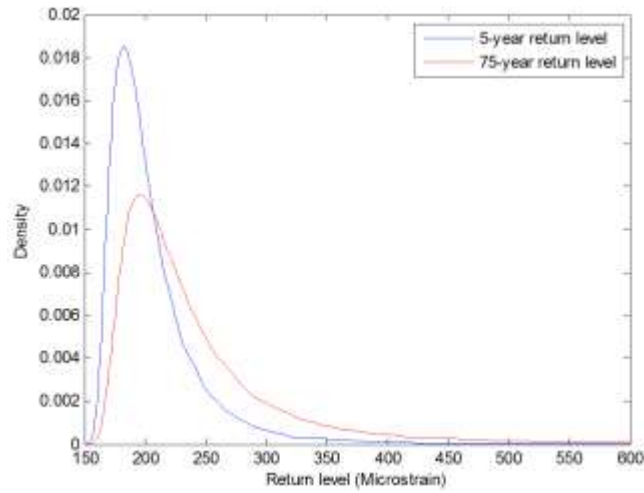


Figure 9
Distribution of 5-year and 75-year return levels of S4

Finally, the future maximum LEs are predicted using the posterior predictive distribution. Following the previously described procedures, the posterior predictive distribution is obtained. Figure 10 shows the predictive distribution using the KDE as well as the fitted GEV distribution. It can be seen that the predictive distribution has a wider spread than the fitted GEV distribution. This is because the uncertainty inherent in the parameters was included in the predictive distribution. The Bayesian estimate of future maximum LEs are obtained by evaluating the quantiles of the predictive distribution. Figure 11 plots the variation of the predicted maximum strains of S4 with respect to the return period obtained using both the Bayesian and conventional methods. From Figure 11, it can be seen that the predicted response using the Bayesian method is significantly higher than that of the conventional method and that the difference between the two increases as the return period increases. This is because there exists significant uncertainty of parameter as observed from Figure 8. In this case, ignoring the uncertainty may lead to significant underestimation of the prediction and thus the Bayesian method is able to provide more reliable predictions than the conventional method.

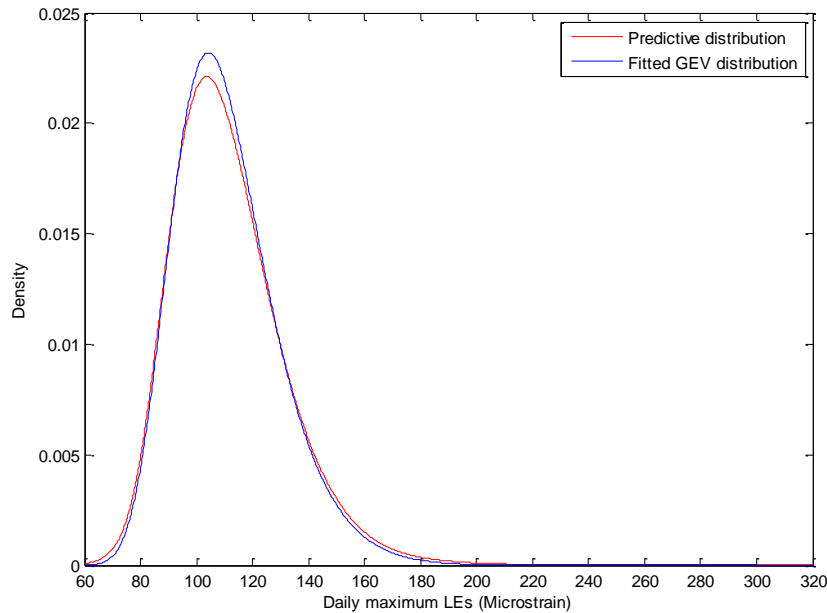


Figure 10
Predictive distribution and fitted GEV distribution of S4

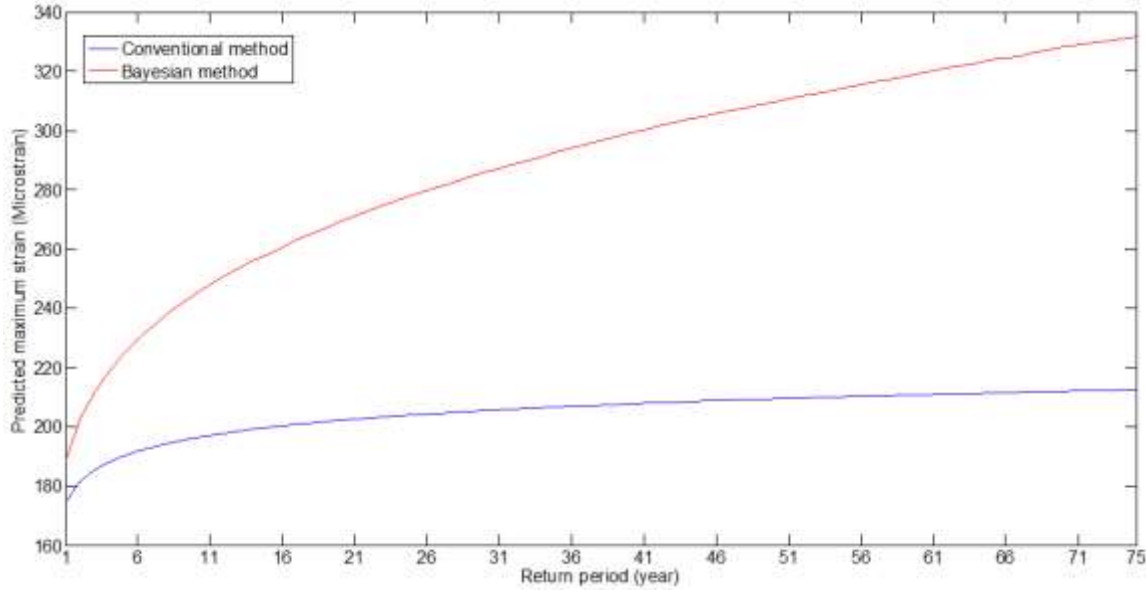


Figure 11
Prediction of maximum LEs of S4

The same procedures are conducted for each sensor of the steel and concrete span. The predicted maximum strains are transferred to the stresses by multiplying the modulus of elasticity of materials assuming that the bridge is operating in elastic stage. Table 1 and Table 2 summarize the predicted maximum stresses for the steel and concrete span at 5 years (the rating period) and 75 years (the design life of structures). These values will later be used for the condition assessment of the bridge.

Table 1
Prediction results for the steel span using Bayesian method

Sensor Number	5-year maximum stresses (MPa)		75-year maximum stress (MPa)	
	Positive	Negative	Positive	Negative
S1	48.86	-13.13	106.49	-20.95
S2	64.36	-21.85	108.99	-31.57
S3	46.88	-19.43	74.05	-32.83
S4	46.01	-17.97	68.01	-26.93
S5	27.44	-11.37	30.16	-13.58
S6	25.72	-10.90	27.85	-13.09
S7	21.24	-9.17	24.11	-11.94
S8	25.84	-10.99	29.86	-13.65
S9	18.02	-8.64	24.68	-12.56
S10	23.74	-10.38	30.75	-13.59
S11	37.32	-11.95	60.69	-16.01
S12	37.05	-13.75	56.11	-18.65

Table 2
Prediction results for the concrete span using Bayesian method

Sensor Number	5-year maximum stresses (MPa)		75-year maximum stress (MPa)	
	Positive	Negative	Positive	Negative
C1	3.96	-0.71	7.12	-0.79
C2	3.49	-0.67	4.96	-0.75
C3	2.67	-0.67	3.50	-0.85
C4	2.33	-0.64	2.99	-0.79
C5	2.28	-0.67	3.39	-0.86
C6	3.02	-0.75	5.04	-0.96

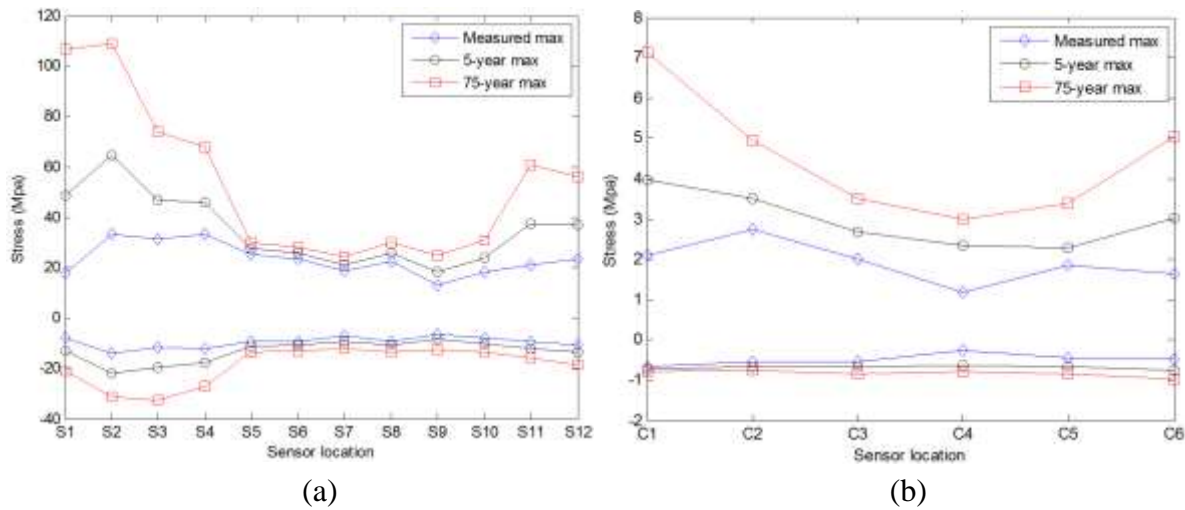


Figure 12

Variation of measured and predicted maximum stresses with respect to sensor locations: (a) steel span; (b) concrete span

Figure 12 plots the variation of measured and predicted maximum stresses with respect to the sensor location. It can be seen that the measured stresses generally decrease as the sensor number increases. This is because most heavy trucks travel on the slow lane (Lane 3 shown in Figure 4) and the girders close to the slow lane experience higher LEs. Moreover, it was observed that the maximum positive and negative stresses of the steel span have a similar trend of variation while this is not the case for the concrete span. The reason for this is that the maximum positive and negative stresses of the steel span are mostly caused by the same truck events and thus they have similar shapes of distribution. However, the maximum positive and negative stresses of the concrete span are usually caused by different truck events. Figure 13 shows the typical stress responses of the concrete span. It can be seen that although the concrete span was designed to be continuous, the negative stress induced by the truck before it enters the instrumented span is almost negligible. Instead, the free vibration of the bridge after the truck left the span can induce significant negative stresses. This is

probably because the natural frequency of the concrete span, which is identified to be about 3 Hz as will be shown later, is close to the typical frequencies of highway vehicles. The matching of frequencies could lead to quasi-resonance and cause significant vibrations of the bridge [9]. In addition, the occurrence of the free vibration also requires the absence of heavy trucks on the span. Therefore, the causes of positive and negative stresses are different for the concrete span, leading to different trends of variation.

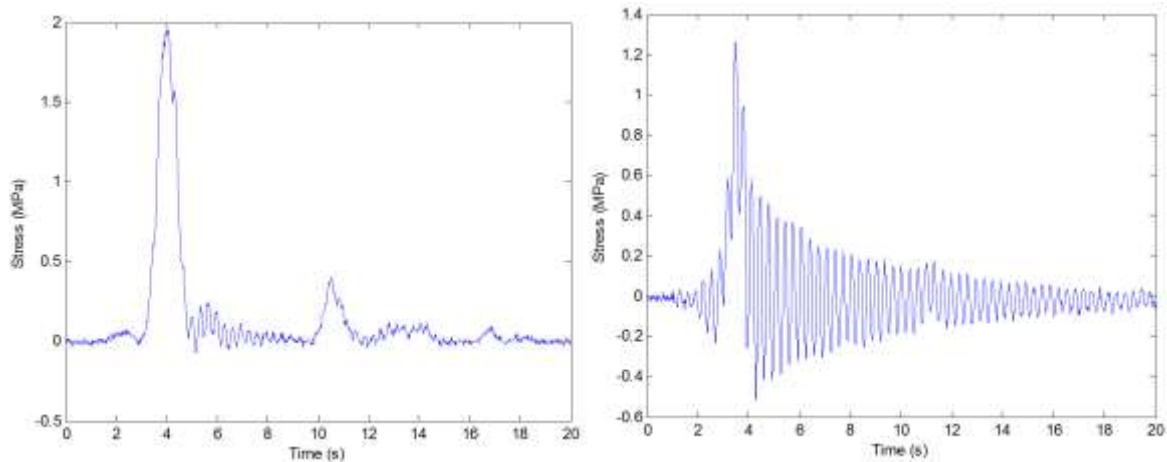


Figure 13
Typical stress responses of the concrete span at sensor C2

Furthermore, it can be seen from Figure 12 that the predicted maximum stresses of exterior girders tend to increase faster with the increase of the return period than those of interior girders because the maximum stress distributions of exterior girders have heavy upper tails. For example, Figure 14 shows the distribution of the maximum positive stresses for S2 on the exterior girder and S5 on the interior girder. It can be seen that the distribution for S2 is obviously right skewed with a long upper tail while the distribution of maximum LEs for S5 is left skewed with a much shorter upper tail. For the GEV distribution, the tail behavior is the governed by the shape parameter. A larger shape parameter results in a longer upper tail and thus higher return levels. The marginal posterior distributions of shape parameters for S2 and S5 are shown in Figure 15. It can be seen that the shape parameters of S2 are mostly positive while the shape parameter of S5 are negative. Consequently, the increasing rate of predicted maximum stresses of exterior girders will be higher than that of interior girders.

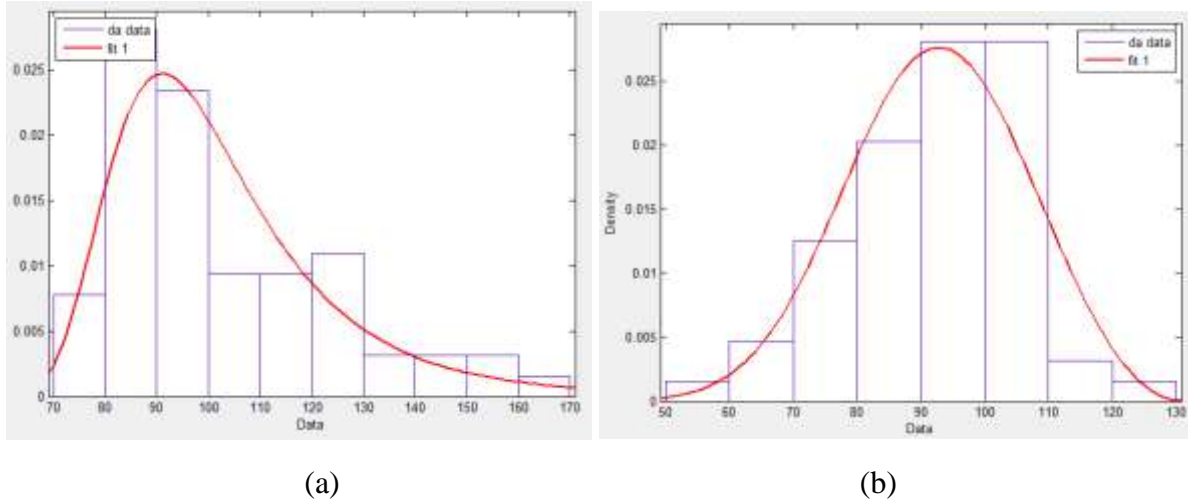


Figure 14
Distribution of daily maximum LEs: (a) S2; (b) S5

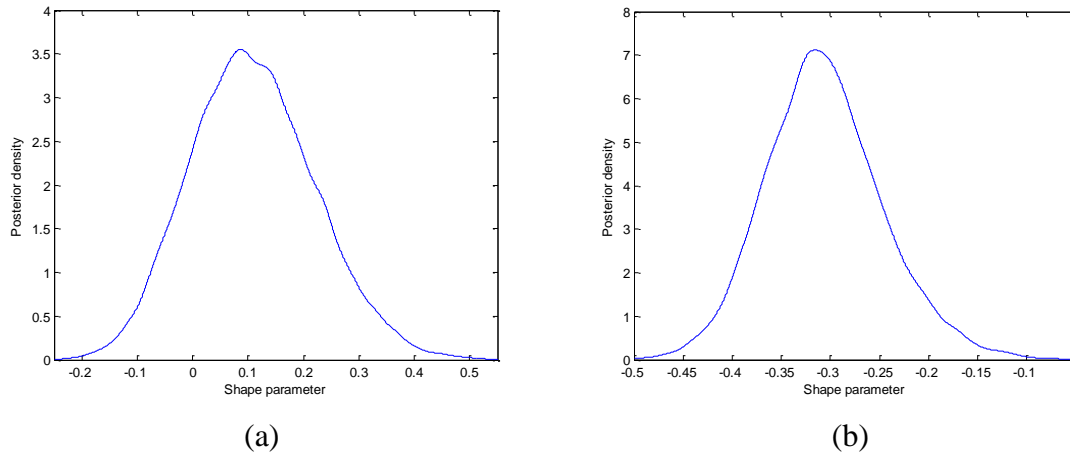


Figure 15
Marginal posterior distributions of shape parameters: (a) S2; (b) S5

In fact, the upper tail of the maximum stress distributions of exterior girders is caused by cases where trucks were traveling on or close to the shoulder. These cases produce significantly higher stresses in exterior girders but their occurrences are less frequent than trucks traveling on Lane 3, which causes the distribution to be right skewed with heavy upper tails. This also indicates that the daily maximum stress of some sensors is not identically distributed. In other words, the distribution of daily maximum stresses is a mixed distribution. Caprani et al. adopted the composite distribution statistics (CDS) approach to account for the mixture of loading events [10]. In the CDS approach, the maximum LEs are classified based on their event types and the maximum LEs of each event type are fitted to the GEV distribution. The composite distribution is then formulated based on the GEV distributions of each event type. However, it is very difficult to always identify the event types in practice and the data collected for some extreme event types may not be sufficient

[11]. Therefore, it may not be practical to use the CDS approach in reality. The Bayesian method can be seen as a compromise between the CDS approach and the conventional approach in that although it does not classify data based on event types, it recognizes and considers the uncertainty in distribution parameters and thus provides more reasonable predictions than the conventional method.

It should be mentioned that the prediction of future maximum stresses was made based on only 65 daily maximum stresses and thus the accuracy of the prediction for longer return periods such as 75 years need to be taken into consideration when using the prediction results. When more data becomes available in the future, it should be included to update the prediction. In this case, the uncertainty of parameters will be reduced and the posterior distribution will become more concentrated. Consequently, the prediction using the Bayesian method will approach that using the conventional method. Nevertheless, as more data is obtained, the block length should also be increased to obtain more reliable predictions as discussed before. Thus, there will always exist certain levels of uncertainties that need to be accounted for using the Bayesian method.

Bridge Condition Assessment

Using on the measured and prediction results, the condition of the bridge will be assessed based on the previously proposed framework. First, the design capacity envelops needs to be developed. The bridge was designed according to the AASHTO LRFD specification [1]. The design live load is specified as the HL-93 including a design truck or design tandem and design lane load. The design live load is distributed to girders using the distribution factors. For the bridge under assessment, the design calculation shows that the exterior girder controls and the factored live load moments are given in Table 3. The section properties were also calculated and listed in Table 3. Assuming that the bridge is perfectly designed, the design live load capacity can be evaluated as:

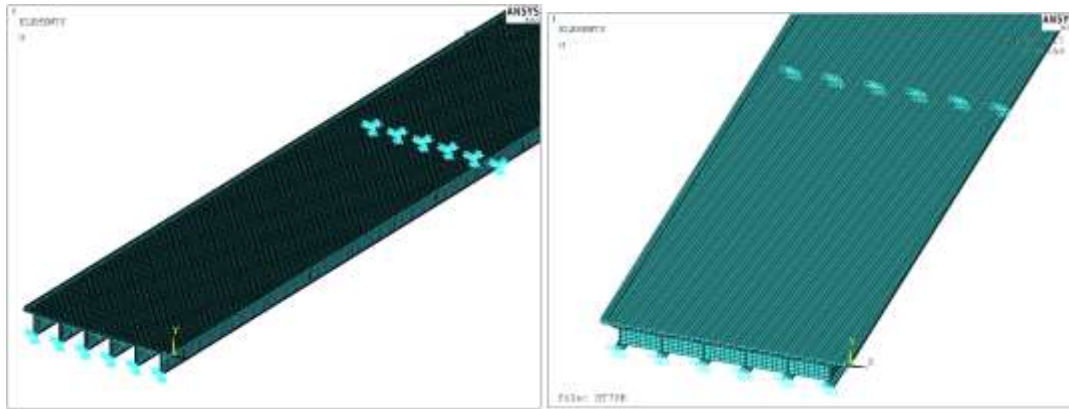
$$\sigma = \frac{M}{S} \quad (36)$$

where, M is the design live load moment and S is the section modulus. Using equation (36), the design live load capacities of the steel and concrete span are calculated and given in Table 3.

Table 3
Calculation of design live load capacity of the steel and concrete span

Span	Factored LL moment (kN-m)	Section properties			Design LL capacity (MPa)	
		Moment of inertia (m ⁴)	Distance to N.A. (m)	Section modulus (m ³)		
Steel span	Positive moment	12919.25	0.13189	1.8407	0.071652	180.31
	Negative moment	-3278.01				-45.75
Concrete span	Positive moment	6941.17	0.81568	1.4942	0.545898	12.72
	Negative moment	-1607.69				-2.95

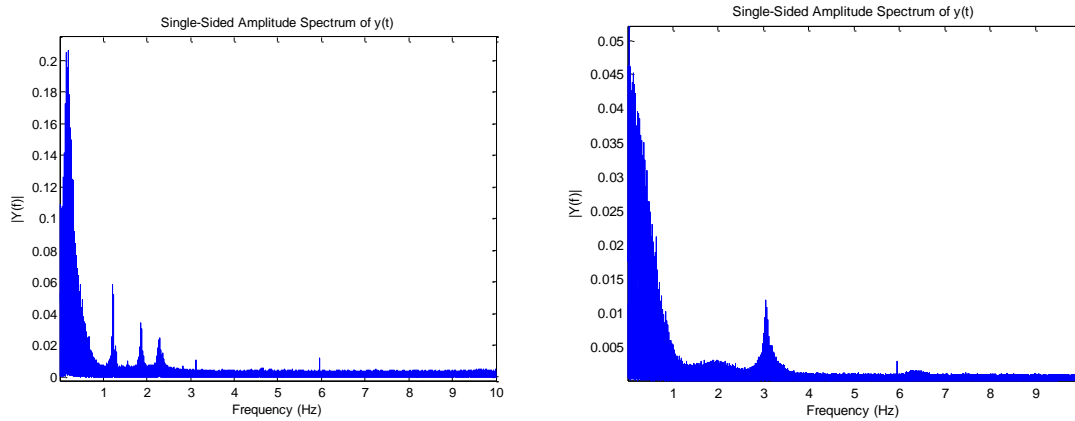
In order to obtain the service LE envelops, the FE models were constructed according to the bridge design plans using the ANSYS FE package. For the steel span, the concrete deck was modeled using solid elements and the steel girders were modeled using shell elements. The K-shaped cross frames at the supports and intermediate locations were modeled using 3D beam elements with defined cross-sections. The concrete span is modeled entirely using solid elements. Figure 16 shows the FE models of the bridge. The FE models were preliminarily calibrated using the natural frequencies identified from the strain responses. Figure 17 shows the amplitude spectra of the traffic-induced strain responses of one day. It can be seen that three frequencies can be identified for the steel span while only one frequency can be identified for the concrete span. To calibrate the FE models, the elastic moduli of materials are adjusted to match the identified natural frequencies. Table 4 gives the as-design and calibrated values of the elastic moduli. The calibrated parameters can serve as better indicators of the bridge behavior than the as-design parameters. Nevertheless, it should be mentioned that a more refined calibration of FE models should be conducted if a load test using known trucks was conducted. Using the calibrated FE models, the design lanes are positioned to obtain the maximum LEs. Multiple presence factors are applied to account for the probability of simultaneous occurrence. For the exterior girders, three design lanes and two design lanes were found to cause the maximum LEs for the steel span and concrete spans, respectively. For the interior girders, three design lanes were found to cause the maximum LEs for both spans. The obtained design capacity envelops and service LE envelops for the steel and concrete spans are summarized in Table 5 and Table 6, respectively. The measured maximum stresses are also given. It can be seen that the service LE envelops are significantly smaller than the design capacity envelops. This is because the FE models more accurately reflect the bridge behavior as discussed before.



(a)

(b)

Figure 16
FE models of the bridge: (a) the steel span; (b) the concrete span



(a)

(b)

Figure 17
Amplitude spectra of strain responses: (a) the steel span; (b) the concrete span

Table 4
FE model calibration parameters

Parameters		As-design value (MPa)	Calibrated value (MPa)
Steel Span	Elastic modulus of concrete deck	34169	38500
	Elastic modulus of steel girders	204774	201000
Concrete Span	Elastic modulus of concrete deck	34169	41300
	Elastic modulus of concrete girders	41145	47400

Table 5
Maximum measured stress and LE envelops for the steel span

Sensor Number	Measured maximum stress (MPa)		Service performance envelop (MPa)		Design LL capacity envelop (MPa)	
	Positive	Negative	Positive	Negative	Positive	Negative
S1	17.63	-8.06	70.58	-18.78	180.31	-45.75
S2	33.07	-13.87	72.63	-19.09	180.31	-45.75
S3	31.34	-11.75	62.52	-18.25	180.31	-45.75
S4	33.05	-12.29	64.68	-18.59	180.31	-45.75
S5	25.31	-9.47	54.59	-17.98	180.31	-45.75
S6	23.57	-9.20	56.61	-18.29	180.31	-45.75
S7	18.57	-7.24	56.61	-18.29	180.31	-45.75
S8	22.57	-9.56	54.59	-17.98	180.31	-45.75
S9	13.22	-6.42	64.68	-18.59	180.31	-45.75
S10	18.27	-8.03	62.52	-18.25	180.31	-45.75
S11	20.99	-9.49	72.63	-19.09	180.31	-45.75
S12	23.17	-10.79	70.58	-18.78	180.31	-45.75

Table 6
Maximum measured stress and LE envelops for the concrete span

Sensor Number	Measured maximum stress (MPa)		Service performance envelop (MPa)		Design LL capacity envelop (MPa)	
	Positive	Negative	Positive	Negative	Positive	Negative
C1	2.09	-0.649	6.88	-1.46	12.72	-2.95
C2	2.73	-0.551	5.90	-1.22	12.72	-2.95
C3	2.00	-0.549	4.93	-0.94	12.72	-2.95
C4	1.17	-0.263	4.93	-0.94	12.72	-2.95
C5	1.86	-0.446	5.90	-1.22	12.72	-2.95
C6	1.65	-0.476	6.88	-1.46	12.72	-2.95

In order to assess the current condition of the bridge, Figure 18 plots the measured maximum stresses and response envelops for the steel and concrete spans. It can be seen that the measured maximum stresses of both spans are below the service LE and design capacity envelops, indicating that the bridge is safe and performing as designed under the current condition. Also, it can be seen that the safety reserve of the bridge is quite large under the current condition.

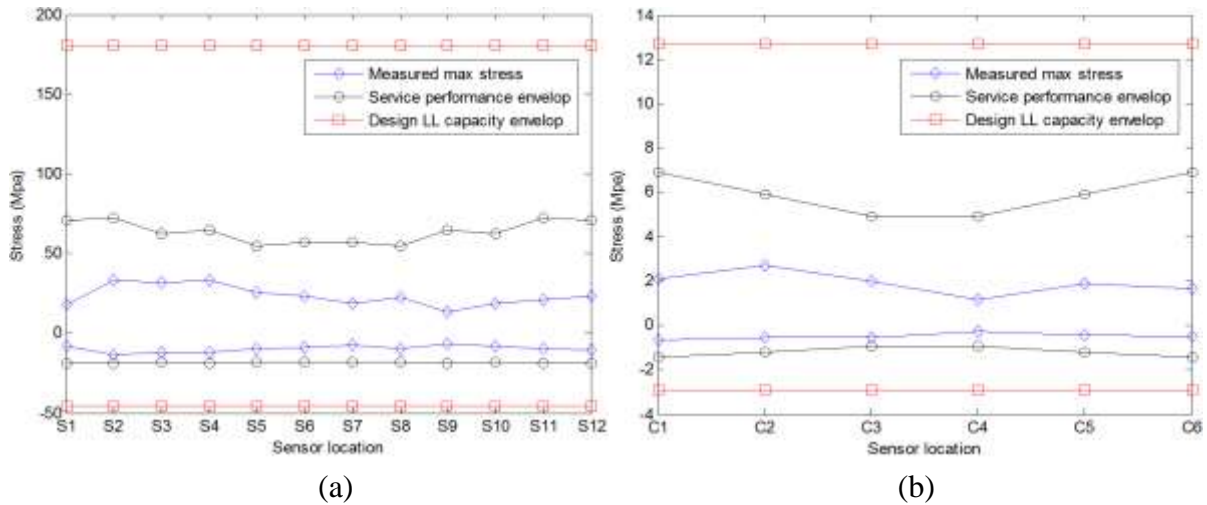


Figure 18
Assessment of current condition: (a) steel span; (b) concrete span

Furthermore, in order to assess the future condition of the bridge, the predicted maximum stresses and response envelops are plotted in Figure 19 and Figure 20 for the steel and concrete spans, respectively. It can be seen from Figure 19 (a) and Figure 20 (a) that the 5-year maximum stresses of both spans are generally below the response envelops, indicating that the bridge will be safe and performing as designed in the next five years. For the 75-year condition, it was observed from Figure 19 (b) and Figure 20 (b) that the maximum stresses of sensors were below the design capacity envelop. However, it was found that the maximum stresses of certain sensors exceeded the service LE envelops, suggesting that the bridge may be overstressed in the future. These sensors were installed on the exterior girders under the right shoulder for both spans and the interior girder under the Lane 3 for the steel span. In practice, these girders also experience the largest traffic LEs due to their close vicinity to the heavy truck traffic. In addition, it can be seen that the bridge still has sufficient safety reserves even at 75 years from now. The information provided by the assessment can be used for the load rating of the bridge.

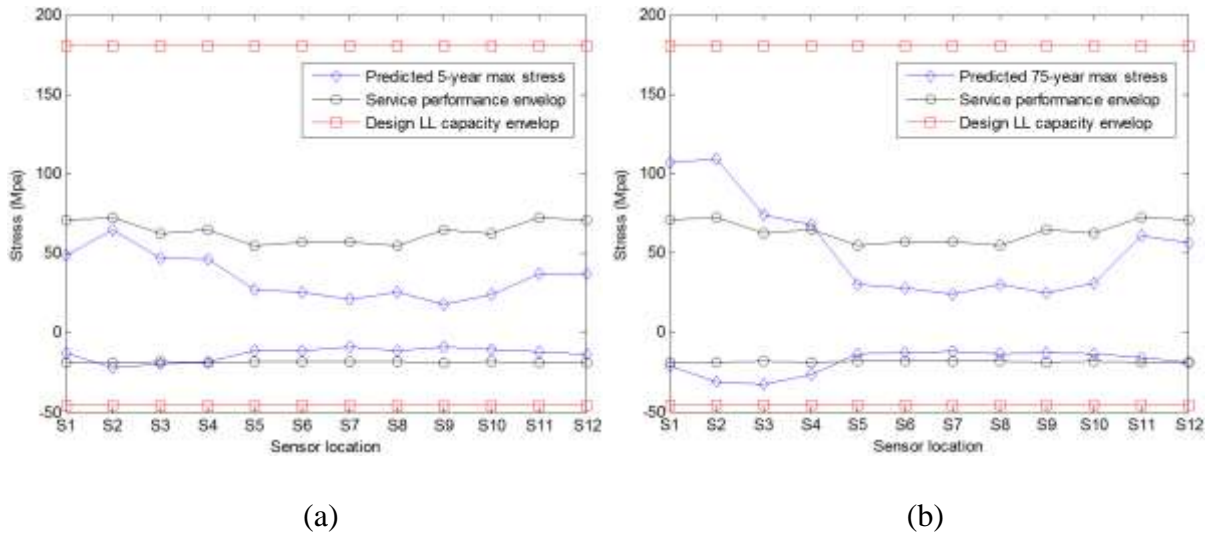


Figure 19
Assessment of future condition for the steel span: (a) 5-year; (b) 75-year

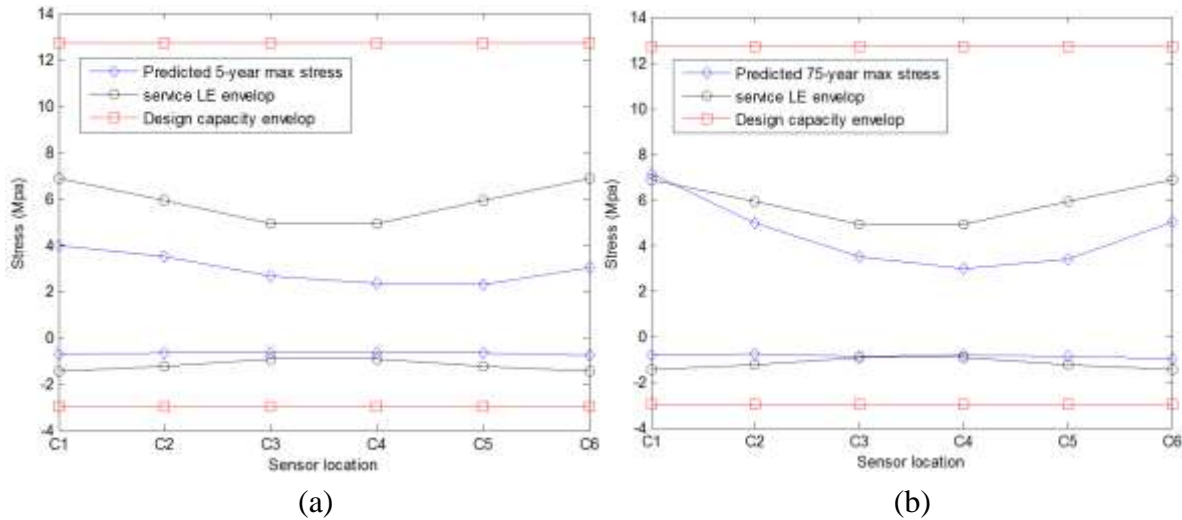


Figure 20
Assessment of future condition for the concrete span: (a) 5-year; (b) 75-year

Live Load Monitoring through Nothing-on-road BWIM

Numerical Simulation

Vehicle Model. In the present study, three typical highway trucks with different numbers of axles are adopted. Table 7 lists the axle configurations of these trucks. The width of all trucks is set as 2.5 m. In the simulation, the truck is modeled as spring-dashpot systems. The vehicle body (tractor or trailer) is represented by a rigid body with a mass and three degrees of freedom (DOFs), i.e., the vertical displacement, the pitching rotation, and the rolling rotation. The connection between the tractor and the trailer is modeled as a pinned connection, i.e., the tractor and the trailer have equal vertical displacement at the connection. Each wheel is represented by a lumped mass with one DOF, i.e., the vertical displacement.

For example, the analytical model of Truck 2 is shown in Figure 21 where Z_V and Z_a represent the vertical displacement of the vehicle body and the tire, respectively; θ_V represents the pitching rotation of the vehicle body; ϕ_V represents the rolling rotation of the vehicle body; K_u and K_l represent the stiffness of the suspension system and the tire, respectively; C_u and C_l represent the damping of the suspension system and the tire, respectively.

Table 7
Axle configurations of truck models

Truck Number	Number of axles	Axle spacing			
		First to second (m)	Second to third (m)	Third to fourth (m)	Fourth to fifth (m)
1	2	6.25	N.A.	N.A.	N.A.
2	3	4.27	4.27	N.A.	N.A.
3	3	4.94	1.40	N.A.	N.A.
4	5	8.00	5.00	2.00	5.00

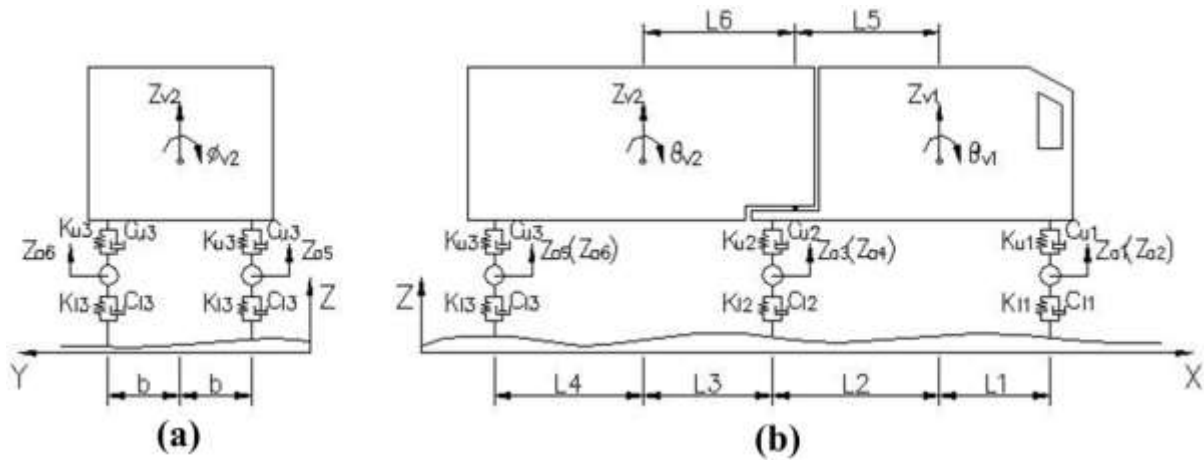


Figure 21
Analytical model of the adopted truck

Bridge Model. In the numerical study, a simply supported beam-slab bridge is adopted. As a good representative of highway bridges, the selected bridge was designed according to the AASHTO LRFD specification and is 24.38-m long and 10.67-m wide [1]. The bridge consists of five identical I-girders and three diaphragms located at the two ends and the mid-span of the bridge. Figure 22 shows the cross section of the bridge. The bridge is modeled with the ANSYS software using solid elements (with three translational DOFs at each node) to predict the dynamic characteristics including the natural frequencies and mode shapes. The finite element (FE) model of the bridge is shown in Figure 23. Modal analysis

shows that the bridge has a fundamental frequency of 3.46 Hz corresponding to the first bending mode.

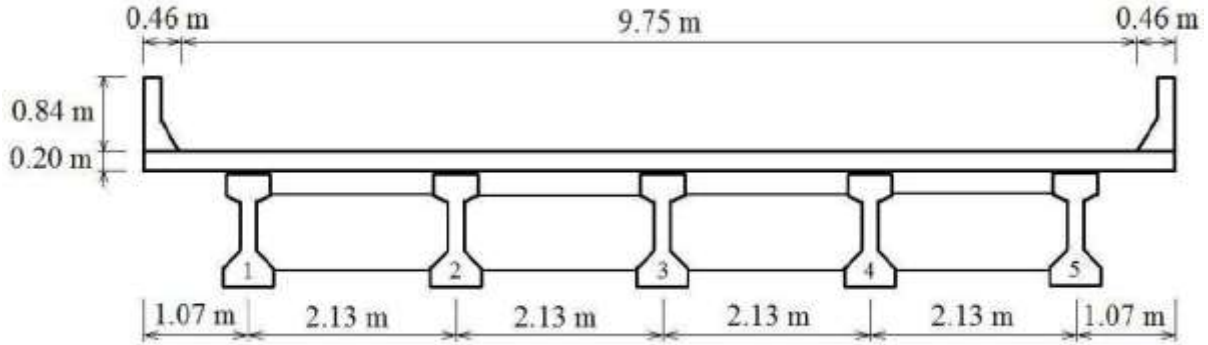


Figure 22
Cross section of the bridge used in the simulation



Figure 23
Finite element model of the bridge used in the simulation

Vehicle-bridge Interaction. In the present study, a coupled approach is used to solve the vehicle-bridge interaction problem [12]. The equations of motion for the vehicle and bridge can be written in matrix forms as:

$$[M_v]\{\ddot{d}_v\} + [C_v]\{\dot{d}_v\} + [K_v]\{d_v\} = \{F_G\} + \{F_v\} \quad (37)$$

$$[M_b]\{\ddot{d}_b\} + [C_b]\{\dot{d}_b\} + [K_b]\{d_b\} = \{F_b\} \quad (38)$$

where $[M_v]$, $[C_v]$, and $[K_v]$ are the mass, damping, and stiffness matrices of the vehicle, respectively; $[M_b]$, $[C_b]$, and $[K_b]$ are the mass, damping, and stiffness matrices of the bridge, respectively; $\{d_v\}$ and $\{d_b\}$ are the displacement vector of the vehicle and bridge,

respectively; $\{F_G\}$ are the gravity force vector of the vehicle; and $\{F_v\}$ and $\{F_b\}$ are the wheel-road contact force vectors acting on the vehicle and bridge, respectively.

Based on the displacement relationship and interaction force relationship at the contact points, the two equations of motion above can be combined into a coupled equation:

$$\begin{bmatrix} M_b & \\ & M_v \end{bmatrix} \begin{Bmatrix} \ddot{d}_b \\ \ddot{d}_v \end{Bmatrix} + \begin{bmatrix} C_b + C_{b-b} & C_{b-v} \\ C_{v-b} & C_v \end{bmatrix} \begin{Bmatrix} \dot{d}_b \\ \dot{d}_v \end{Bmatrix} + \begin{bmatrix} K_b + K_{b-b} & K_{b-v} \\ K_{v-b} & K_v \end{bmatrix} \begin{Bmatrix} d_b \\ d_v \end{Bmatrix} = \begin{Bmatrix} F_{b-r} \\ F_{b-r} + F_G \end{Bmatrix} \quad (39)$$

where C_{b-b} , C_{b-v} , C_{v-b} , K_{b-b} , K_{b-v} , K_{v-b} , F_{b-r} , and F_{b-r} are the interaction-related terms caused by the contact forces. As the vehicle travels through the bridge, the positions of contact points change and so do the contact forces. Therefore, the interaction-related terms are time-dependent terms which will change as the vehicle moves across the bridge.

In order to reduce the size of the matrices and save calculation efforts, the modal superposition technique is adopted and thus the bridge displacement vector $\{d_b\}$ in equation (38) can be expressed as:

$$\{d_b\} = [\{\Phi_1\} \ \{\Phi_2\} \ \dots \ \{\Phi_m\}] \{\xi_1 \ \xi_2 \ \dots \ \xi_m\}^T = [\Phi_b] \{\xi_b\} \quad (40)$$

where m is the total number of modes considered for the bridge; $\{\Phi_i\}$ and ξ_i are the i th mode shape of the bridge and the i th generalized modal coordinate, respectively. If each mode shape is normalized such that $\{\Phi_i\}^T [M_b] \{\Phi_i\} = 1$ and $\{\Phi_i\}^T [K_b] \{\Phi_i\} = \omega_i^2$, and the damping matrix $[C_b]$ in equation (38) is assumed to be equal to $2\omega_i\eta_i[M_b]$ where ω_i and η_i are the natural circular frequency and the percentage of the critical damping of the i th mode of the bridge, respectively, then equation (39) can be simplified as:

$$\begin{bmatrix} I & \\ & M_v \end{bmatrix} \begin{Bmatrix} \ddot{\xi}_b \\ \ddot{d}_v \end{Bmatrix} + \begin{bmatrix} 2\omega_i\eta_i I + \Phi_b^T C_{b-b} \Phi_b & \Phi_b^T C_{b-v} \\ C_{v-b} \Phi_b & C_v \end{bmatrix} \begin{Bmatrix} \dot{\xi}_b \\ \dot{d}_v \end{Bmatrix} + \begin{bmatrix} \omega_i^2 I + \Phi_b^T K_{b-b} \Phi_b & \Phi_b^T K_{b-v} \\ K_{v-b} \Phi_b & K_v \end{bmatrix} \begin{Bmatrix} \xi_b \\ d_v \end{Bmatrix} = \begin{Bmatrix} \Phi_b^T F_{b-r} \\ F_{v-r} + F_G \end{Bmatrix} \quad (41)$$

The coupled equation (41) contains only the mechanical parameters of vehicles and the modal properties of the bridge. Consequently, the computation cost of solving the coupled equations was considerably reduced. A computer program was developed in the MATLAB environment to solve equation (41) in the time domain using the fourth-order Runge-Kutta

method. After obtaining the displacement responses of the bridge $\{d_b\}$, the strain responses can then be calculated by:

$$\{\varepsilon\} = [B]\{d_b\} \quad (42)$$

where, $[B]$ is the strain-displacement relationship matrix assembled with the x, y, and z derivatives of the element shape functions.

Calibration of the Influence Surface. In the numerical study, five measurement stations (S1, S2, S3, S4, and S5) are selected at the bottom of the five girders (G1, G2, G3, G4, and G5) at the mid-span of the bridge. The longitudinal strains at these measurement stations were recorded. Figure 24 shows the locations of the measurement stations. The vehicle's TP is defined as the distance from the right wheels of the vehicle to the right end of the bridge's cross section as illustrated in Figure 24. In order to generate the influence surface, Truck 2 is used as the calibration truck. A series of TPs ranging from 0.6096 m to 7.62 m with an interval of 0.1524 m is considered in the calibration. These positions cover all cases of the vehicle traveling within the two traffic lanes and bridge shoulders as shown in Figure 24. For each TP, Truck 2 is set to pass the bridge and the bridge response obtained from the simulation is used to extract the influence line corresponding to that TP using the inverse method. The influence ordinates at positions in-between these TPs were obtained using linear interpolations. Figure 25 shows the contour plots of the numerically calibrated influence surface for S2 and S5. It can be seen that the maximum value of the influence surface occurs around positions where the axle load is directly applied above the location of the measurement station.

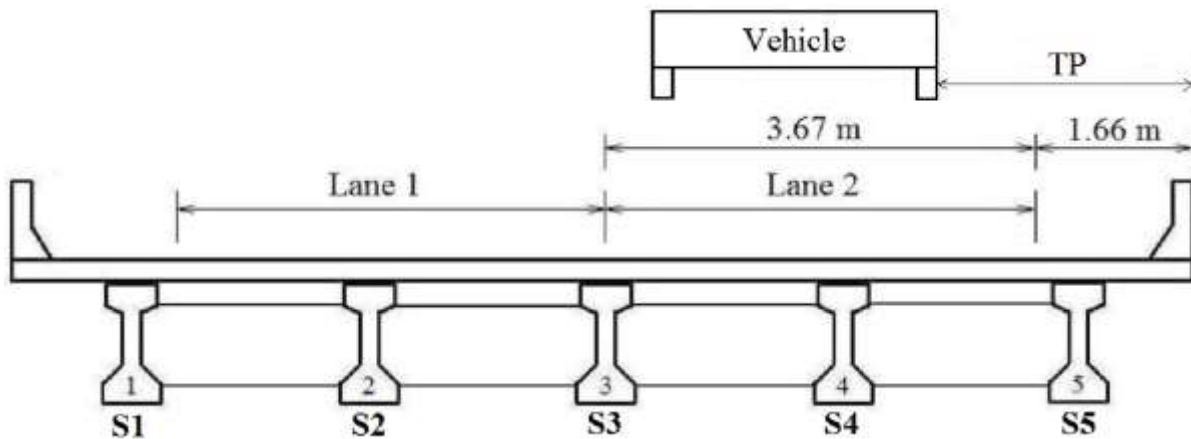


Figure 24
Location of the measurement stations and traffic lanes

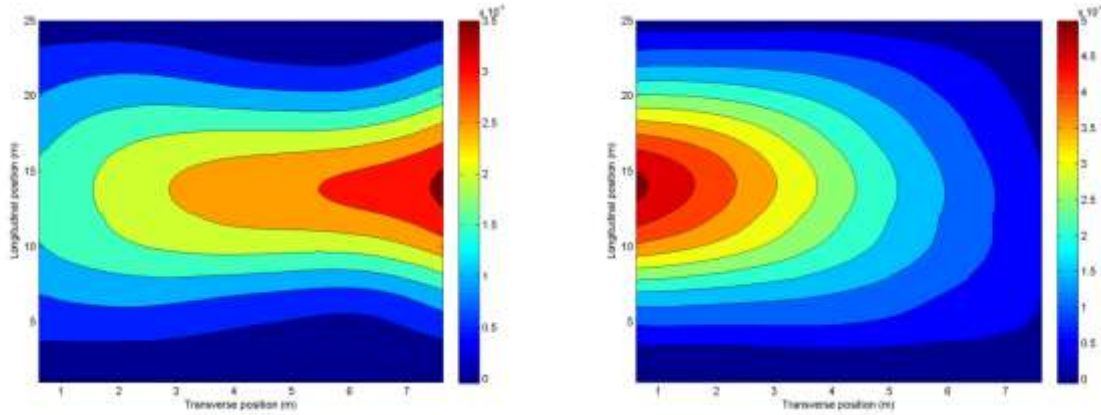


Figure 25

Contour plots of numerically calibrated influence surfaces: (a) S2; (b) S5 (unit: microstrain)

Simulation Results

Axle Detection. In the numerical simulation, each of the four highway trucks are set to cross the bridge at three constant speeds, i.e., 10 m/s, 20 m/s and 30 m/s in lane 2 and Figure 24 shows the transverse position of the vehicle on the bridge. In a commercial BWIM system, five weighing sensors would be installed underneath the five girders at the mid-span to measure the global responses of the bridge, i.e., longitudinal strain responses, and at least four free-of-axle-detector (FAD) sensors (two for each lane) would be installed underneath the bridge slab to identify the vehicle axles. In this study, as an attempt to achieve the NOR BWIM without FAD sensors, the strain signal of the weighing sensor installed on the girder directly beneath the vehicle trajectory, i.e., Girder 4, is used for the axle identification.

Figure 26 shows the typical time histories of the strain response of Girder 4 corresponding to Trucks 2 and 4 traveling at 20 m/s and 10 m/s under a smooth road surface, respectively. A sampling frequency of 200 Hz is used. From the strain response histories, it can be seen that there is no obvious information on the presence of vehicle axles. This is understandable since the longitudinal strain responses of girders are the global responses of the bridge and they are not sensitive to the presence of axle loads. Nevertheless, as discussed before, the details of the original strain signals still contain the information of vehicle axles. Therefore, a CWT is conducted on the strain signals and the results are presented in Figure 26. The plotted wavelet coefficients are chosen at the scale of 14. As can be seen, the transformed signals have several pronounced peaks. These sharp peaks correspond to vehicle axles entering or exiting the bridge. For the three-axle truck, i.e., Truck 2, the first three peaks correspond to the three axles entering the bridge and the last three peaks correspond to the three axles exiting the bridge. Again, the same feature was also observed for the transformed signal for Truck 4, i.e., the five-axle truck.

Since the span length of the bridge is already known, the vehicle speed can be calculated from the time difference between each vehicle axle entering and exiting the bridge. Once the vehicle speed is known, the time difference between vehicle axles can be used to obtain the axle spacing of the truck. For the signals shown in Figure 26, the velocity and two axle spacing of Truck 2 were calculated as 19.85 m/s, 4.22 m and 4.27 m, respectively, and the velocity and four axle spacing of Truck 4 were calculated as 9.92 m/s, 7.96 m, 4.94 m, 1.99 m and 4.94 m, respectively. Compared to the true values given in Table 7, the identified results are found to be very accurate.

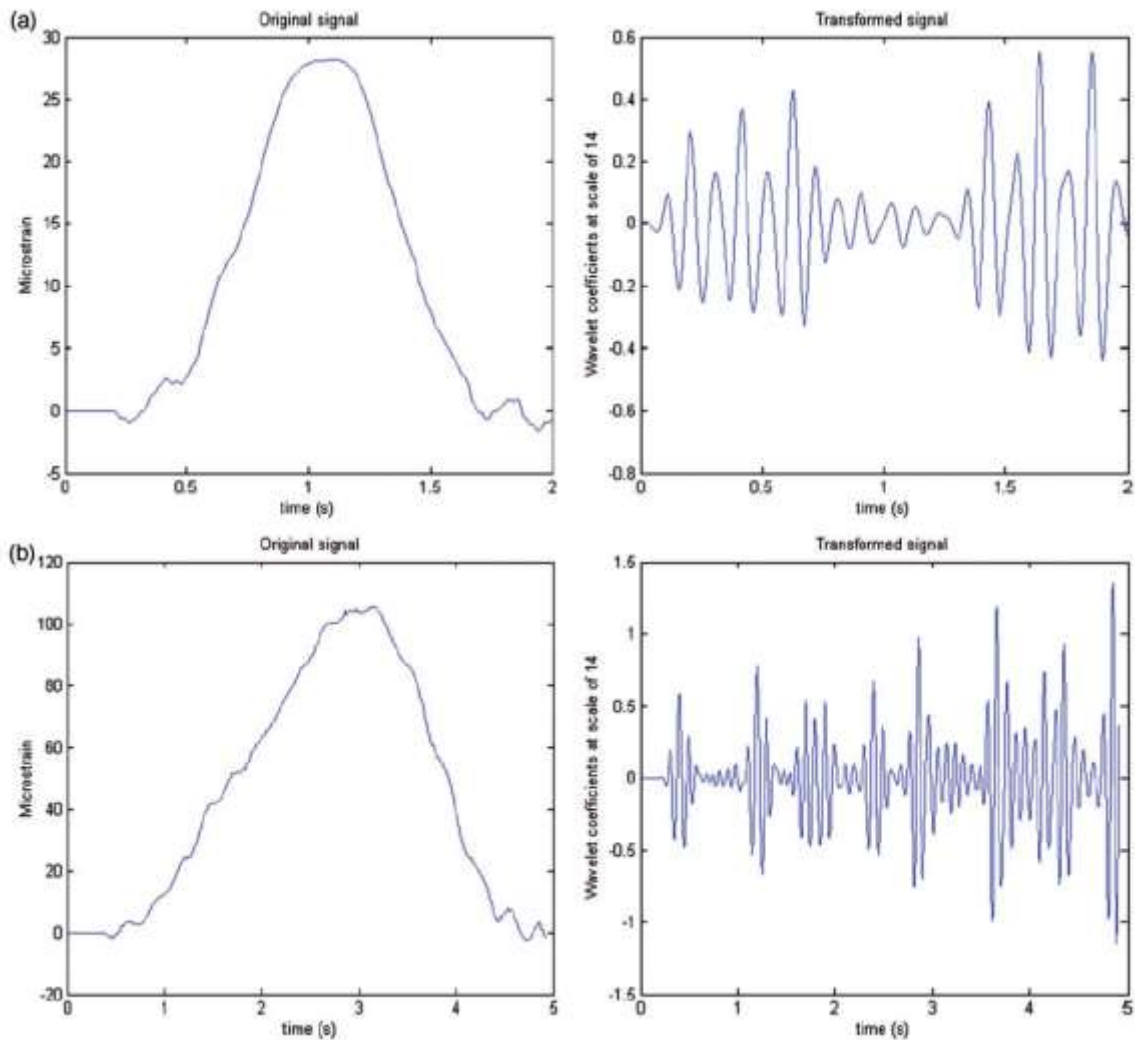


Figure 26

Typical strain signals and corresponding wavelet transformations at scale of 14: (a) Truck 2 (3-axle) traveling at 20 m/s and (b) Truck 4 (5-axle) traveling at 10 m/s

The identification results for all considered cases are tabulated in Table 8. To better examine the accuracy of identification, the identification error is defined as:

$$\text{Identification Error} = \left| \frac{P_{iden} - P_{true}}{P_{true}} \right| \times 100\% \quad (43)$$

where, P_{iden} and P_{true} are the identified parameter and the true parameter, respectively. Using this definition, the identification errors were calculated and the results are given in Table 9.

Table 8
Identified results using wavelet transformation

Truck number	Number of axles	Identified results				
		Velocity (m/s)	Axle spacing First to second (m)	Axle spacing Second to third (m)	Axle spacing Third to fourth (m)	Axle spacing fourth to fifth (m)
1	2	9.93	6.21	N.A.	N.A.	N.A.
2	3	9.92	4.24	4.22	N.A.	N.A.
3	3	9.93	4.86	1.42	N.A.	N.A.
4	5	9.92	7.96	4.94	1.99	4.94
1	2	19.86	6.21	N.A.	N.A.	N.A.
2	3	19.85	4.22	4.27	N.A.	N.A.
3	3	19.85	4.67	1.64	N.A.	N.A.
4	5	19.89	7.96	5.07	1.94	4.92
1	2	29.92	6.28	N.A.	N.A.	N.A.
2	3	29.92	4.19	4.34	N.A.	N.A.
3	3	29.86	6.19	2.76	N.A.	N.A.
4	5	29.88	7.92	4.48	2.39	4.78

Table 9
Identification errors using wavelet transformation

Truck number	Number of axles	Vehicle speed (m/s)	Identification errors (%)				
			Velocity	Axle spacing First to second	Axle spacing Second to third	Axle spacing Third to fourth	Axle spacing fourth to fifth
1	2	10	0.70	0.64	N.A.	N.A.	N.A.
2	3	10	0.80	0.70	1.17	N.A.	N.A.
3	3	10	0.70	1.62	1.43	N.A.	N.A.
4	5	10	0.80	0.50	1.20	0.50	1.20
1	2	20	0.70	0.64	N.A.	N.A.	N.A.
2	3	20	0.75	1.17	0.00	N.A.	N.A.
3	3	20	0.75	5.47	17.1	N.A.	N.A.
4	5	20	0.55	0.50	1.40	3.00	1.60
1	2	30	0.27	0.48	N.A.	N.A.	N.A.
2	3	30	0.27	1.87	1.64	N.A.	N.A.
3	3	30	0.47	25.3	97.1	N.A.	N.A.
4	5	30	0.40	1.00	10.4	19.5	4.40

From Table 9, it can be seen that a satisfactory accuracy was achieved with most errors well below two percent. However, it was found that there are several cases with large identification errors and that these large errors seem to occur at high vehicle speeds. For example, for Truck 3 traveling at 30 m/s, the maximum error of axle spacing reaches 97.1 percent, indicating a failure of identification. The reason for these large errors is that some high-frequency information of the signal is lost due to the relatively low sampling frequency as the vehicle travels at a high speed. It will be shown in the next section that once the sampling frequency is increased; these errors will considerably decrease.

The successful axle identification using bridge global responses has significant implications since the vehicle speed and axle spacing can be identified using only the weighing sensors. In the real application, the use of this advanced axle detection technique will reduce the number of sensors to be installed and thus the cost of BWIM systems. Furthermore, since the identification principle of this technique does not impose any restrictions on bridge types as in the case of FAD applications, it could potentially help extend the application of the BWIM technology to different types of bridges.

Effect of Sampling Frequency. As mentioned earlier, some large errors occurred due to the relatively low sampling frequency. To investigate the effect of sampling frequency on the identification accuracy, two sampling frequencies, i.e., 200 Hz and 500 Hz, are used to record the strain response for Truck 3 traveling at 30 m/s. Figure 27 shows the transformed signals under the two sampling frequencies. It should be mentioned that with the increase of sampling frequency, the scale of wavelet coefficients used for identification is reduced to 4.

From Figure 27, it can be clearly seen that the peaks in the transformed signal corresponding to the sampling frequency of 500 Hz are much sharper than the one corresponding to the sampling frequency of 200 Hz. As a result, the identified vehicle speed and the two axle spacing using the sampling frequency of 500 Hz changed to 30.25 m/s, 4.95 m and 1.42 m, respectively, and corresponding identification errors for the two axle spacing were reduced from 25.3% and 97.1% to 0.20% and 1.43%, respectively. For other cases with relatively large errors, it was also found that increasing the sampling frequency considerably reduced the identification errors.

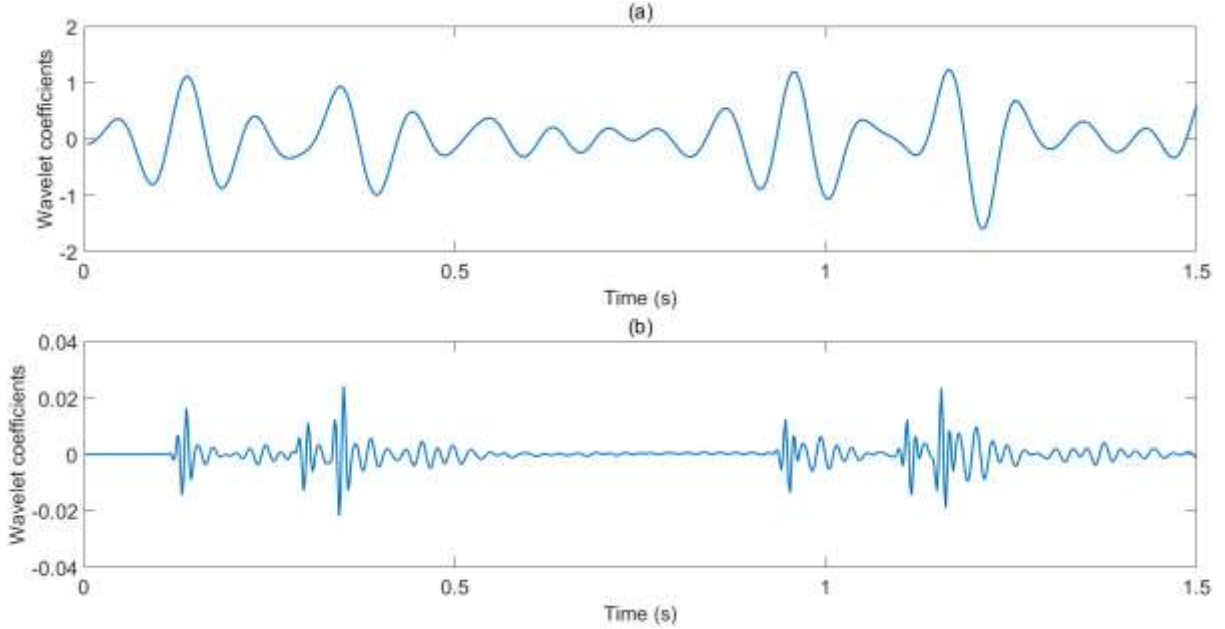


Figure 27

Wavelet transformations of signals for Truck 3 traveling at 30 m/s: (a) sampling frequency of 200 Hz; (b) sampling frequency of 500 Hz

Essentially, increasing the sampling frequency sharpens the peaks in the transformed signal, which, in turn, increases the accuracy of identification. However, higher sampling frequency would also substantially increase the amount of data and its processing time. Therefore, an appropriate sampling frequency should be determined based on the maximum vehicle speed of interest. In addition, this example also demonstrates that the wavelet analysis is capable of identifying closely-spaced axles which can be difficult sometimes for the FAD techniques [13].

Effect of Road Surface Condition. A road profile is usually represented by a zero-mean stationary stochastic process that can be expressed by a power spectral density (PSD) function. In this study, a modified PSD function was used [12]:

$$\varphi(n) = \varphi(n_0) \left(\frac{n}{n_0} \right)^{-2} \quad (n_1 < n < n_2) \quad (44)$$

where, n is the spatial frequency (cycle/m); n_0 is the discontinuity frequency of 0.5π (cycle/m); $\varphi(n_0)$ is the roughness coefficient (m^3/cycle); and n_1 and n_2 are the lower and upper cut-off frequencies, respectively. The International Organization for Standardization classified the road surface condition into several categories depending on different values of roughness coefficients [14]. In the present study, according to ISO specifications, the

roughness coefficients of 5×10^{-6} , 20×10^{-6} , 80×10^{-6} , and 256×10^{-6} m³/cycle were used for very good, good, average, and poor road surface conditions, respectively [14].

The road surface elevation can then be generated by an inverse Fourier transformation as:

$$r(x) = \sum_{k=1}^N \sqrt{2\varphi(n_k)\Delta n} \cos(2\pi n_k x + \theta_k) \quad (45)$$

where, θ_k is the random phase angle uniformly distributed between 0 and 2π ; n_k is the wave number (cycle/m); N is the number of frequencies between n_1 and n_2 ; and Δn is the frequency interval between n_1 and n_2 .

In order to examine the effect of road surface roughness on the identification accuracy, Truck 2 is set to travel at 20 m/s under four different surface conditions, i.e., very good, good, average, and poor road surface conditions and the sampling frequency is chosen to be 500 Hz. The wavelet transformations of the strain signals at the scale of 4 are presented in Figure 28. It can be seen that as the road roughness increases, the peaks used to identify the axles become less pronounced as there appears to have many other “noise” peaks. These other “noise” peaks are caused by the dynamic effect of the vehicle-bridge interaction. As the road surface condition worsens, these “noise” peaks become more pronounced, making the identification more difficult. Nevertheless, under very good and good surface conditions, the identification is still effective, as the identification errors were calculated to be below one percent. However, as road surface condition further deteriorates, the identification becomes infeasible since it is difficult to distinguish the peaks due to vehicle axles from other “noise” peaks caused by the dynamic effect.

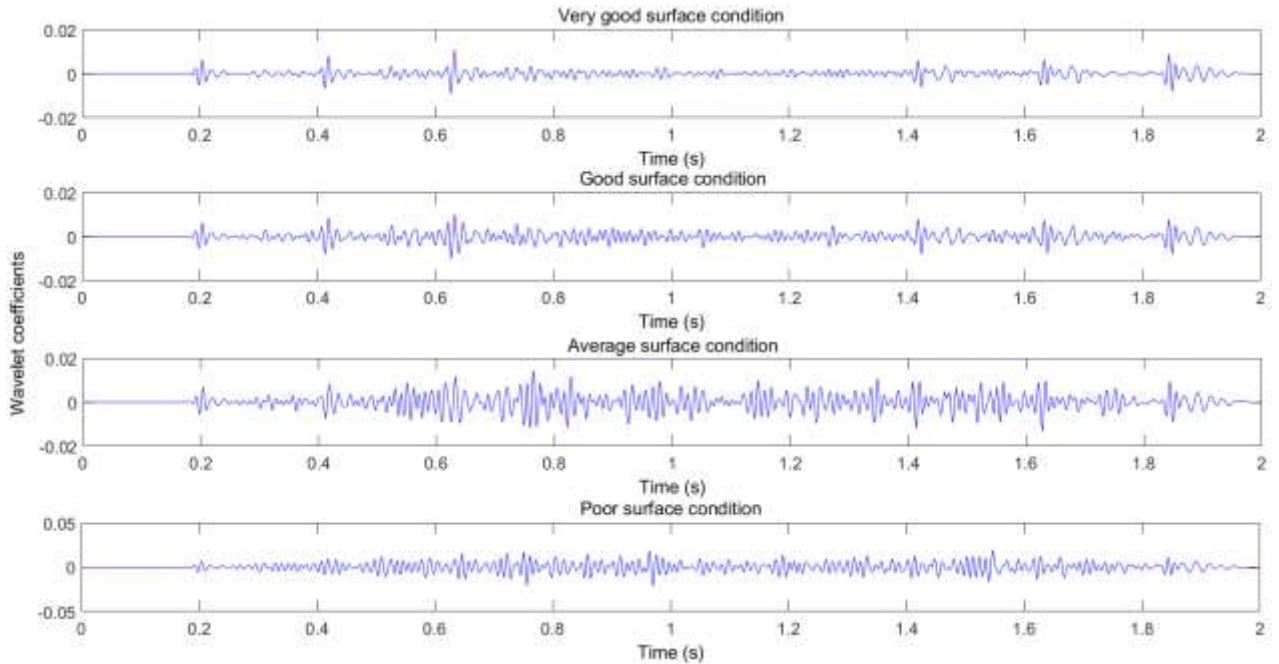


Figure 28

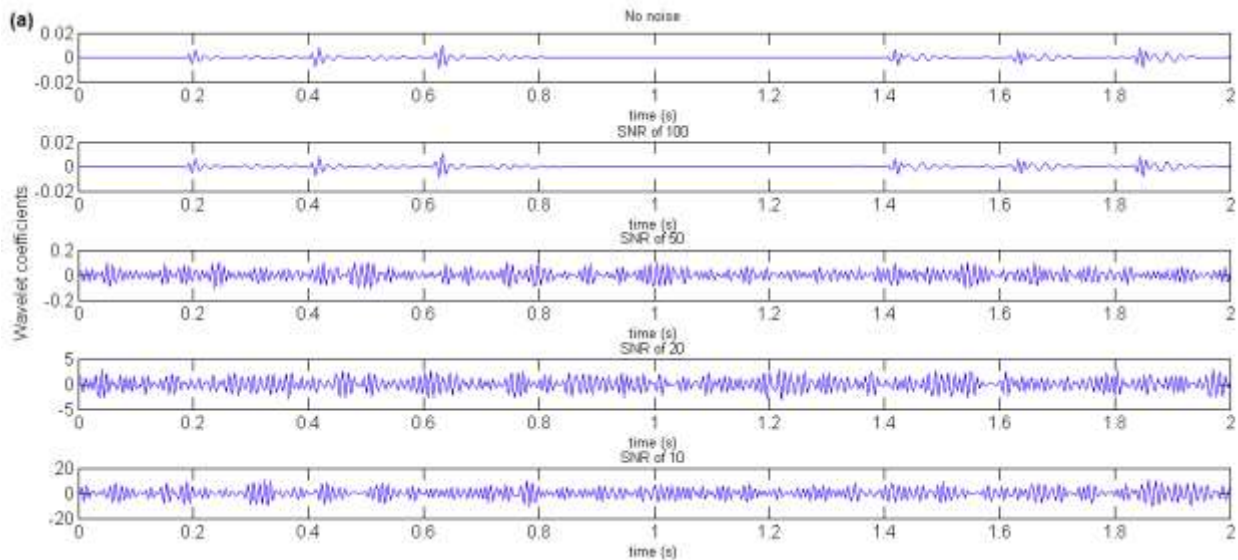
Wavelet transformations of signals under different road surface conditions

In some previous studies on the bridge dynamic behaviors, a low-pass filter was often employed to remove the dynamic effect of the response [12]. However, in the case of axle identifications using wavelet analysis, low-pass filtering is not a solution, since the high frequency components of the signal contain the useful information used to identify the vehicle axles. Namely, low-pass filtering will also filter out the useful information. Nonetheless, it should be pointed out that, a smooth road condition is a prerequisite to achieve a satisfactory identification accuracy for most existing BWIM technologies such as those using Moses's algorithm [8]. Therefore, the fact that the axle identification using wavelet analysis is limited to good bridge surface conditions does not really impede the implementation of modern commercial BWIM systems whose basic framework is the Moses's algorithm [8]. Naturally, a new methodology that can work well under rough road surface conditions, and at the same time can eliminate the axle detection sensors, is very desirable.

Effect of Measurement Noise. While the results above can be very accurate for good road surface conditions, they are obtained in the ideal situation. In real practice, the obtained signals are usually contaminated by measurement noises induced by the environmental changes and electric devices used for data acquisition. Thus, it is necessary to examine the effect of measurement noise on the identification accuracy. For this purpose, different levels of Gaussian white noise are added to the original strain signal obtained when Truck 2 travels at 20 m/s under sampling frequencies of 500 Hz and 200 Hz. As mentioned before, the scale

of the wavelet coefficients for the two frequencies are 4 and 14, respectively. Figure 29 shows the wavelet transformations of the original signal and polluted signals under four different signal-to-noise ratios (SNRs) of 100, 50, 20 and 10.

From Figure 29 (a), it can be seen that under the sampling frequency of 500 Hz, the peaks induced by the vehicle axles quickly get submerged by the noise as the noise level increases, making the identification impossible. This suggests that the identification method is sensitive to the measurement noise. The main reason for this is that the information of vehicle axles is reflected by very delicate changes in the original signal. Therefore, it becomes very difficult to separate this information from the measurement noises even through de-noising techniques that allow the preservation of certain features of the original signal, such as median filter and wavelet de-noising.



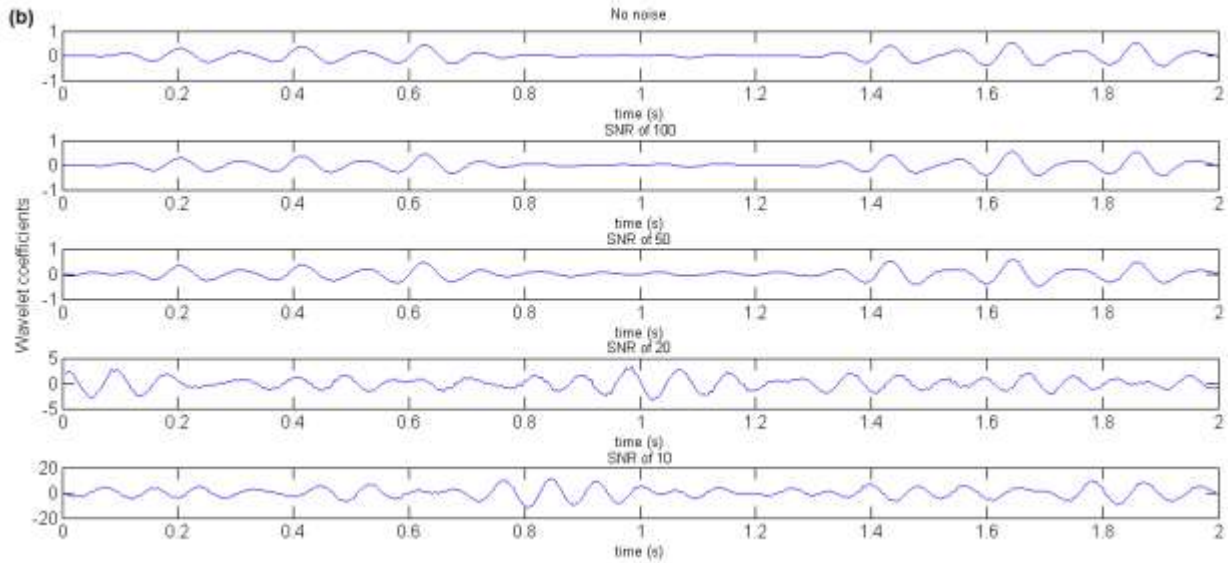


Figure 29

Wavelet transformations of signals under different levels of noise: (a) sampling frequency of 500 Hz; (b) sampling frequency of 200 Hz

Nevertheless, it was also noticed from Figure 29 (b) that as the sampling frequency decreases to 200 Hz, the peaks induced by the vehicle axles tend to get submerged more slowly than the previous case, i.e., the identification becomes less susceptible to the noise under a lower sampling frequency. This is because while the scale of the noise remains the same, the scale of the peaks increased due to the lower sampling frequency. From this perspective, increasing the sampling frequency, though it sharpens the peaks induced by the vehicle axles, it does not necessarily increase the identification accuracy. Therefore, the choice of an optimal sampling frequency should take into consideration the maximum vehicle speed of interest as well as the level of noise.

2D BWIM Algorithm

Numerical simulations were conducted on the simply supported beam-slab bridge. Seven loading cases were considered with each case corresponding to the vehicle traveling at a different TP based on the location of traffic lanes. As shown in Figure 24, two traffic lanes, each with a width of 3.67 m, were designed for the bridge. The first three loading cases correspond to the vehicle traveling at the center of Lane 1, the vehicle's right wheel traveling at the right side of Lane 1, and the vehicle's left wheel traveling at the left side of the Lane 1. The second three cases correspond to the same vehicle layout as the first three cases but in Lane 2. Case 7 corresponds to a special case where the vehicle travels at the center of the bridge. Table 10 summarizes the description of the seven loading cases. In the following study, the vehicle is set to travel at a constant speed of 10 m/s under a smooth road surface profile unless otherwise specified in the parametric study.

Table 10
Description of loading cases considered in the simulation

Case Number	Traveling Lane	Transverse position, x (m)
1	Lane 1	1.676
2	Lane 1	2.286
3	Lane 1	2.896
4	Lane 2	5.334
5	Lane 2	5.944
6	Lane 2	6.553
7	Lane 1 and Lane 2	4.115

To identify the TP of the vehicle, the measurement station of the largest response is first used to calculate the set of axle weights for an assumed TP. Then, the obtained set of axle weights are used to predict the responses for other measurement stations using the calibrated influence surface and the results are substituted into equation (27) to calculate the value of the error function at the assumed TP. The same procedure is repeated for all possible TPs and the one that gives the minimum value of the error function is identified as the true TP of the vehicle. For example, Figure 30 shows the variation of the error function with the possible TPs for Case 2 with Truck 4 and Case 4 with Truck 1. It can be seen that the minimum value of the error function is achieved at a specific TP. In Figure 30 (a) and (b), the two TPs that minimize the error function are 2.286 m and 5.334 m, respectively, corresponding to the true TPs of the vehicle for the two cases. It should be noted that the reason for not plotting all possible TPs in Figure 30 is that the values of the error function at positions far away from the true TP is so large that plotting them in the figure would make it difficult to visually identify the minimum value of the error function.

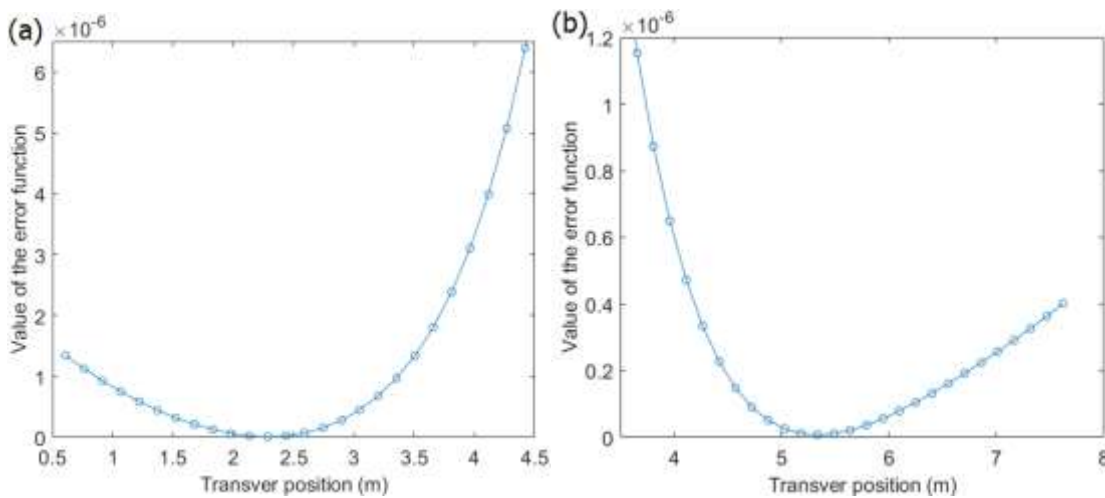
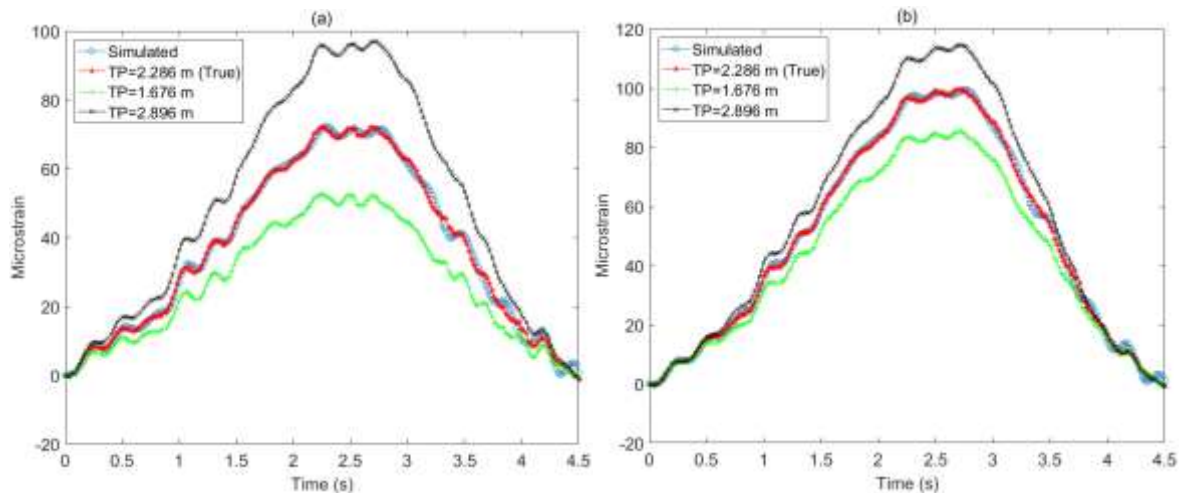


Figure 30
Variation of the error function with respect to the possible TPs of the vehicle: (a) Case 2 with Truck 4; (b) Case 4 with Truck 1

To better illustrate the identification principle, Figure 31 plots the simulated responses and the reconstructed responses obtained using the axle weights identified at different TPs of different measurement stations under Case 2 with Truck 4. Only the responses corresponding to the true TP and two other assumed TPs are plotted for visualization purposes. For Case 2, Girder 5 had the largest response. Therefore, S5 was selected as the weighing station. It can be seen from Figure 31 (e) that the reconstructed responses corresponding to different TPs uniformly match the simulated response very well for S5, i.e., the weighing station. However, this is not the case for other measurement stations. As can be seen from Figure 31, the degree of match between the simulated and reconstructed responses gradually decreases as the location of the measurement station gets further away from S5 with the exception of the reconstructed responses obtained using the axle weights identified at the true TP. This is because if the assumed TP is not the true one, the axle weights will either be over- or underestimated depending on the assumed TP in order to match the simulated response of S5, which in turn causes a mismatch between the simulated and reconstructed responses for other measurement stations. In other words, only the axle weights identified at the true TP will be able to achieve a good match between the simulated and reconstructed responses for all measurement stations.



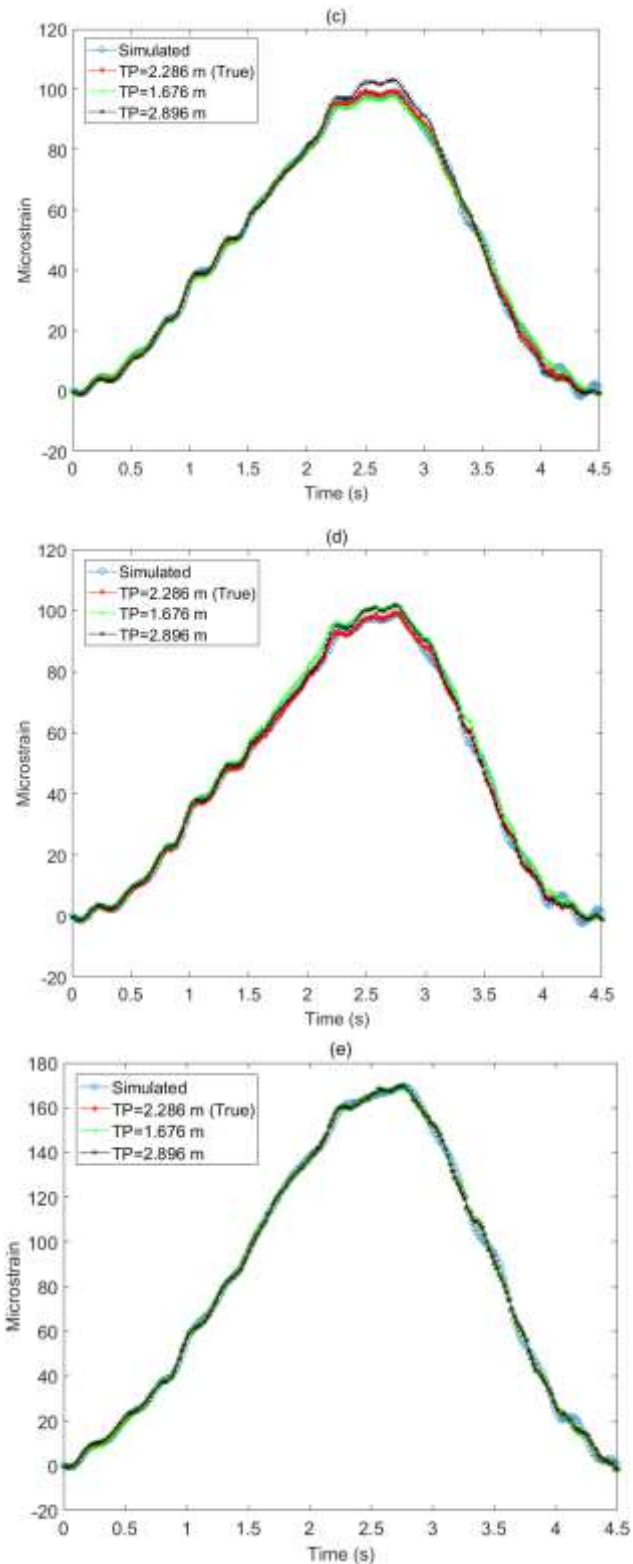


Figure 31
Simulated and reconstructed bridge responses of different measurement stations for Case 2 with Truck 4: (a) S1; (b) S2; (c) S3; (d) S4; (e) S5

The proposed algorithm was implemented for all seven loading cases using the three highway trucks, i.e., Trucks 1, 2 and 4 shown in Table 7. The identification results are given in Table 11 with the identified values of vehicle weights rounded to one decimal place. To better examine the identification accuracy, the identification error is defined as:

$$Identification\ Error = \left| \frac{P_{iden} - P_{true}}{P_{true}} \right| \times 100\% \quad (46)$$

where, P_{iden} and P_{true} are the identified parameter and the true parameter, respectively. Using this definition, the identification errors of the vehicle's TP, axle weights and gross vehicle weight (GVW) were calculated and the results are given in Table 12. It should be mentioned that the errors were calculated using the identified values before the rounding. In order to compare the identification accuracy between the proposed algorithm and the 1D Moses's algorithm, the identification was also conducted using the Moses's algorithm and the identification errors are also given in Table 12. It should be noted that for the Moses's algorithm, the axle weights are identified using the total response of the bridge and in this case, the influence lines under the vehicle traveling at the center of the bridge were used to predict the total response of the bridge.

Table 11
Identification results using the proposed algorithm

Case Number	Truck Number	Identified TP of the vehicle (m)	Identified vehicle weights (kN)					GVW
			First axle	Second axle	Third axle	Fourth axle	Fifth axle	
1	1	1.676	125.9	145.9	N.A.	N.A.	N.A.	271.8
	2	1.676	35.5	141.9	142.3	N.A.	N.A.	319.7
	4	1.676	125.8	178.3	106.7	117.7	161.9	690.4
2	1	2.286	125.9	145.9	N.A.	N.A.	N.A.	271.8
	2	2.286	35.5	141.9	142.3	N.A.	N.A.	319.7
	4	2.286	125.8	178.6	105.1	119.5	161.5	690.5
3	1	2.896	125.9	145.9	N.A.	N.A.	N.A.	271.8
	2	2.896	35.6	141.9	142.3	N.A.	N.A.	319.8
	4	2.896	125.8	179.2	102.2	122.6	160.8	690.6
4	1	5.334	125.9	145.9	N.A.	N.A.	N.A.	271.8
	2	5.334	35.6	141.9	142.3	N.A.	N.A.	319.8
	4	5.334	125.8	179.2	102.5	122.3	160.8	690.6
5	1	5.944	125.9	145.9	N.A.	N.A.	N.A.	271.8
	2	5.944	35.5	141.9	142.3	N.A.	N.A.	319.7
	4	5.944	125.8	178.6	105.3	119.3	161.6	690.6
6	1	6.553	125.9	145.9	N.A.	N.A.	N.A.	271.8
	2	6.553	35.5	141.9	142.3	N.A.	N.A.	319.7
	4	6.553	125.8	178.3	106.8	117.6	162.0	690.5

	1	4.115	126.0	146.0	N.A.	N.A.	N.A.	272.0
7	2	4.115	35.5	142.0	142.2	N.A.	N.A.	319.7
	4	4.115	125.6	179.8	102.6	121.1	161.5	690.6

Table 12
Comparison of identification errors between the Moses's algorithm and the proposed algorithm

Case Number	Truck Number	Moses's algorithm (%)						Proposed algorithm (%)						
		1st axle	2nd axle	3rd axle	4th axle	5th axle	GVW	TP	1st axle	2nd axle	3rd axle	4th axle	5th axle	GVW
1	1	4.12	5.39	N.A.	N.A.	N.A.	4.80	0.00	0.21	0.00	N.A.	N.A.	N.A.	0.10
	2	19.5	2.19	8.91	N.A.	N.A.	5.16	0.00	0.08	0.04	0.02	N.A.	N.A.	0.00
	4	3.86	5.55	4.38	2.85	6.96	4.92	0.00	0.36	0.78	2.74	2.10	0.46	0.11
2	1	2.71	3.85	N.A.	N.A.	N.A.	3.32	0.00	0.22	0.00	N.A.	N.A.	N.A.	0.10
	2	10.4	0.56	5.74	N.A.	N.A.	3.46	0.00	0.11	0.05	0.03	N.A.	N.A.	0.01
	4	2.20	4.09	0.94	5.60	4.16	3.27	0.00	0.39	0.58	1.17	0.63	0.21	0.11
3	1	1.73	2.09	N.A.	N.A.	N.A.	1.92	0.00	0.22	0.02	N.A.	N.A.	N.A.	0.09
	2	9.34	1.54	3.83	N.A.	N.A.	2.06	0.00	0.20	0.09	0.05	N.A.	N.A.	0.01
	4	1.09	2.71	2.61	4.72	2.33	1.87	0.00	0.43	0.26	1.62	2.01	0.27	0.10
4	1	0.05	1.01	N.A.	N.A.	N.A.	0.52	0.00	0.22	0.01	N.A.	N.A.	N.A.	0.09
	2	6.72	2.98	2.71	N.A.	N.A.	0.63	0.00	0.19	0.08	0.05	N.A.	N.A.	0.01
	4	0.53	1.40	5.09	4.07	1.05	0.46	0.00	0.42	0.30	1.30	1.70	0.22	0.10
5	1	0.52	2.72	N.A.	N.A.	N.A.	1.70	0.00	0.21	0.00	N.A.	N.A.	N.A.	0.10
	2	7.42	2.43	4.66	N.A.	N.A.	1.82	0.00	0.11	0.05	0.03	N.A.	N.A.	0.01
	4	0.28	2.60	3.94	4.87	2.81	1.64	0.00	0.38	0.60	1.35	0.80	0.24	0.11
6	1	2.04	4.62	N.A.	N.A.	N.A.	3.43	0.00	0.21	0.00	N.A.	N.A.	N.A.	0.10
	2	18.5	4.63	8.61	N.A.	N.A.	3.83	0.00	0.08	0.04	0.02	N.A.	N.A.	0.00
	4	2.16	4.35	2.36	1.43	6.26	3.59	0.00	0.36	0.79	2.80	2.16	0.47	0.12
7	1	0.24	0.01	N.A.	N.A.	N.A.	0.11	0.00	0.24	0.10	N.A.	N.A.	N.A.	0.16
	2	0.10	0.04	0.03	N.A.	N.A.	0.01	0.00	0.09	0.03	0.02	N.A.	N.A.	0.00
	4	0.78	0.91	8.43	7.44	1.03	0.12	0.00	0.54	0.08	1.20	0.75	0.19	0.09

From Table 12, it can be seen that the proposed algorithm successfully identified the true TPs of the vehicle for all cases. For the axle weights and GVW, most errors are within one percent, indicating a very accurate identification. Slightly larger errors were observed for the third and fourth axles of Truck 4. This is because the third and fourth axles of Truck 4 are closely spaced at a distance of two

meters and it has been found that accurately identifying the weights of closely spaced axles is very difficult [15,16]. Actually, closely spaced axles forming an axle group are usually identified as a single axle in practice. In the case of the Moses's algorithm, the identification errors of axle weights and GVW seem to be related with the TP of the vehicle. The errors appear to decrease as the TP gets closer to the center of the bridge, i.e., the TP corresponding to which the influence lines were selected to predict the total response of the bridge. As a matter of fact, accurate identification of axle weights and GVW was achieved using the Moses's algorithm for Case 7 in which the vehicle was located at the center of the bridge. Nevertheless, the identification errors using the Moses's algorithm are generally much higher than those using the proposed algorithm. This suggests that the TP of the vehicle has a significant influence on the identification accuracy. From this perspective, the vehicle's TP should be considered in the identification of axle weights. Therefore, an algorithm that is able to identify the vehicle's TP such as the proposed one should be able to improve the identification accuracy compared with the 1D Moses's algorithm in practice.

Effect of Road Surface Condition. In order to examine the effect of the road surface condition on the identification accuracy, Truck 4 was set to travel under four different road surface conditions: very good, good, average, and poor conditions; the identification was conducted under Case 5. The identification errors are summarized in Table 13. It can be seen that although the identification of the GVW remains accurate, the identification errors of axle weights increases significantly as the road surface condition worsens. This is because the dynamic effect of the vehicle was induced by the road surface roughness, which causes the simulated response to deviate from the predicted response obtained using the influence surface, resulting in larger identification errors. In fact, the accurate identification of axle weights under rough surface conditions remains a challenging issue to modern commercial BWIM systems. Usually, a good road surface condition is the prerequisite of achieving satisfactory identification accuracy [17]. Nevertheless, the vehicle's TP was successfully identified regardless of the road surface conditions used, implying that the proposed algorithm is robust in identifying the TP of the vehicle.

Table 13
Identification errors for Case 5 with Truck 4 traveling under different road surface conditions

Road surface condition	TP (%)	Axle weights (%)					GVW (%)
		First axle	Second axle	Third axle	Fourth axle	Fifth axle	
Smooth	0.00	0.38	0.60	1.35	0.80	0.24	0.11
Very good	0.00	1.71	4.33	28.39	22.95	3.00	0.16
Good	0.00	2.46	7.30	47.87	39.17	5.47	0.21
Average	0.00	3.94	13.23	86.83	71.62	10.42	0.30
Poor	0.00	6.30	22.58	148.3	122.8	18.21	0.45

In order to reduce the influence of the road roughness, a low-pass filter can be applied to remove the dynamic effect. Based on trial and error, a cut-off frequency of 1.5 Hz was chosen for the low-pass filter as this frequency can effectively remove the dynamic components of the response and leave the static components intact. Table 14 gives the identification errors after the simulated responses were filtered. Comparing Table 14 with Table 13, it was found that the identification accuracy was considerably improved after the application of the low-pass filter. In addition, it is interesting to note that the identification errors for the third and fourth axles under the smooth surface condition actually increased after the filtering probably because the low-pass filtering blurred the distinction between the effects of the closely spaced axles, which are reflected in the high-frequency components of the response [15]. For this reason, it was suggested that the low-pass filtering only be used for bridges with high fundamental frequencies [15]. Nevertheless, the low-pass filter is able to improve the identification accuracy overall in the present study.

Table 14
Identification errors for Case 5 with Truck 4 traveling under different road surface conditions using filtered responses

Road surface condition	TP (%)	Axle weights (%)					GVW (%)
		First axle	Second axle	Third axle	Fourth axle	Fifth axle	
Smooth	0.00	0.16	1.47	6.08	4.43	0.65	0.12
Very good	0.00	0.78	1.10	8.19	6.67	0.79	0.11
Good	0.00	0.80	1.33	9.57	8.03	1.12	0.10
Average	0.00	0.83	1.79	12.32	10.74	1.77	0.08
Poor	0.00	0.87	2.47	16.49	14.88	2.78	0.06

Additionally, it is conceivable that the measurement noise will also have an impact on the identification accuracy and the effect of the measurement noise is, to some degree, similar to that of the road surface roughness in a way that they all cause deviations to the measured

static response. Similarly, a low-pass filter can be used to remove the high-frequency noise and thus improve the identification accuracy. For the sake of simplicity, the effect of the measurement noise on the identification accuracy is not further discussed here.

Effect of Vehicle Speed. In order to determine the effect of the vehicle speed on the identification accuracy, Truck 2 was set to travel at six different speeds ranging from 5 m/s to 30 m/s with an interval of 5 m/s. The identification was conducted under Case 2. The identification errors are given in Table 15. It can be seen that the TP of the vehicle was successfully identified for all considered speeds and that most identification errors for axle weights and GVW are within one percent. Moreover, vehicle traveling at speeds higher than 10 m/s appears to cause slightly larger errors in the identified axle weights. This is because higher speeds induced the dynamic effect of the vehicle while this effect is basically negligible for the vehicle traveling at lower speeds. However, the dynamic effect does not necessarily become more evident as the vehicle speed increases. In fact, the largest errors occur at the vehicle speed of 15 m/s. A possible explanation for this is that the excitation frequency of the vehicle at this speed approached the fundamental frequency of the bridge, which led to the resonant vibration of the bridge. The excitation frequency of the vehicle may be calculated using the following equation [18]:

$$f_{ex} = \frac{v}{L_v} n \quad (n=1,2,3,\dots) \quad (47)$$

where, v is the vehicle speed; L_v is the vehicle's axle spacing which is uniformly 4.27 m for Truck 2; and f_{ex} is the excitation frequency of the vehicle. When the vehicle speed is 15 m/s, the excitation frequency is calculated to be 3.51 Hz, which is very close to the fundamental frequency of the bridge of 3.46 Hz. Therefore, the larger identification errors at this speed may be contributed to the stronger dynamic effect caused by the resonance. Nevertheless, accurate identification was achieved for various vehicle speeds, indicating that the vehicle speed does not have a significant influence on the identification accuracy.

Table 15
Identification errors for Case 2 with Truck 2 traveling at different vehicle speeds

Vehicle speed (m/s)	TP (%)	Axle weights (%)			GVW (%)
		First axle	Second axle	Third axle	
5	0.00	0.02	0.01	0.00	0.00
10	0.00	0.11	0.05	0.03	0.01
15	0.00	1.56	0.66	0.39	0.05
20	0.00	0.38	0.15	0.08	0.01
25	0.00	1.01	0.46	0.28	0.04
30	0.00	0.37	0.19	0.13	0.01

Effect of Vehicle Width. In the present study, the truck used to calibrate the influence surface has a width of 2.5 m. However, the vehicle width varies between different vehicles in practice and it is conceivable that this variation will result in identification errors. Nevertheless, it has been found that the variation of the width of commercial trucks is very small. The survey by Berard and Bourion showed that the mean width of heavy trucks is 2.52 m with approximately ninety percent of the widths falling within the range from 2.5 m to 2.6 m [19]. Furthermore, according to the latest Federal Size Regulations for Commercial Motor Vehicles, the maximum width of commercial trucks is established at 2.6 m [20].

To examine the effect of the vehicle width on the identification accuracy, a series of vehicle widths ranging from 2.3 m to 2.7 m with an interval of 0.1 m was set for Truck 2. The identification was conducted under Case 6 and the identification errors are summarized in Table 16. It can be seen that the TP of the vehicle was successfully identified except for vehicle widths of 2.3 m and 2.7 m where a negligible error of 0.02 % was obtained. The variation of identification errors of axle weights and GVW with respect to the vehicle width is plotted in Figure 32. It can be observed that the identification errors increase as the vehicle width deviates from 2.5 m, the original vehicle width that was used in the calibration of the influence surface. Nevertheless, even with the varying vehicle width, the identification of axle weights and GVW was still accurate with the maximum error within four percent. This suggests that the vehicle width will not have a significant effect on the identification accuracy in practice.

Table 16
Identification errors for Case 6 with Truck 2 using different vehicle widths

Vehicle width (m)	TP (%)	Axle weights (%)			GVW (%)
		First axle	Second axle	Third axle	
2.3	0.02	2.37	1.98	0.91	1.02
2.4	0.00	0.53	1.03	0.26	0.28
2.5	0.00	0.08	0.04	0.02	0.00
2.6	0.00	0.10	0.86	0.19	0.29
2.7	0.02	3.41	2.30	0.68	0.95

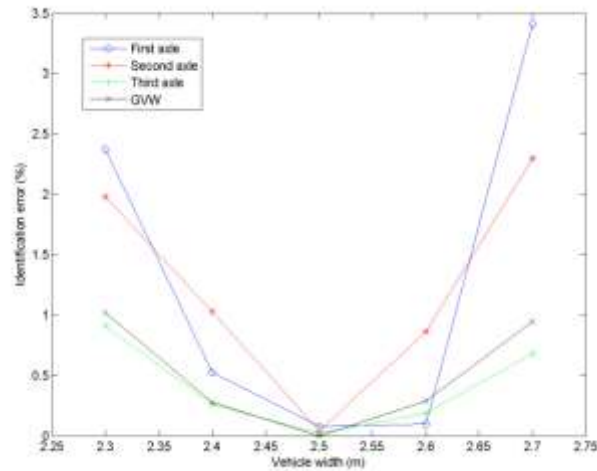


Figure 32
Variation of identification errors of axle weights and GVW with respect to the vehicle width for Case 6 with Truck 2

Effect of Different Measurement Stations. In previous identifications, the measurement station of the largest response was selected as the weighing station while other stations were used to identify the TP. In order to investigate the effect of using different measurement stations as the weighing station, Truck 2 was set to run under Case 1 and the identification was conducted using each measurement station as the weighing station. In this case, S5 had the largest response while the responses of S3 and S4 were smaller than that of S5 but close. The responses of S1 and S2 were noticeably smaller than those of other measurement stations. Table 17 lists the identification errors obtained using different weighing stations. It can be seen that the TP of the vehicle was successfully identified regardless of the weighing stations selected and that accurate identification of axle weights and GVW was achieved with the maximum error within one percent. Nevertheless, the identification of axle weights and GVW seems more accurate when S3, S4 and S5, i.e., measurement stations underneath the traveling lane, were respectively selected as the weighing station. To a certain degree, this implies that using measurement stations of smaller responses as the weighing station may lead to larger identification errors of axle weights and GVW. As a general rule of thumb, the measurement station of the largest response is preferred for the selection of the weighing station in order to facilitate the implementation in practice.

Table 17
Identification errors for Case 1 with Truck 2 using different weighing stations

Weighing stations	TP (%)	Axle weights (%)			GVW (%)
		First axle	Second axle	Third axle	
S1	0.00	0.69	0.30	0.18	0.02
S2	0.00	0.32	0.14	0.09	0.01
S3	0.00	0.03	0.01	0.00	0.00
S4	0.00	0.04	0.02	0.01	0.00
S5	0.00	0.08	0.04	0.02	0.00

Verification by a Field Study

Tested Bridge. In order to verify the effectiveness of the proposed algorithm in practice, the proposed algorithm was demonstrated using a previously conducted field test. The field test was conducted on a beam-slab bridge in 2006. The tested bridge is located over Cypress Bayou in District 61, on LA 408 East, Louisiana. The bridge has three simply supported spans and all three spans have an identical length of 16.764 m with zero skew angles as shown in Figure 33. The bridge consists of seven AASHTO Type-II prestressed concrete girders with a center-to-center spacing of 2.13 m. The girders are supported by rubber bearings at both ends of the bridge. For each span, three intermediate diaphragms are located at the mid-span and the two ends of the bridge, separated from the bridge deck. The cross section and the lane arrangement of the bridge are shown in Figure 34.

The third span of the bridge was instrumented. Seven strain gauges were installed at the bottom of the seven girders to measure the longitudinal strains. These strain gages were installed 0.305 m away from the mid-span of the bridge in order to avoid stress concentrations caused by the diaphragms placed at the mid-span. Therefore, a total of seven measurement stations (S1, S2, S3, S4, S5, S6, and S7) were selected corresponding to the seven girders G1, G2, G3, G4, G5, G6, and G7.

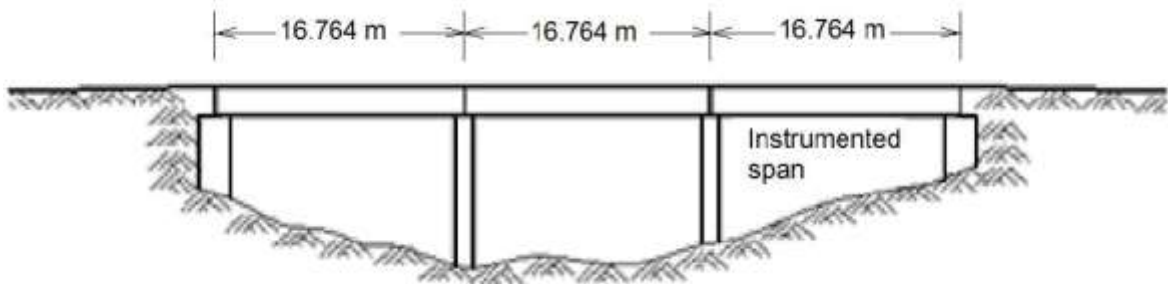


Figure 33
Longitudinal profile of the tested bridge

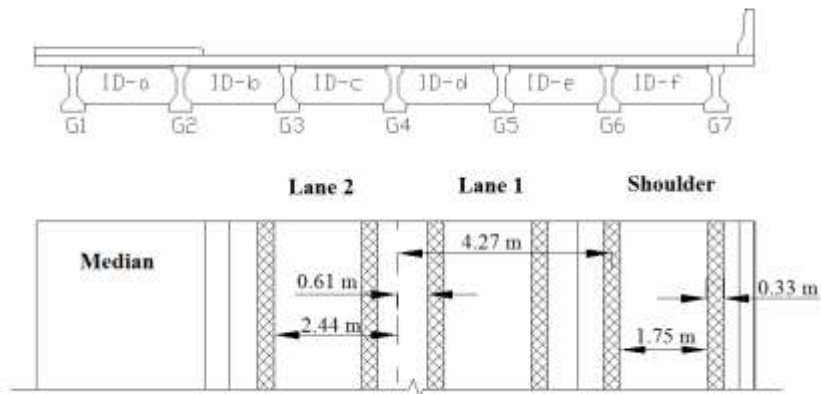


Figure 34
Cross section and lane arrangement of the tested bridge

Test Vehicle. In the field test, a dump truck with a single front axle and a rear two-axle group as shown in Figure 35 was used as the test vehicle. The static loads for the first, second, and third axles of the test truck are 80.0 kN, 95.6 kN, and 95.6 kN, respectively. The axle spacing between the first axle and the center of the rear axle group is 6.25 m, and the distance between the two rear axles is 1.2 m. The width of the test vehicle is 2.41 m. Chan and O’Conner found that the axles within a group can be replaced by a single axle acting at the center of the group if the axles within the group are closely spaced [21]. Therefore, the two rear axles of the test truck are replaced by one equivalent axle in order to simply the identification in this study.



Figure 35
The test vehicle

Field Calibration of Influence Surface. Six testing cases (three static and three dynamic tests) were considered in the field testing. A brief description of the testing cases is given in Table 18. Detailed testing setups can be found in Reference [22]. The first three cases correspond to the static testing with three different TPs of the vehicle. The responses obtained from these three cases were used to calibrate the influence surface as the dynamic effect was very small during the static testing. For each TP, the corresponding influence line was calculated from the measured bridge response using the method proposed by O'Brien et al. [23]. Previous experimental studies found that a cubic spline function is suitable for the interpolation of influence ordinates at positions in-between the measured TPs in field calibrations [15, 24]. Therefore, a spline interpolation was adopted in the current study to form a continuous influence surface using the field calibrated influence lines obtained at different TPs. Figure 36 shows the contour plots of the field calibrated influence surfaces for S4 and S6.

Table 18
Description of testing cases

Case number	Testing type	Traveling Lane	Transverse position (m)	Velocity (m/s)
Case 1	static	Shoulder	0.914	2.24
Case 2	static	Lane 1	4.420	2.24
Case 3	static	Lane 2	7.798	2.24
Case 4	dynamic	Lane 1	4.420	13.41
Case 5	dynamic	Lane 1	4.420	17.88
Case 6	dynamic	Lane 2	7.798	17.21

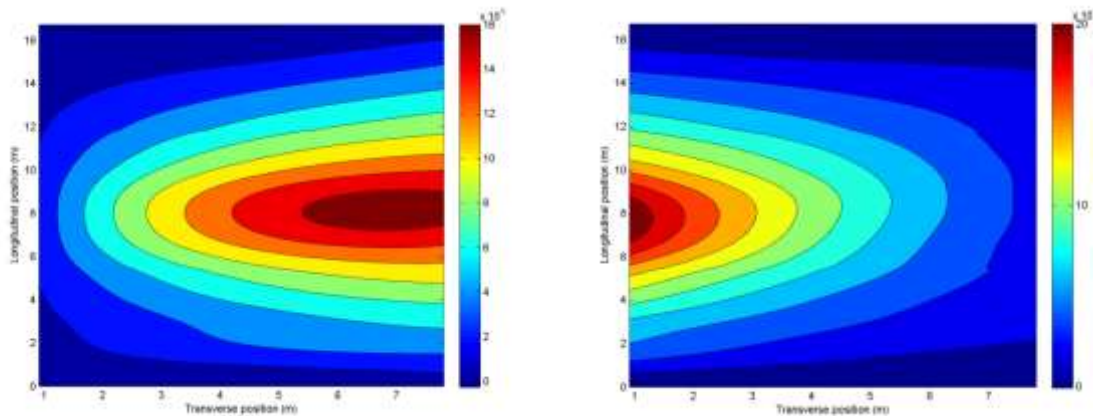


Figure 36
Contour plots of field calibrated influence surfaces: (a) S4; (b) S6 (unit: microstrain)

Identification Results. The proposed algorithm was used to identify the TP and axle weights of the test truck for all considered cases. For Case 2, Case 4 and Case 5, S5 had the

largest response and thus S5 was selected as the weighing station. Similarly, S3 was selected as the weighing station for Case 3 and Case 6 while S7 was selected as the weighing station for Case 1. Based on the proposed algorithm, the measurement stations other than the weighing station will be used to identify the vehicle's TP. Nevertheless, it was found that in each case, the response of the station furthest from the test vehicle is so small that significant variations were observed in the response. Thus, the furthest measurement station from the test truck was not used for the identification in order to reduce the effect of measurement errors.

The identification results and corresponding errors are shown in Table 19. It can be seen that the identification errors for the first three cases, i.e., the static testing cases, are basically negligible as expected. For the dynamic testing cases, it was observed that the identification errors of the TP are approximately within four percent while the errors of axle weights and GVW for most cases are within four percent as well. In fact, the only case where the error of axle weights and GVW exceeded four percent is Case 6. This is probably because the vehicle speed for Case 6 was not well controlled according to the record. Nevertheless, the identification accuracy achieved using the proposed algorithm is acceptable in practice.

In addition, another approach to examine the identification accuracy is to reconstruct the bridge response using the identified TP and axle weights of the vehicle and compare it with the measured response. Figure 37 shows the comparison between the measured response and the reconstructed response of the weighing station for Case 4 and Case 6. It can be seen that a good match between the measured and reconstructed responses is achieved.

Table 19
Identification results and corresponding errors

Case Number	Transverse position		First axle		Second axle		GVW	
	Value (m)	Error (%)	Value (kN)	Error (%)	Value (kN)	Error (%)	Value (kN)	Error (%)
Case 1	0.914	0.00	79.8	0.25	191.4	0.08	271.1	0.02
Case 2	4.420	0.00	79.7	0.33	191.4	0.10	271.1	0.03
Case 3	7.798	0.00	79.8	0.25	191.3	0.07	271.1	0.02
Case 4	4.597	4.02	81.7	2.11	185.6	2.92	267.3	1.44
Case 5	4.343	1.72	77.0	3.71	191.3	0.07	268.3	1.05
Case 6	7.798	0.00	68.2	14.7	185.8	2.81	254.0	6.33

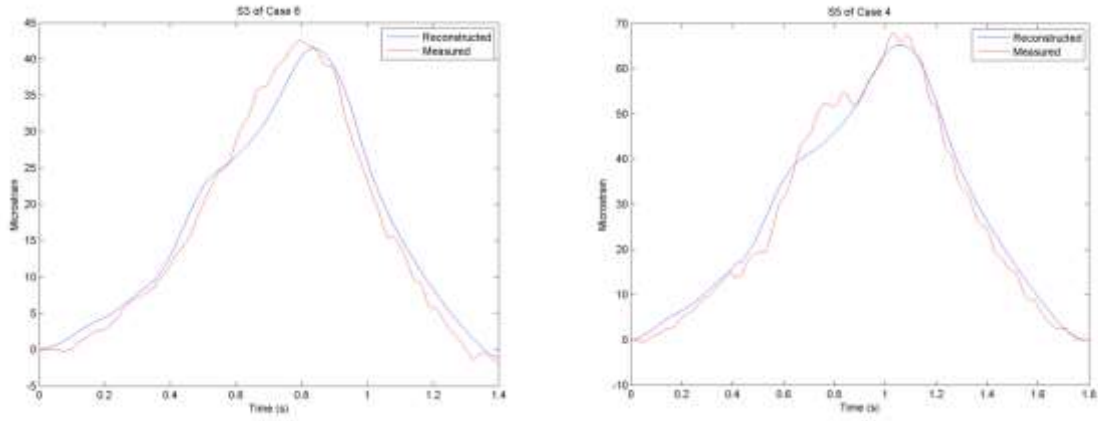


Figure 37
Comparison between the measured and reconstructed bridge responses of the weighing station:
(a) Case 4; (b) Case 6

CONCLUSIONS

A framework for assessing the conditions of in-service bridges was proposed. The framework uses the monitored live load effect (LE) data to achieve the assessment and the prediction of extreme traffic LEs is done using the Bayesian method which provides a systematic framework of uncertainty quantifications for extreme value analysis. The proposed assessment framework was then used to assess the current and future conditions of the I-10 Twin Span Bridge (TSB). The monitored strain responses were first processed using the wavelet decomposition to extract the traffic LEs and then the Bayesian method was adopted to predict the future maximum traffic LEs of the bridge. The design capacity envelopes and service LE envelopes of the I-10 TSB were developed based on the design calculation and the finite element (FE) models of the bridge.

Furthermore, a nothing-on-road (NOR) bridge weigh-in-motion (BWIM) system is developed. The developed NOR BWIM system is able to use only the strain measurements at the mid-span of the bridge to achieve the identification of the vehicle weight. Therefore, it provides a potential solution to achieve the live load monitoring using the current instrumentation of the I-10 TSB. Specifically, the developed BWIM algorithm first uses wavelet analysis to detect the vehicle's axles. Then, it uses the response sensitivity to identify the transverse position (TP) of the vehicle. Finally, with the identified vehicle's position on the bridge, the 2D Moses's algorithm is used to estimate the vehicle's axle weights.

Based on the study using the developed methodology, the following conclusions can be drawn:

- (1) The Bayesian method provides a systematic framework of uncertainty quantifications for extreme value analysis. Compared with the conventional method, the Bayesian method is able to quantify the uncertainties of parameters in terms of posterior distributions and incorporate the uncertainties into the prediction through the posterior predictive distribution;
- (2) The prediction results on the I-10 TSB show that the predicted maximum live LEs obtained using the Bayesian method are higher than those obtained using the conventional method especially for longer return periods. This difference is caused by the uncertainties inherent in the distribution parameters;
- (3) The condition assessment results on the I-10 TSB show that the bridge is performing normally under the current condition and that the bridge will be safe during its remaining

life from the design perspective except that certain girders close to the slow lane may be overstressed in the future (75-year return period);

- (4) Numerical results show that the proposed algorithm can identify the TP and the axle weights of vehicles and that considering the vehicle's TP can significantly improve the identification accuracy of axle weights. However, the identification accuracy of axle weights decreases significantly as the road surface condition becomes worse;
- (5) Vehicle axle identifications can be achieved through a wavelet analysis of bridge global responses. This approach has obvious advantages over existing axle identification methods in that it requires fewer sensors.

RECOMMENDATIONS

Based on the condition assessment results, the I-10 Twin Span Bridge is currently safe and performing as designed. Nevertheless, results also indicate that the exterior girders under the slow lane could be overstressed in the future. Thus, it is suggested that the future inspection pay special attention to these exterior girders. Furthermore, as the monitoring duration increases, the newly obtained data should be processed using the developed software and included to update the prediction in order to get more reliable predictions. In addition, when the monitoring period becomes sufficiently long, the non-stationarity of the traffic should be considered using the proposed method for long-term assessment in order to more accurately account for the traffic effects.

The project was intended to monitor the live load information. However, due to the failure of the installed WIM system, live load information cannot be achieved, which motivates the development of a nothing-on-road (NOR) bridge weigh-in-motion (BWIM) system in this study. Numerical simulation and experimental study on a bridge in Louisiana show that the developed NOR BWIM system is able to identify the vehicle speed, axle spacing and weight using only the strain sensors installed at the mid-span of the bridge. This suggests that the developed NOR BWIM system may provide a potential tool to achieve the live load monitoring of the I-10 Twin Span Bridge utilizing the current instrumentation. Nevertheless, the implementation of BWIM system requires field test to calibrate the influence surfaces. It is thus recommended that a load test be conducted to explore the feasibility of achieving the live load monitoring using the current instrumentation of the I-10 Twin Span Bridge. The load test can also provide information to calibrate the finite element model of the bridge, which can help further reduce the uncertainty and achieve more reliable condition assessment of the I-10 Twin Span Bridge.

ACRONYMS, ABBREVIATIONS, AND SYMBOLS

3D	Three-dimensional
AASHTO	American Association of State Highway and Transportation Officials
ANSYS	Commercial Finite Element Software
ASD	Allowable Stress Design
BWIM	Bridge weigh-in-motion
CDF	Cumulative distribution function
CDS	Composite distribution statistics
cm	centimeter(s)
CWT	Continuous wavelet transformation
DOF	Degrees of freedom
DOTD	Department of Transportation and Development
FAD	Free-of-axle-detector
FE	Finite Element
FT	Fourier transformation
FHWA	Federal Highway Administration
FT	Fourier transformation
GEV	Generalized extreme value
GVW	Gross vehicle weight
i.i.d.	Independent and identically
KDE	Kernel density estimation
lb.	pound(s)
LFD	Load Factor Design
LRFD	Load and Resistance Factor Design
LRFR	Resistant Factor Rating
LSU	Louisiana State University
LTRC	Louisiana Transportation Research Center
m	meter(s)
MCMC	Markov Chain Monte Carlo
MBE	Manual for Bridge Evaluation
MG	Metropolis-within-Gibbs
MLE	Maximum likelihood estimation
NBIP	National Bridge Inspection Program
NOR	Nothing-on-road
SHM	Structural health monitoring

SNR	Signal-to-noise ratio
STFT	Short-time Fourier analysis
TP	Transverse position
TSB	Twin Span Bridge
WIM	Weigh-in-motion

REFERENCES

1. AASHTO. LRFD design specification. (2012).
2. Abu-Farsakh, M., Yoon, S., Yu, X. and Tang, X. *Structural Health Monitoring of I-10 Twin Span Bridge*. (2014).
3. Fisher, R. A. and Tippett, L. Limiting forms of the frequency distribution of the largest or smallest member of a sample. *Mathematical Proceedings of the Cambridge Philosophical Society* 24, 180–190 (1928).
4. Renard, B., Sun, X. and Lang, M. in *Extremes in a Changing Climate: Detection, Analysis and Uncertainty* (Springer, 2012).
5. Rosenthal, J. in *Handbook of Markov Chain Monte Carlo* (CRC Press, 2011).
6. Ni, Y. Q. *et al.* In-Service Condition Assessment of Bridge Deck Using Long-Term Monitoring Data of Strain Response. *Journal of Bridge Engineering* 17, 876–885 (2012).
7. Gabor, D. Theory of communication. *Journal of the Institution of Electrical Engineers* 93, 429–457 (1946).
8. Moses, F. Weigh-in-motion system using instrumented bridges. *Transportation Engineering Journal of ASCE* 105, 233–249 (1979).
9. Deng, L., Yu, Y., Zou, Q. and Cai, C. S. State-of-the-Art Review of Dynamic Impact Factors of Highway Bridges. *Journal of Bridge Engineering* 20, 04014080 (2015).
10. Caprani, C. C., O'Brien, E. J. and Mclachlan, G. J. Characteristic traffic load effects from a mixture of loading events on short to medium span bridges. *Structural Safety* 30, 394–404 (2008).
11. Zhou, X. Statistical analysis of traffic loads and their effects on bridges. (Universite Paris-Est, 2013).
12. Deng, L. and Cai, C. S. Development of dynamic impact factor for performance evaluation of existing multi-girder concrete bridges. *Engineering Structures* 32, 21–31 (2010).
13. Chatterjee, P., OBrien, E., Li, Y. and González, A. Wavelet domain analysis for identification of vehicle axles from bridge measurements. *Computers and Structures* 84, 1792–1801 (2006).
14. International Organization for Standardization (ISO). *Mechanical vibration-road surface profiles—reporting of measured data*. (1995).
15. WAVE. *WEIGHING-IN-MOTION OF AXLES AND VEHICLES FOR EUROPE*

- (WAVE): *Report of Work Package 1.2. Work* (2001).
16. O'Brien, E. J., Rowley, C. W., González, A. and Green, M. F. A regularised solution to the bridge weigh-in-motion equations. *International Journal of Heavy Vehicle Systems* 16, 310–327 (2009).
 17. Yu, Y., Cai, C. S. and Deng, L. State-of-the-art review on bridge weigh-in-motion technology. *Advances in Structural Engineering* 19, 1514–1530 (2016).
 18. Shi, X., Cai, C. S. and Chen, S. Vehicle induced dynamic behavior of short-span slab bridges considering effect of approach slab condition. *Journal of Bridge Engineering* 13, 83–92 (2008).
 19. Berard, R. and Bourion, A. Truck widths and paths. in *International Symposium on Highway Geometric Design Practices* 1–9 (1998).
 20. Federal Highway Administration. *Federal Size Regulations for Commercial Motor Vehicles*. (2015).
 21. Chan, T. H. T. and O'Conner, C. Vehicle model for highway bridge impact. *Journal of Structural Engineering* 116, 1772–1793 (1990).
 22. Araujo, M. C. Slab-on-Girder Prestressed Concrete Bridges: Linear and Nonlinear Finite Element Analysis and Experimental Load Tests. (Louisiana State University, 2009).
 23. O'Brien, E. J., Quilligan, M. J. and Karoumi, R. Calculating an IL from direct measurements. *Proceedings of the Institution of Civil Engineers, Bridge Engineering* 159, 31–34 (2006). doi:10.1680/bren.2006.159.1.31
 24. Quilligan, M. Bridge Weigh-in-Motion: Development of a 2D Multi-vehicle algorithm. (Royal Institute of Technology, 2003).
 25. Jacob, B. and Beaumelle, V. F. La. Improving truck safety: Potential of weigh-in-motion technology. *IATSS Research* 34, 9–15 (2010).
 26. Richardson, J., Jones, S., Brown, A., O'Brien, E. and Hajializadeh, D. On the use of bridge weigh-in-motion for overweight truck enforcement. *International Journal of Heavy Vehicle Systems* 21, 83–104 (2014).
 27. Zhao, H., Uddin, N., Shao, X. D., Zhu, P. and Tan, C. J. Field-calibrated influence lines for improved axle weight identification with a bridge weigh-in-motion system. *STRUCTURE AND INFRASTRUCTURE ENGINEERING* 11, 721–743
 28. Yamaguchi, E., Kawamura, S., Matuso, K., Matsuki, Y. and Naito, Y. Bridge-Weigh-In-Motion by Two-Span Continuous Bridge with Skew and Heavy-Truck Flow in Fukuoka Area, Japan. *Advances in Structural Engineering* 12, 115–125 (2009).

29. Ieng, S.-S. Bridge Influence Line Estimation for Bridge Weigh-in-Motion System. *Journal of Computing in Civil Engineering* 29, 1–4 (2014).
30. Zhao, H., Uddin, N., O'Brien, E. J., Shao, X. and Zhu, P. Identification of Vehicular Axle Weights with a Bridge Weigh-in-Motion System Considering Transverse Distribution of Wheel Loads. *Journal of Bridge Engineering* 19, 04013008 (2014).
31. González, A., Dowling, J., O'Brien, E. J. and Žnidarič, A. Testing of a Bridge Weigh-in-Motion Algorithm Utilizing Multiple Longitudinal Sensor Locations. *Journal of Testing and Evaluation* 40, 133–150 (2012).
32. COST 323. *Weigh-in-motion of road vehicles*. (2002).
33. Lydon, M., Taylor, S. E., Robinson, D., Mufti, A. and O'Brien, E. J. Recent developments in bridge weigh in motion (B-WIM). *Journal of Civil Structural Health Monitoring* 6, 69–81 (2016).
34. Kalin, J., Žnidarič, A. and Lavrič, I. Practical Implementation of Nothing-on-the-Road Bridge Weigh-in-Motion System. *Slovenian National Building and Civil Engineering Institute* 207, 3–10 (2006).
35. Dunne, D., O'Brien, E. J., Basu, B. and González, A. Bridge WIM systems with nothing on the road (NOR). in *Proceedings of the 4th international WIM conference* 109–117 (2005).
36. Yu, Y., Cai, C. and Deng, L. Vehicle axle identification using wavelet analysis of bridge global responses. *Journal of Vibration and Control* (2015).
doi:10.1177/1077546315623147
37. Lechner, B., Lieschnegg, M., Mariani, O., Pircher, M. and Fuchs, A. A wavelet-based Bridge Weigh-in-Motion system. *International Journal on Smart Sensing and Intelligent Systems* 3, 573–591 (2010).
38. Wall, Christopher J Christenson, Richard E McDonnell, Anne-marie H Jamalipour, Alireza Sime, J. M. C. *A Non-Intrusive Bridge Weigh-in-Motion System for a Single Span Steel Girder Bridge Using Only Strain Measurements*. (2009).
39. O'Brien, E., Hajjalizadeh, D., Uddin, N., Robinson, D. and Opitz, R. Strategies for Axle Detection in Bridge Weigh-in-Motion Systems. in *Proceedings of the International Conference on Weigh-In-Motion (ICWIM 6)* 79–88 (Wiley, NJ, 2012).
40. Ojio, T., Carey, C. H., O'Brien, E. J., Doherty, C. and Taylor, S. E. Contactless Bridge Weigh-in-Motion. *Journal of Bridge Engineering* 21, 1–11 (2016).
41. Brown, A. Bridge weigh-in-motion deployment opportunities in Alabama. (2011).

42. Haugen, T., Levy, J. R., Aakre, E. and Tello, M. E. P. Weigh-in-Motion Equipment - Experiences and Challenges. *Transportation Research Procedia* 14, 1423–1432 (2016).
43. Hang, W., Xie, Y. and He, J. Practices of using weigh-in-motion technology for truck weight regulation in China. *Transport Policy* 30, 143–152 (2013).
44. Karim, M. R., Ibrahim, N. I., Saifizul, A. A. and Yamanaka, H. Effectiveness of vehicle weight enforcement in a developing country using weigh-in-motion sorting system considering vehicle by-pass and enforcement capability. *IATSS Research* 37, 124–129 (2014).
45. Han, L. D., Ko, S. S., Gu, Z. and Jeong, M. K. Adaptive weigh-in-motion algorithms for truck weight enforcement. *Transportation Research Part C: Emerging Technologies* 24, 256–269 (2012).
46. Rytter, A. *Vibrational Based Inspection of Civil Engineering Structures*. (University of Aalborg, 1993).
47. Carden, P. and Fanning, P. Vibration Based Condition Monitoring: A Review. *Structural Health Monitoring* 3, 355–377 (2004).
48. Adams, R. D., Cawley, P., Pye, C. J. and Stone, B. J. A Vibration Technique for Non-Destructively Assessing the Integrity of Structures. *Journal of Mechanical Engineering Science* 20, 93–100 (1978).
49. Cawley, P. and Adams, R. D. The location of defects in structures from measurements of natural frequencies. *The Journal of Strain Analysis for Engineering Design* 14, 49–57 (1979).
50. Kong, X. **FRAMEWORK OF DAMAGE DETECTION IN VEHICLE-BRIDGE COUPLED SYSTEM AND APPLICATION TO BRIDGE SCOUR MONITORING**. (Louisiana State University, 2013).
51. Law, S. S. *et al.* Dynamic Assessment of Bridge Load-Carrying Capacities. I. *Journal of Structural Engineering* 121, 478–487 (1995).
52. Fan, W. and Qiao, P. Vibration-based Damage Identification Methods: A Review and Comparative Study. *Structural Health Monitoring* 10, 83–111 (2010).
53. Ewins, D. J. *Modal Testing: Theory and Practice*. (Research Studies Press Ltd, 1984).
54. Gandomi, A. H., Sahab, M. G., Rahaei, A. and Gorji, M. S. Development in mode shape-based structural fault identification technique. *World Applied Sciences* 5, 29–38 (2008).
55. Allemang, R. J. and Brown, D. L. Correlation coefficient for modal vector analysis. in *Proceedings, 1st International Modal Analysis Conference* 110–116 (1982).

56. Lieven, N. A. J. and Ewins, D. J. Spatial correlation of mode spaces: the coordinate modal assurance criterion (COMAC). in *Proceedings of the 6th International Modal Analysis Conference* 1063–1070 (1988).
57. Shi, Z. Y., Law, S. S. and Zhang, L. M. Damage Localization by Directly Using Incomplete Mode Shapes. *Journal of Engineering Mechanics* 126, 656–660 (2000).
58. Pandey, A. K., Biswas, M. and Samman, M. M. Damage detection from changes in curvature mode shapes. *Journal of Sound and Vibration* 145, 321–332 (1991).
59. WAHAB, M. M. and DE ROECK, G. Damage Detection in Bridges Using Modal Curvatures: Application To a Real Damage Scenario. *Journal of Sound and Vibration* 226, 217–235 (1999).
60. Byung Hwan Oh, B. S. J. Structural Damage Assessment with Combined Data of Static and Modal Tests. *Journal of Structural Engineering* 124, 956–965 (1998).
61. Mottershead, J. E. and Friswell, M. I. Model Updating In Structural Dynamics: A Survey. *Journal of Sound and Vibration* 167, 347–375 (1993).
62. Kim, G.-H. and Park, Y.-S. An improved updating parameter selection method and finite element model update using multiobjective optimisation technique. *Mechanical Systems and Signal Processing* 18, 59–78 (2004).
63. Fritzen, C. P. in *Structural Health Monitoring* (ed. Balageas, D.) 45–224 (ISTE Ltd, 2010). doi:10.1002/9780470612071.ch2
64. Cantero, D. and González, A. Bridge Damage Detection Using Weigh-in-Motion Technology. *Journal of Bridge Engineering* 1–10 (2014). doi:10.1061/(ASCE)BE.1943-5592.0000674.
65. Cantero, D., Karoumi, R. and González, A. The Virtual Axle concept for detection of localised damage using Bridge Weigh-in-Motion data. *Engineering Structures* 89, 26–36 (2015).
66. Carey, C. H., O’Brien, E. J. and Keenahan, J. Investigating the Use of Moving Force Identification Theory in Bridge Damage Detection. *Key Engineering Materials* 569–570, 215–222 (2013).
67. Gonzalez, I. and Karoumi, R. BWIM aided damage detection in bridges using machine learning. *Journal of Civil Structural Health Monitoring* 5, 715–725 (2015).
68. AASHTO. LRFR rating specification. (2010).
69. Zhao, H. *et al.* Use of weigh-in-motion (WIM) data for site-specific LRFR bridge rating. in *6th International Conference on Weigh-in-Motion, ICWIM6* (2012).

70. Pelphrey, J. *et al.* State-Specific LRFR Live Load Factors Using Weigh-in-Motion Data. *Journal of Bridge Engineering* 13, 339–350 (2008).

APPENDIX I

Review on Bridge Weigh-in-motion Technology

Overloaded trucks pose serious threats to the safety of the public and transportation systems. Vehicle overloading causes accelerated degradation of highway infrastructures [25]. For highway bridges, overloaded trucks lead to fatigue damages or even cause the collapse of bridges in some extreme cases. Moreover, overloaded vehicles are more likely to cause traffic accidents that usually lead to severe casualties. For these reasons, vehicle overweight enforcement is critical to the protection of the safety of the public and highway infrastructures. The traditional method of enforcement is to use static scales to weigh highway trucks (Figure 38). However, this interrupts the traffic and decreases the efficiency of the transportation system. In order to overcome these limitations, weigh-in-motion technology has been developed to measure the weight of vehicles while they are in motion. WIM technology provides an efficient method for overweight enforcement [26]. Furthermore, WIM can also be used to implement toll-by-weight method and collect traffic information for traffic planning and design.

Generally speaking, WIM can be classified into two types including the pavement-based WIM and bridge BWIM (BWIM). The pavement-based WIM uses devices installed on the road surface such as bending plates, piezoelectric sensors to directly measure the axle force of the vehicle when the vehicle axle contacts the device [26]. The technology adopted by pavement-based WIM systems is relatively simple. However, since the device of pavement-based WIM systems is installed on the road surface, it is intrusive to the pavement and has poor durability due to the direct exposure to the heavy traffic. Thus, its installation and maintenance usually requires traffic closures. Furthermore, the axle force measured by the pavement-based WIM is not the static weight of the axle since the axle force is a time-varying force. Therefore, the errors of estimated vehicle weight could be significant especially when the dynamic effect is pronounced [17].



Figure 38
Weigh stations on the highway

The concept of BWIM was first proposed by Moses in 1979 [8]. BWIM uses an instrumented bridge as the weighing scale to estimate the vehicle weight using the measured responses of bridges. The BWIM has many advantages over the pavement-based WIM. Firstly, the BWIM uses sensors installed underneath the bridge. Thus, the BWIM has better durability and its installation does not interrupt the traffic. Furthermore, the measurement period of BWIM is usually significantly longer, which allows the dynamic effect to be filtered out and the static weight of the vehicle to be obtained. In addition, the BWIM also has the advantages of being non-intrusive and portable, making it an ideal replacement for pavement-based WIM. Figure 39 shows the framework of BWIM. In addition to the traditional application to overweight enforcement, recent studies have explored its potential application in fields such as SHM and bridge condition assessment.

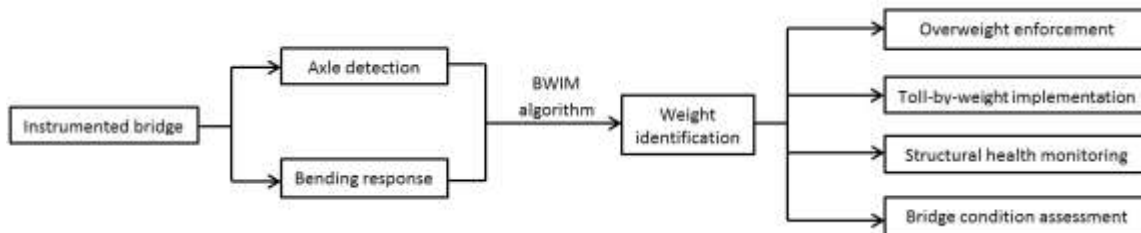


Figure 39
The framework of BWIM and its applications

This paper presents a comprehensive review of BWIM technology and its applications. The identification methodology is first reviewed and the instrumentation of the BWIM system is introduced focusing on its portability of application. Then, the applications of BWIM are discussed including the overweight enforcement, toll-by-weight, structural health monitoring and bridge condition assessment. Meanwhile, much effort is made to identify the remaining issues in the application of BWIM technology and the corresponding future research is proposed.

BWIM Algorithm

Different methods have been proposed to identify the vehicle weight in BWIM including the Moses's algorithm, the influence area method, the reaction force method, and move force identification (MFI) method. Among these algorithms, the Moses's algorithm is commonly adopted for modern commercial BWIM systems due to its easy implementation and acceptable accuracy.

Moses's Algorithm. Moses proposed the first BWIM algorithm for a beam-slab bridge [8]. For this type of bridge, the measured bending moment at time step k can be obtained by summing the individual bending moment of each girder:

$$M_k^m = \sum_i^G ES_i \varepsilon_i \quad (48)$$

where, G is the total number of girders; E is the modulus of elasticity; S_i is the section modulus of the i th girder; ε_i is the measured strain in the i th girder. Meanwhile, the predicted bending moment at time step k can be obtained using the influence line concept as:

$$M_k^p = \sum_{i=1}^N A_i I_{i,(k-C_i)} \quad (49)$$

$$C_i = \frac{D_i f}{v} \quad (50)$$

where, N is the number of axles; A_i is the weight of the i th axle; $I_{i,(k-C_i)}$ is the influence ordinate at the position of the i th axle; D_i is the distance between the first axle and i th axle; C_i is the number of scans corresponding to D_i ; f is the sampling frequency of the BWIM system; v is the vehicle speed which is assumed to be a constant as the vehicle travels on the bridge. The error function for the total number of step T is defined as:

$$E = \sum_{k=1}^T (M_k^p - M_k^m)^2 \quad (51)$$

To minimize the error function, the least-square method is used. The partial derivative with respect to the axle weight is set to zero:

$$\frac{\partial E}{\partial A_j} = 2 \sum_{k=1}^T (M_k^p - M_k^m) \frac{\partial (M_k^p - M_k^m)}{\partial A_j} = 0 \quad (52)$$

which leads to the following equation upon rearrangement and substitution:

$$\sum_{k=1}^T \sum_{i=1}^N A_i I_{i,(k-C_i)} I_{j,(k-C_j)} = \sum_{k=1}^T M_k^m I_{j,(k-C_j)} \quad (53)$$

Define:

$$F = [F_{ij}] = \sum_{k=1}^T I_{i,(k-C_i)} I_{j,(k-C_j)} \quad (54)$$

$$M = [M_j] = \sum_{k=1}^T M_k^m I_{j,(k-C_j)} \quad (55)$$

equation (53) can then be written in a matrix form as:

$$FA = M \quad (56)$$

Thus, the axle weight and gross vehicle weight (GVW) can be calculated as:

$$A = F^{-1}M \quad (57)$$

$$GVW = \sum_{i=1}^N A_i \quad (58)$$

Calibration of BWIM Systems. For the Moses's algorithm, the accuracy of the influence line is critical for the BWIM system to achieve an accurate identification. When Moses first proposed the BWIM concept, the theoretical influence line of a simply-supported beam was adopted [8]. However, the theoretical influence line cannot accurately predict the real behavior of the bridge. To reduce the errors caused by the difference between the theoretical and true influence lines, O'Brien et al. presented a method to generate the influence line from direct measurements [23]. By using the least-square method, the error function defined in equation (51) is minimized with respect to the influence ordinate while the axle weights of the calibration vehicle are already known and thus the measured response of a load effect is converted into the influence line of that effect. This method was verified by field tests and was successfully applied in a BWIM system by Zhao et al. [27]. However, it should be mentioned that this method generates the influence line by connecting discrete points instead of producing a smooth curve. In order to generate a continuous influence line, some researchers adopted a polynomial function to describe the influence line and the optimal coefficients of the polynomial function are determined by minimizing the error function [28]. Ieng pointed out that the method proposed by O'Brien et al. is sensitive to perturbations and revised the method on a probabilistic basis utilizing the maximum likelihood estimation principle, respectively [23, 29]. The revised method takes advantage of more signals in the estimation of the influence line and thus reduces the error caused by the noise in a specific signal.

Accuracy of the Moses's Algorithm. The accuracy of the Moses's algorithm is affected by several factors. The three most significant factors include the dynamic effect of moving vehicles, the transverse position of the vehicle, and the condition of the final system equations. First of all, the dynamic effect caused by the moving vehicles reduces the accuracy of the Moses's algorithm. This is because the Moses's algorithm determines the axle weights through minimizing the difference between the measured and predicted bridge responses. However, the dynamic effect causes the measured response to deviate from the predicted response obtained using the static influence line and thus reduces the accuracy of the identified axle weights. From this perspective, the Moses's algorithm usually requires the bridge surface and approach span be in good condition if a satisfactory accuracy is to be achieved. Furthermore, the transverse position of the vehicle may also affect the accuracy of the Moses's algorithm. While the transverse position of the vehicle is not considered in the original Moses's algorithm, some researchers have found that ignoring the transverse position of the vehicle could lead to significant errors in the identified axle weights in some cases [30]. In practice, the errors can be reduced by choosing bridges with fewer lanes. However, even if the bridge has only one lane, which is a rare case, the transverse position of the vehicle within the lane will still have an influence on the accuracy. Also, another issue associated with bridges having more than one lane is that there might be multiple vehicles present on the bridge, which makes the identification of individual axle weight difficult. Accordingly, some researchers proposed two-dimensional (2D) BWIM algorithms on the basis of the Moses's algorithm to address this issue. Quilligan proposed a 2D BWIM algorithm as an extension to the Moses's algorithm [24]. In the 2D algorithm, the influence surface concept is used instead of the influence line. The influence surface represents the load effect caused by a unit concentrated load at position (x,y) and the axle weights can be found by following the same minimization routine as used in the Moses's algorithm. Theoretically, this would be an ideal solution to account for the effect of the transverse position of vehicles. However, the disadvantage of this algorithm is that it requires an accurate finite-element (FE) model of the bridge which comes at the cost of complex calculations as well as time-consuming calibrations. Alternatively, some researchers proposed other methods that modified the original Moses's algorithm without involving the use of influence surface. Zhao et al. proposed a modified 2D Moses's algorithm [30]. The proposed algorithm considered the 2D behavior of the bridge by incorporating the transverse distribution of wheel loads on different girders to predict the responses.

Another common problem encountered when implementing the Moses's algorithm is that the derived system equations are usually ill-conditioned, especially for a rough surface profile and vehicles with closely-spaced axles [16]. In this case, the solution of the axle weights using the least-square method would be sensitive to the measurement noise. This problem

can be resolved by applying the Tikhonov regularization technique to provide bounds to the solution. An additional penalty term multiplied by a regularization parameter is added into the original minimization formulation to improve the condition of the original system. The regularization technique was reported to significantly improve the accuracy of the identified axle weights; however, as the vehicle dynamics becomes more noticeable, the convergence of the regularized solution becomes slower [16]. Gonzalez et al. proposed a novel BWIM algorithm which makes use of strain sensors at multiple longitudinal locations [31]. This algorithm allows the ill-conditioned portions of the predicted axle force history to be identified and removed before calculating the static axle weights.

The accuracy of a WIM system is usually defined in a statistical way. COST classified the accuracy into different levels as A, B, C and D based on the tolerance of the confidence interval for the relative error of the vehicle weight [32]. The level of accuracy determines the purposes of the BWIM [32]: (the number in the parenthesis represents the width of the confidence interval):

Class A (5): legal purposes such as enforcement of legal weight limits and other particular needs.

Class B+ (7): enforcement of legal weight limits in particular cases with a special agreement of the legal authorities; efficient pre-selection of overloaded axles or vehicles.

Class B (10): pavement and bridge design, maintenance or evaluation, such as aggressiveness evaluation, fatigue damage and lifetime calculations; pre-selection of overloaded axles or vehicles.

Class C (15) or D+(20): Detailed statistical studies, determination of load histograms, and accurate classification of vehicles based on the loads; infrastructures studies and fatigue assessments.

Class D (25): Weight indications required for statistical purposes, economical and technical studies, standard classification for vehicles according to wide weight classes.

Instrumentation of BWIM Systems

An on-site BWIM system usually consists of a data acquisition system, communication system, power supply system, and sensors. As an example, Figure 40 shows the components of the SiWIM system, a commercially available BWIM system that was originally developed within the framework of the WAVE project and has been continuously improved and updated over the years [15]. The data collected from the on-site system are processed with

software using BWIM algorithms. The results are then presented in a graphic user interface (GUI) that is designed for users to visualize the real-time monitoring data. The following sections will introduce the typical instrumentation of BWIM systems including the types of sensors used in a BWIM system and their installation locations.



Figure 40

Components of an SiWIM system: (1) FAD sensors, (2) spider, (3) weighing sensors, (4) cabinet and panel, (5) batteries, (6) solar panels, (7) solar panel installation, (8) antenna, (9) camera, (10) PDA [30]

Axle Detection. In a modern BWIM system, axle-detecting sensors are used to identify the presence of vehicle axles from which the speed and axle spacing of the vehicle can be calculated. Axle detection is an indispensable part of the BWIM system since the identified vehicle speed and axle spacing of the vehicle will directly affect the results of the axle weight calculation. The traditional instruments for axle detection include tape switches and pneumatic tubes. Moses pointed out that traffic switches are easier to incorporate into the system while the pneumatic tubes require a pressure sensing device to produce the signal of axle passage [8]. The identification of vehicle speed and axle spacing using traditional axle

detectors is actually quite simple. Usually, two parallel axle detectors are placed on the road surface where the spacing between the two detectors is measured as an input to the system. In some cases, where the transverse location of the vehicle needs to be determined, a third detector is placed diagonally with a known angle corresponding to the other two detectors. Nevertheless, the installation of axle detectors on the pavement usually requires lane closure and the poor durability of sensors also diminishes the advantage of the BWIM systems over the pavement-based WIM systems.

To overcome the problems of the traditional axle detection, the FAD algorithm was first proposed in the WAVE project [15]. The basic idea of the FAD algorithm is to use FAD sensors to replace traditional axle detectors on the road surface. The FAD sensors measure the local strain responses and thus they pick up a sharp peak upon each axle passage above the sensor location. Typically, two FAD sensors are installed at different longitudinal locations on each lane with a known distance. Figure 41 shows some typical signals of FAD sensors. The signals were recorded under a five-axle truck passing on the bridge [30]. It can be seen that each FAD sensor picked up five peaks corresponding to the five axles. However, it should be mentioned that clear peaks in the strain signal may not occur if the wheel load is directly applied over the beam [33]. In practice, a correlation function is usually used to calculate the vehicle speed. The correlation function is defined as:

$$Corr(t) = \int_{-\infty}^{+\infty} f(\tau)g(t+\tau)d\tau \quad (59)$$

where, $f(t)$ and $g(t)$ are the signals of FAD sensors at two longitudinal locations, respectively. To calculate the vehicle speed, the time taken by the vehicle to pass the known distance between the two sensors is needed. From equation (59), it can be seen that the correlation function will obtain the maximum value when $f(t)$ and $g(t+\tau)$ both reach the maxima, i.e., picking up the peak corresponding to the same vehicle axle. Since the time difference between $f(\tau)$ and $g(t+\tau)$ is t , the time difference t_0 that gives the maximum value of the correlation function is the time taken by the same vehicle axle to pass the known distance between the two FAD sensors and then the vehicle speed can be easily calculated by using the known distance and the time difference t_0 . Once the vehicle speed is known, the axle spacing can be obtained by using the time difference between the peaks in the FAD signals [34].

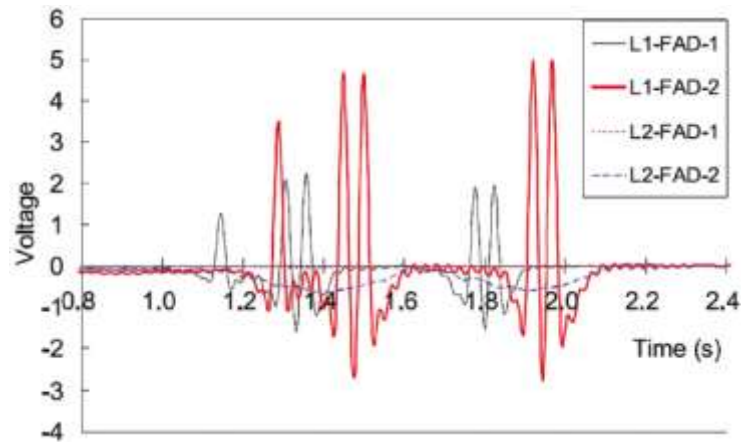


Figure 41
Typical FAD signals of a five-axle truck crossing [30]

Although the FAD algorithm resolves the durability problem of the traditional axle detectors, it still requires additional sensors, i.e., FAD sensors, only for the purpose of axle detection. Furthermore, the FAD algorithm imposes certain restrictions upon the span length and superstructure thickness of the selected bridge. Namely, the FAD algorithm is not applicable to all types of bridges. As a general rule of thumb, the bridges suitable for the FAD algorithm should have the following: (1) a short span or relatively longer span but with transverse supports, i.e., secondary members such as transverse cross-beams or stiffeners, to divide the bridge into sub-spans because longer spans will have joint contributions of several axles that make it difficult to distinguish individual axles; (2) a thin superstructure because a thick superstructure will “smear” the peaks induced by the vehicle axles; (3) a smooth road surface and approach span since a rough surface condition will cause significant dynamic effects which impose additional peaks into the signal [15, 34]. The types of bridges that have already been identified as suitable for the FAD algorithm include orthotropic deck bridges, short integral bridges with thin slabs (usually 6 to 12 meters long with the slab thickness between 40 to 60 centimeters), and beam-slab bridges with secondary members [34].

Recently, the concept of a nothing-on-road (NOR) BWIM system was proposed. The goal of the NOR BWIM system is to free the use of axle detector on the road surface. While the FAD algorithm is one application of the NOR BWIM, a more effective way is to directly employ the global strain signal obtained from the weighing sensors to identify the vehicle speed and axle spacing. This will be a very attractive feature for future commercial BWIM systems since it reduces the number of sensors to be installed and thus the cost of the system, making the installation even easier. Besides, it does not impose any restriction on the selection of bridges, which helps extend the application of BWIM techniques. However, direct identification from the global strain signal is very difficult since it usually does not have a sharp peak upon each axle passage. Nevertheless, it has been shown by some

researchers that the identification can be achieved through proper signal processing techniques such as a wavelet-based analysis, which are suitable to treat non-stationary signals. Dunne et al. first proposed using wavelet transformation to identify closely-spaced axles from FAD signals [35]. Chatterjee et al. conducted field testing on a culvert and adopted the wavelet transformation to analyze the strain signal obtained from vehicle crossing [13]. The results show that wavelet techniques can help identify closely-spaced axles within a tandem or tridem group which could not be directly identified from the FAD signal and reveal the potential of using wavelet techniques to identify vehicle axles from the strain signal of weighing sensors. Yu et al. proposed a vehicle axle identification method based on the wavelet transformation of the global signal [36]. The numerical results showed that this method can provide accurate identification of vehicle axles using only weighing sensors.

In addition, some other methods for axle detections have also been reported. Some researchers found that crack openings on the bottom of the concrete slabs are sensitive to axle loads and thus they measured the crack displacements to detect the vehicle axles [37]. However, this method cannot be generalized since it is only applicable to bridges with crack openings. Wall et al. adopted an approach where the change of slope induced by the axle passage is used for the axle identification [38]. In an ideal setting, the passage of each axle will have a corresponding impulse in the second derivative of the strain signal. However, in practice, this approach requires that the strain signal have evident slope discontinuities; in other words, the strain signal must show a certain level of sensitivity to the vehicle axles. Also, as these slope discontinuities are only subtle changes, this approach may no longer be feasible once the measurement noise is introduced in practice. O'Brien et al. proposed a novel axle detection strategy using shear strain sensors based on the assumption that each axle passage will induce a sudden change of the shear strain [39]. Preliminary FE analyses have been carried out on a beam-slab bridge and the interface of the web and the flange is recommended for the sensor location. Further work will be continued to assess the feasibility of this novel axle detection method. With the recent advances of image processing technology, the identification of the vehicle axle configuration has been made possible through proper image analysis algorithms and thus a vision-based system utilizing a roadside camera was proposed by some researchers as a potential tool for the axle detection [40].

Installation Location of Sensors

The installation location of sensors should account for several factors including the purpose of sensors, types of bridges, strain levels, sensitivity to strain variations, etc. In this section, the installation location of sensors will be discussed with respect to the two most important

factors, i.e., the purpose of sensors and types of bridges chosen for installation. In addition, a case study with specific sensor layouts on a typical beam-slab bridge is also presented.

Purpose of Sensors. Weighing sensors measure the global bending strain caused by vehicle loads and thus they are usually installed at locations of most pronounced responses, e.g., the mid-span of the bridge. For complex bridge structures, the locations of weighing sensors can be determined by a preliminary FE analysis. As for axle-detecting sensors, both traditional axle detection and FAD algorithm require two parallel lines of sensors be installed with a known distance. However, the differences are the following: (1) traditional axle-detecting sensors are installed on the road surface while FAD sensors are installed underneath the bridge; (2) traditional axle-detecting sensors can be installed at almost any location on the bridge; however, the selection of the installation locations for FAD sensors depends on the shape of the influence line since the influence line at the location of installation needs to present a sharp peak in order for the axle identification.

Type of Bridges. The sensitivity of strain responses to axle loads differs between different bridge types and different measurement locations on a certain bridge, thus the specific plan of sensor layouts for each bridge should be determined on a case-by-case basis. Nevertheless, based on the existing BWIM practices, the general schemes of sensor layouts for some typical bridges are summarized and shown in Table 20. It should be mentioned that the reason for requiring only one line of axle-detecting sensors in orthotropic deck bridges is that the installed weighing sensors also pick up sharp peaks corresponding to the axle passage, namely, the weighing sensors in this case also serve the purpose of axle detection.

In addition, Brown studied the influence of different installation schemes of FAD sensors on the accuracy of axle detections including the longitudinal and transverse locations, and installation angles [41]. Based on the signals obtained from a T-beam reinforced concrete bridge, it was concluded that FAD sensors should be orientated longitudinally and installed close to the beginning or end of the bridge span, ideally directly below the wheel path, in order to obtain a clear signal with sharp peaks. The reason for choosing the beginning or end of the bridge span is that the bridge is stiffer at these locations and thus more definite peaks can be produced, and that the dynamic effects at these stiffer locations are also less pronounced, which leads to a cleaner signal. Furthermore, the study also shows that, compared to longitudinally-orientated sensors, transversely-orientated sensors provide poor signals for axle detection. Besides, it was also found that weighing sensors do not have to be installed exactly at the mid-span since any location near the mid-span can provide an adequate strain level for weighing purposes.

Table 20
General layout schemes of BWIM sensors for typical bridges types

Type of bridges	Location of weighing sensors		Location of axle-detecting sensors	
	Longitudinal	Transverse	Longitudinal	Transverse
Orthotropic deck bridges		Bottom of the longitudinal stiffener	One line of sensors at a section away from the mid-span	Bottom of the longitudinal stiffener
Integral slab bridges	Mid-span	Bottom of the slab	Two lines of sensors at two sections away from the mid-span	Bottom of the slab
Beam-slab bridges		Bottom of the girder		Bottom of the slab

Case Study

In order to give a better illustration on the sensor installation of the BWIM system, a case study is presented herein. The case study is chosen from a recent BWIM practice conducted in Alabama [30]. The instrumented bridge is a three-span simply-supported concrete multi-girder bridge. The three spans have an equal length of 12.8 m and the first span was chosen for the installation of the BWIM system. The reasons for selecting this bridge are as follows: (1) the bridge has a short span and thin superstructure, suggesting that it is suitable for the implementation of the FAD algorithm; (2) the short span has higher natural frequencies to avoid matching the natural and pseudo frequencies of the vehicle and thus reduces the dynamic effect of the moving vehicles; (3) the bridge has a smooth approach and good surface condition, which again helps minimize the dynamic effect.

For the sensor installations, a total of four weighing sensors were installed in a parallel manner underneath the girders (one for each girder) and a total of four FAD sensors were mounted beneath the concrete slab (two for each lane). The specific sensor layouts are presented in Figure 42. It should be noted that the sensors are not installed exactly at the mid-span because of the diaphragm.

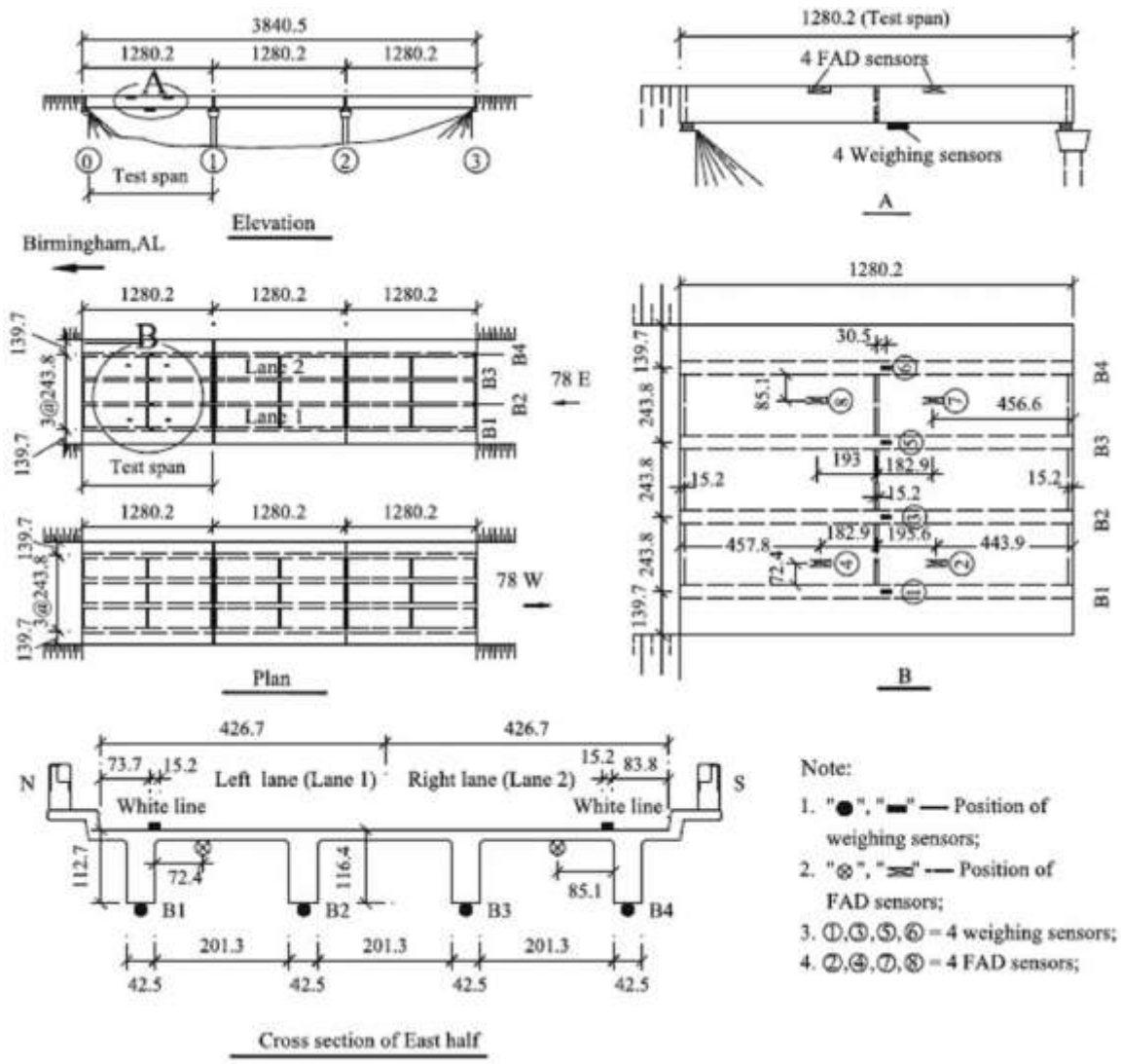


Figure 42
Sensor layouts of a typical BWIM system (cm) [30]

Applications of BWIM Technology

Overweight Enforcement. The traditional method for overweight enforcement uses static scales aided with visual pre-selection to weigh highway trucks. However, the use of static scales is time-consuming and infeasible for transportation systems with heavy truck traffic [42]. The WIM technology is able to identify the truck weight without interrupting the traffic, which makes it an ideal tool for overweight enforcement. Nevertheless, the use for direct enforcement requires very accurate estimation of vehicle weight. As a prerequisite of direct enforcement, the error of the identified vehicle weight should be less than 5% for 95% of the results [33]. For pavement-based WIM, the accuracy is affected by many factors including the quality of system installation, usage and maintenance, vehicle speed and acceleration, road surface condition, tire friction and weather conditions, which makes it difficult to satisfy the requirement for direct enforcement [43]. Instead, pavement-based WIM can be used for effective pre-selection of overloaded trucks [44]. As shown in Figure 43, the truck is first weighed on the highway as it vehicles travels at its normal speed. The estimated weight of truck is then compared with a preset threshold determined based on the distribution of the measured vehicle weight [45]. If the estimated weight exceeds the threshold, then the truck may be overloaded and needs to bypass the inspection station to be weighed by the static scale. Otherwise, the truck can proceed without inspection.

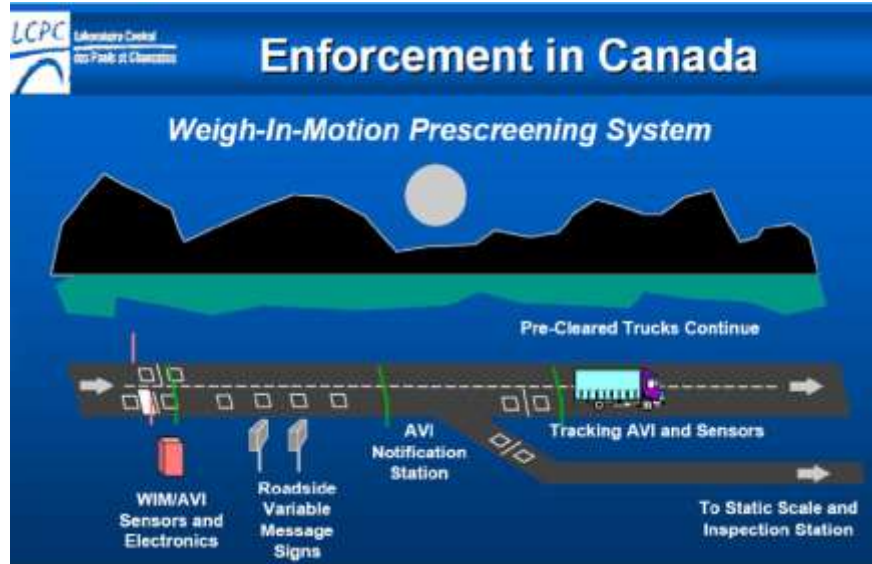


Figure 43
Pre-selection of overloaded trucks using pavement-based WIM [25]

The BWIM is potentially more accurate than the pavement-WIM since it has longer measurement period. The BWIM can be used for direct enforcement provided that the selected bridge meets certain requirements such as a relatively short span and good surface condition. In addition, another advantage of BWIM for overweight enforcement is that it is

invisible to truck drivers. In practice, BWIM has been commonly used for pre-selection of overloaded vehicles. However, the application for direct enforcement is still rare.

Toll-by-weight. In some countries such as China, the toll rate is calculated based on the truck weight and thus the accurate estimation of truck weight is critical to the implementation of the toll-by-method method [43]. In this case, static weighing is clearly not suitable considering the large volume of trucks that need weighing. Instead, pavement-based WIM has been used as the primary method for the toll-by-weight method. Figure 44 shows the setup of a WIM-based toll booth. Typically, bending plate or piezoelectric cable WIM scales are used due to the low costs. However, their accuracy is relatively low. Sometimes, multiple weighing is needed, leading to congestions at the toll station. BWIM, on the other hand, is potentially more suitable for the toll-by-weight method since it is more accurate than pavement-based WIM. However, it does require a bridge suitable for BWIM implementation, which, to some degree, limits the application of BWIM for the implementation of the toll-by-weight method.

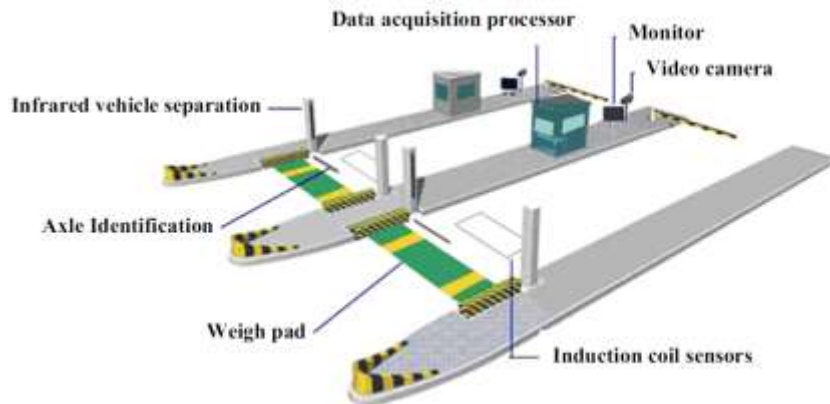


Figure 44
A typical WIM-based toll booth [43]

In addition to the above two applications, the BWIM can also be used to simply monitor the traffic. The obtained traffic data can be used for traffic planning and the design of pavement and bridges, which does not necessarily require very high accuracy of the system [32].

Structural Health Monitoring (SHM). The objective of SHM is to determine the health condition of the bridge. The damage of the structure can happen due to natural causes such as the deterioration of material, corrosion, fatigue cracking or due to human factors such as vehicle and vessel impact. The damage due to natural causes is usually progressive while the damage due to human factors is usually sudden. The SHM uses the monitored bridge response to detect the sudden or progressive damage to the structure. Generally, the SHM methods are classified into the four levels [46]:

Level 1: identify the presence of the damage.

Level 2: identify the presence and location of the damage.

Level 3: identify the damage presence and location, and quantify of the level of damage.

Level 4: identify the damage presence and location, quantify of the level of damage, and predict of the remaining life of structures.

When structural damage occurs, the structural properties also change correspondingly. Therefore, the core of SHM is to find a damage index that is sensitive to the changes in structural properties. To do this, numerous damage detection methods have been developed. Generally speaking, the damage detection methods can be classified into two types: response-based method and model-based method.

Response-based Methods

Natural frequency-based Methods. The natural frequency of structures is sensitive to structural damages since it is related to the stiffness and mass of the structure. The shift of natural frequency may indicate the presence of structural damage. Also, the natural frequency of the structures can be easily measured. Thus, the change of natural frequencies is an attractive damage index to indicate the presence of structure damage [47]. Furthermore, it was shown that the ratio of the change of frequency in two modes is a function of the damage location and thus the measurement of a pair of frequencies yield a locus of potential damage locations [48, 49]. To identify the location of the damage, the loci of different pairs of modes are superimposed and the damage location can be identified as the intersection of the curves [49]. However, there are many limitations to natural frequency-based methods. For example, it is not sensitive to local damages [50]. Some researchers have found that the shift of natural frequency was not significant even though significant loss of stiffness had occurred in real structures [51]. Moreover, it was reported that the variation of natural frequency due to ambient vibrations and environmental effects could reach 10%, which makes it difficult to distinguish the cause of the change in the natural frequency [47]. For these reasons, the greatest success of using natural frequency-based methods for damage detection is still in laboratory tests using simple structures with single damage locations [52].

Mode shape-based Methods. Different methods have been developed to extract the mode shapes from the measured bridge responses [53]. The mode shape-based methods are based on the assumption that the mode shapes of the structure changes as a result of structural damage. Thus, the damage can be detected by comparing the mode shapes of the intact and damaged structures [54]. Two indices have been developed to measure the

similarity of mode shapes including the MAC (modal assurance criterion) and the COMAC (the coordinate modal assurance criterion) [55, 56]. The MAC measures the overall similarity of mode shapes. The value of MAC varies from 0 to 1 with 0 being entirely dissimilar and 1 being perfect match [47]. A reduction of the MAC indicates the presence of damage. The COMAC is the measure of similarity of mode shapes at a point. A low value of COMAC at a point indicates the difference of the mode shapes at the point and can thus provide information on the potential damage locations [52]. The mode shape-based methods are more sensitive to local damages than the frequency-based methods since the mode shapes contain the location information. Nevertheless, the mode shape-based methods depend on the accurate measurement of mode shapes [47]. The main difficulties lie in a large number of sensors required [52], sensitivity to measurement noise [50], and the expansion techniques to obtain the mode shapes from incomplete measurements [57].

In addition to the direct comparison of mode shapes, the change of mode shape curvature is considered to be sensitive the location of the damage and it is usually more pronounced than the change of displacement of mode shapes [58-59]. The curvature can be calculated using the displacement of the mode shapes. The method based on the change of mode shape curvature has been shown to be effective in detecting local damages [60]. However, at higher modes, the difference in mode shape curvatures may not be caused by structural damages [50]. Usually, only the first few modes are used to extract the curvatures for damage detection. Besides, the mode shape curvature is the derivative of mode shape displacement and thus it relies even more on the accurate measurement of mode shapes [47].

Model-based Methods. Model-based methods use a numerical model of the structures to identify structural damages. Initially, the numerical model is calibrated using the baseline measurement to reflect the structural behavior at the healthy state. Then, the model is updated to reproduce the measured response of the structure and the comparison of the updated model and the initially calibrated model can provide information on the damage location and extent [61]. Usually, the finite element (FE) model of the structure is constructed and FE model updating is conducted to calibrate the model to reflect the structural behavior [62]. The model updating involves minimizing an objective function with respect to the parameters that represent the structural properties. There have been many studies on the model updating and different optimization methods were used. The main advantage of the model-based methods is that the identification of the damage location and extent is straightforward [63]. However, it heavily relies on a detailed and accurate model of the structure which may be difficult to obtain. Furthermore, one common problem of model updating is that there are multiple solutions and although a solution can be obtained through optimizing the objective function, the obtained solution still may not correspond to the actual

damage case. In this case, a visual inspection will be helpful to identify whether the identified damage is a false positive.

Application of BWIM in SHM. A well-calibrated BWIM system should be able to accurately identify the vehicle weight. However, if the bridge structure suffered damage, then the calibration can no longer reflect the actual behavior of the bridge, which will result in identification errors of the vehicle weights. Cantero and Gonzalez proposed a Level 1 damage-detection method using the relative difference of GVW identified from the BWIM and pavement-based WIM as the damage indicator, EBWIM (Figure 45) [64]. It was noted that even if the bridge is intact, there still exist errors of GVW identified in both systems due to factors other than the damage such as measurement noise. Thus, the EBWIM is averaged over a large sample of trucks to compensate for the dispersion of individual trucks. Simulation study was conducted to test the effectiveness the proposed method. 1,000 trucks were simulated each day and the daily average EBWIM was calculated (Figure 46). The average of 25 daily EBWIM, i.e., monthly EBWIM was used to detect the presence of global and local damages that were modeled as the loss of stiffness. It was found that the proposed damage indicator is sensitive to both global and local damages and that the proposed method is robust in detection damages since it is applicable for different road profiles and it allows for the intrinsic errors in WIM systems themselves.

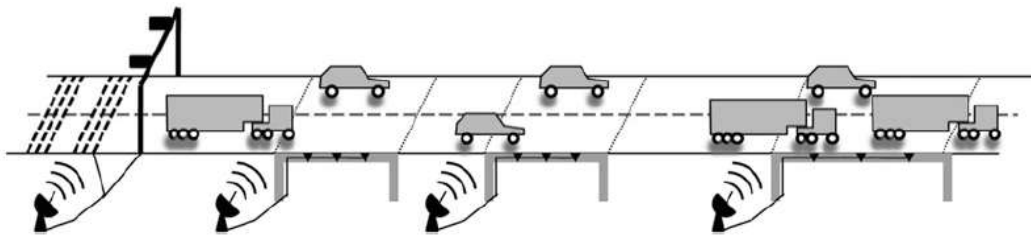


Figure 45
Concept of WIM-based SHM [64]

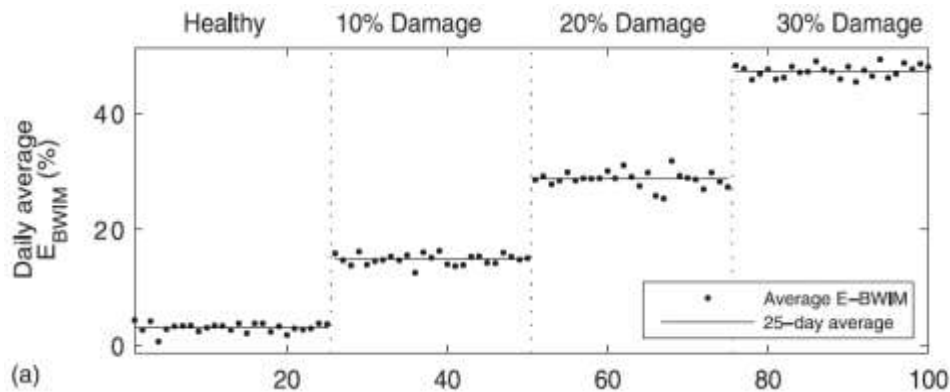


Figure 46
Daily average EBWIM for different damage cases [64]

Cantero et al. proposed a Level 1 damage detection method using the concept of virtual axle (VA) [65]. When identifying the axle weight in BWIM, the vehicle was assumed to have a weightless axle in addition to its existing axles as shown in Figure 47. This additional axle is termed “virtual axle (VA).” It was shown that if there is no change in the influence line of the structure, i.e., the structure is intact, the BWIM will estimate the weight of the VA to be zero. Otherwise, the estimated weight of the VA will be different than zero, which indicates the presence of structural damage. Based on this, a damage index named VA^* is defined to reflect the weight of the VA relative the GVW identified without the VA. The VA^* is averaged over a large number of trucks to reduce the influence of errors due the noise and dynamic effects. The simulation results indicate that the proposed method is able to detect small local damages. However, it should be noted that the proposed method is only applicable to statically indeterminate bridges with relatively short span length.

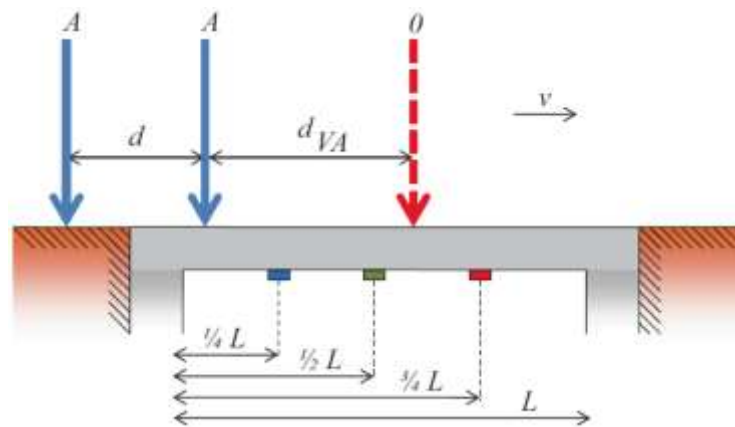


Figure 47
Concept of the VA for damage detection [65]

Carey et al. investigated the possibility of using moving force identification method for damage detection of bridges [66]. They found that the axle force history is sensitive to the structural damage as shown in Figure 48. However, different vehicles have different properties, which results in different axle forces that are not comparable. Thus, the mean axle force of a large number of vehicles with the same axle configuration is used as the damage indicator. The results show that the proposed method can successfully detect local damages and has the potential to provide possible locations of damage.

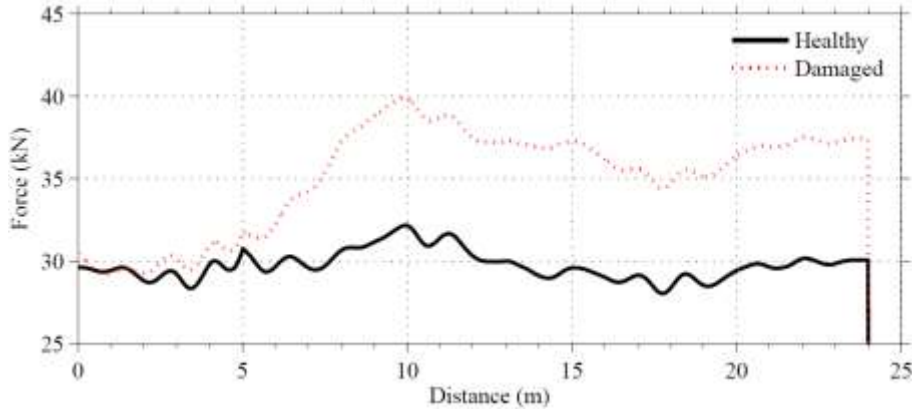


Figure 48

Inferred axle force for the same vehicle at health and damaged state of the bridge [66]

Gonzalez and Karoumi proposed a model-free damage detection method using BWIM and machine learning method [67]. The proposed method utilizes the vehicle information identified from the BWIM system as input to an artificial neural network (ANN) that is able to predict the deck acceleration. Since the ANN is trained to predict the behavior of the structure at its healthy state, the different between the predicted acceleration and measured acceleration can indicate possible damages of the structure. The framework of the proposed method is shown in Figure 49.

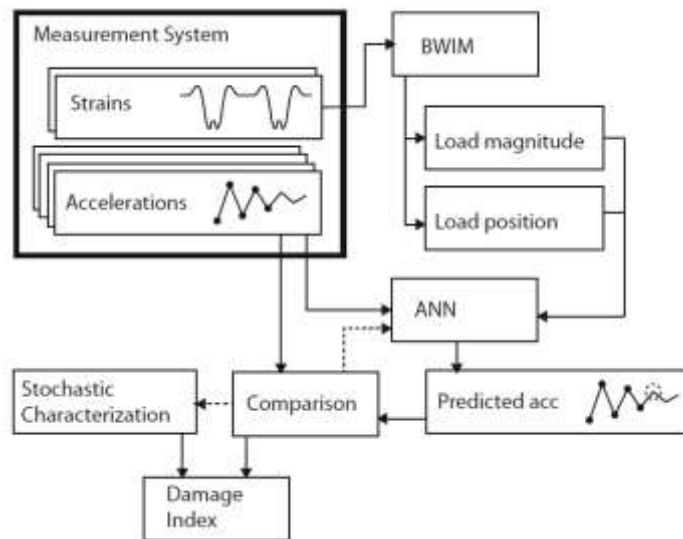


Figure 49

Framework of the damage detection method proposed by [67]

Bridge Condition Assessment. Bridge load rating is common practice used to assess the in-service condition of bridges. Bridges are typically rated every two to five years depending on their conditions. The AASHTO load and resistance factor rating (LRFR) specifications define the rating factor as:

$$RF = \frac{\Phi R - \gamma_{DL} DL}{\gamma_{LL} LL (1 + IM)} \quad (60)$$

where, Φ is the system factor; DL is the dead load; LL is the live load; IM is the impact factor or dynamic load allowance; γ_{DL} is the dead load factor; γ_{LL} is the live load factor [68]. The rating factor reflects the safety reserve of the structure. A rating factor larger than one indicates that the bridge has the capacity to carry the live load. Otherwise, the bridge is considered to be vulnerable and there is a need for load posting. In order to be consistent to LRFD design specification, the live load factor is generally chosen to be 1.75 [1]. However, the factor of 1.75 may be overly conservative for some bridges since the design codes need to cover a wide range of bridges and there exist significant uncertainties.

The BWIM system is able to collect the site-specific traffic data and thus can significantly reduce the uncertainties for condition assessment. The collected site-specific traffic data can be used to calibrate live factor specific for the bridge under assessment, which can help avoid unnecessary load posting and increase the efficiency of transportation system. Zhao et al. used the data collect by pavement-based WIM and BWIM systems in Alabama to calibrate the statewide live load factor [69]. They found that the live load factor specified by the LRFR is overly conservative for the economic assessment of bridges. Accordingly, they suggest that the ALDOT adopt the state-specific live load factors to improve the load rating especially when the LRFP specified load factor results in the bridge to be posted. In addition, they also found that different traffic direction and seasonal variation do not have a significant effect on the live load factor. Similar works have also been conducted by [70].

In addition, when the BWIM data is collected over a relatively long period of time, the statistical characteristics of vehicle weight can be obtained and the future vehicle weight can be predicted using certain projection methods. The predicted future vehicle weight can be used for traffic planning and assessing the condition of the bridge during its remaining life, which can provide essential information for bridge management and maintenance.

APPENDIX II

Sample Time History of Sensors

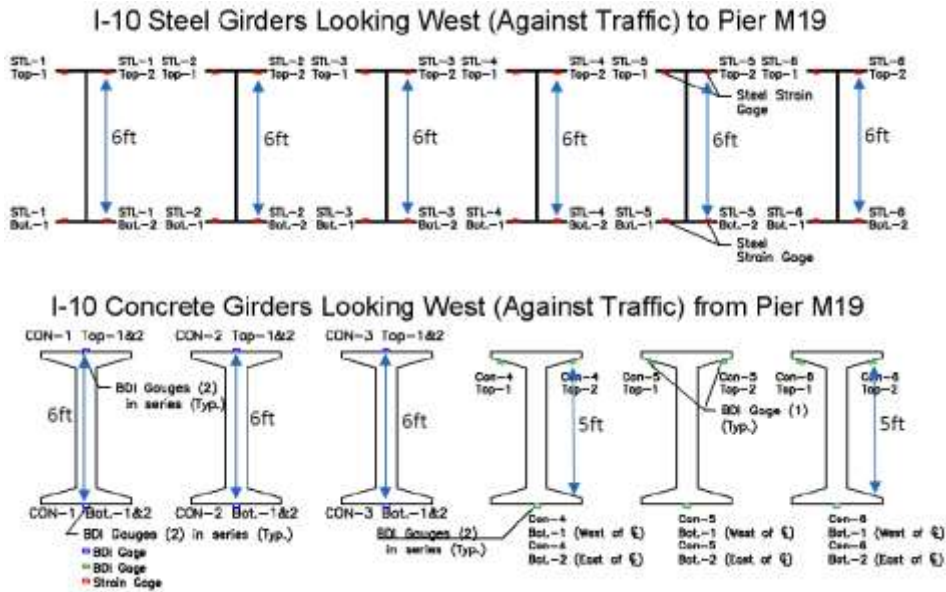
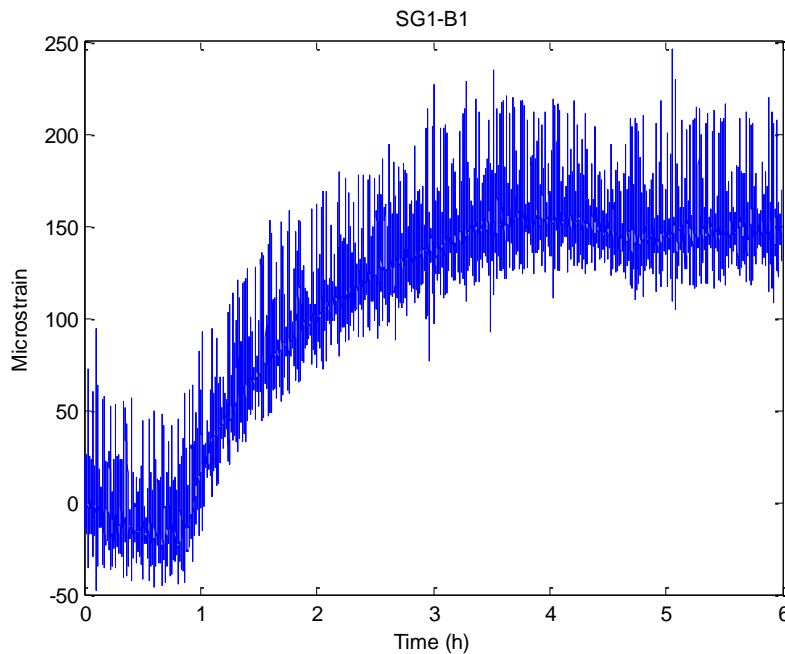
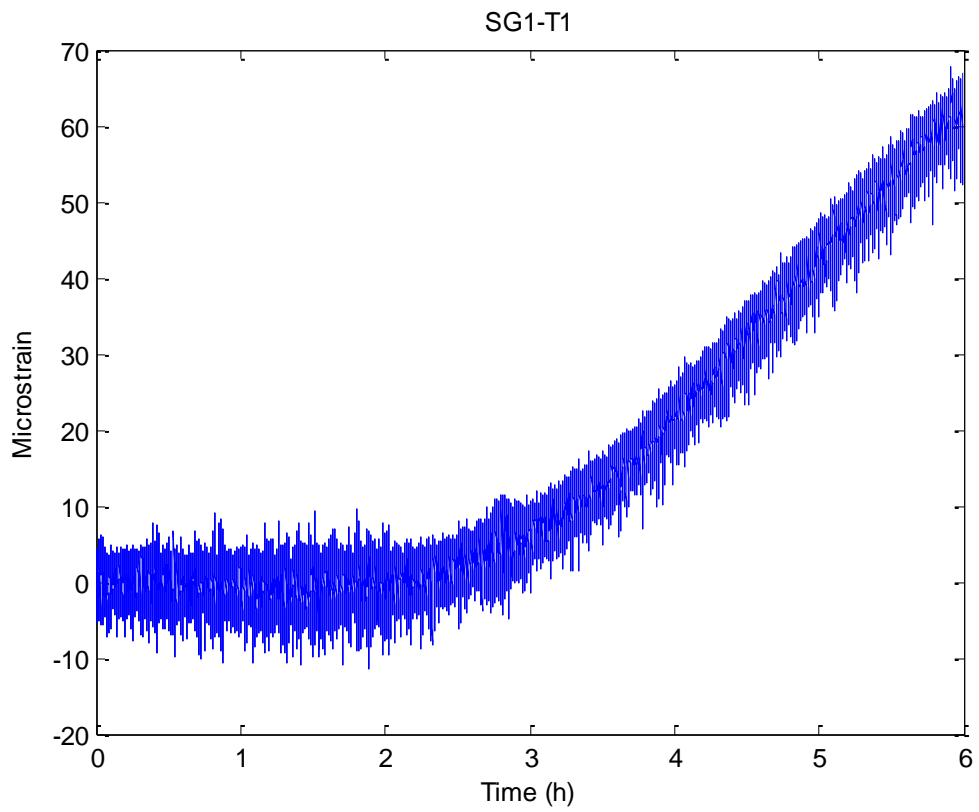
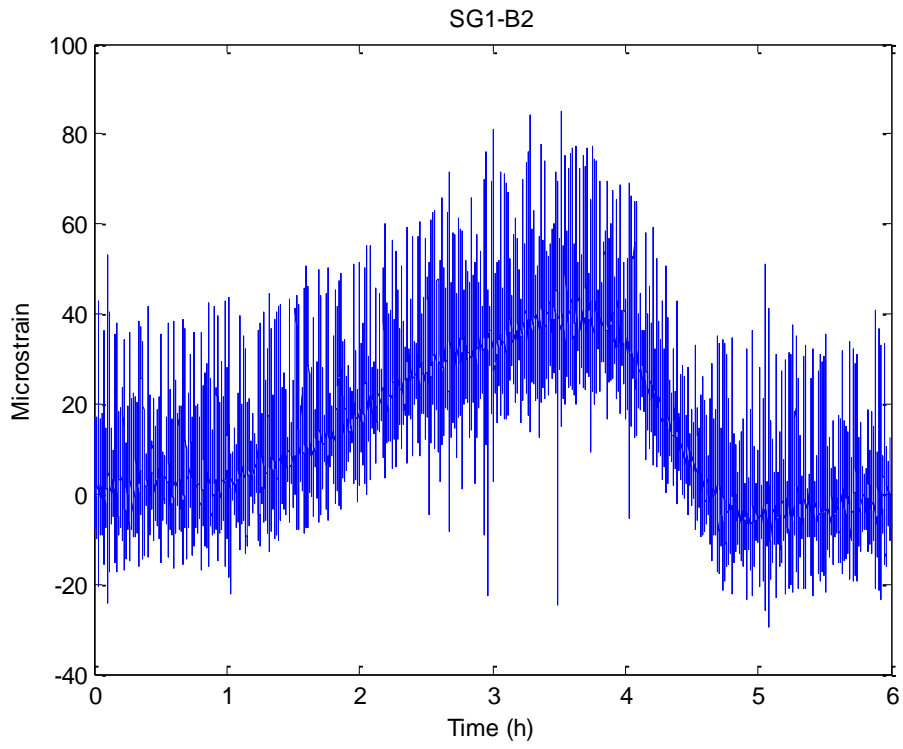


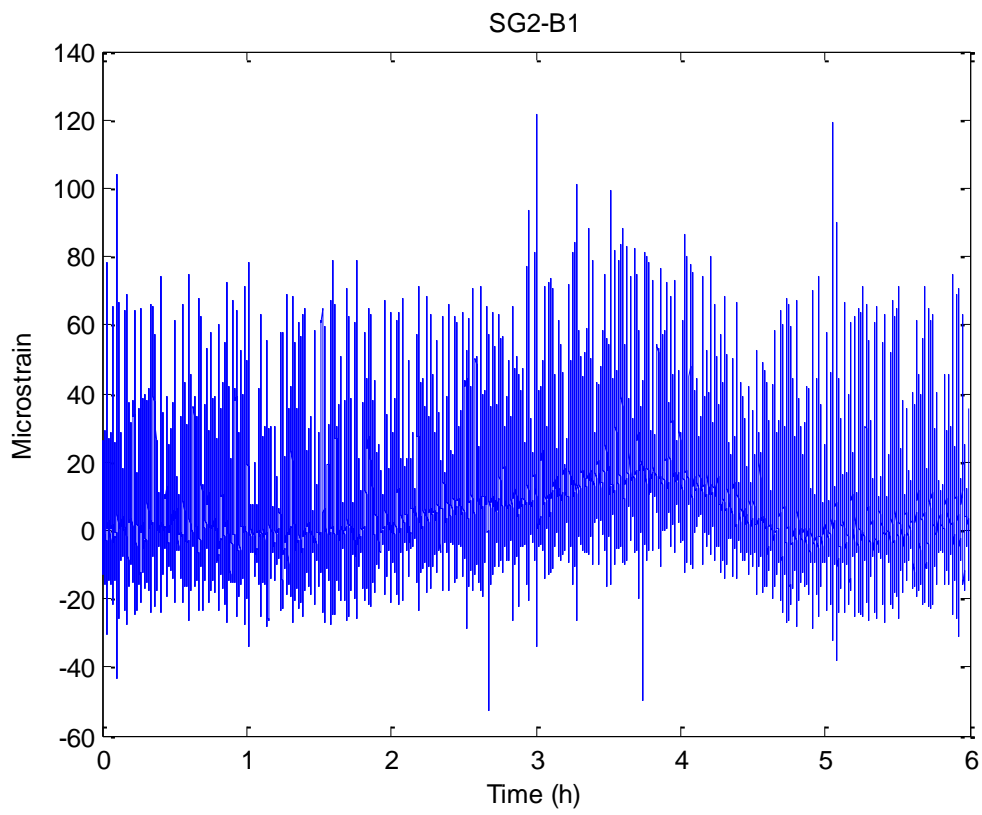
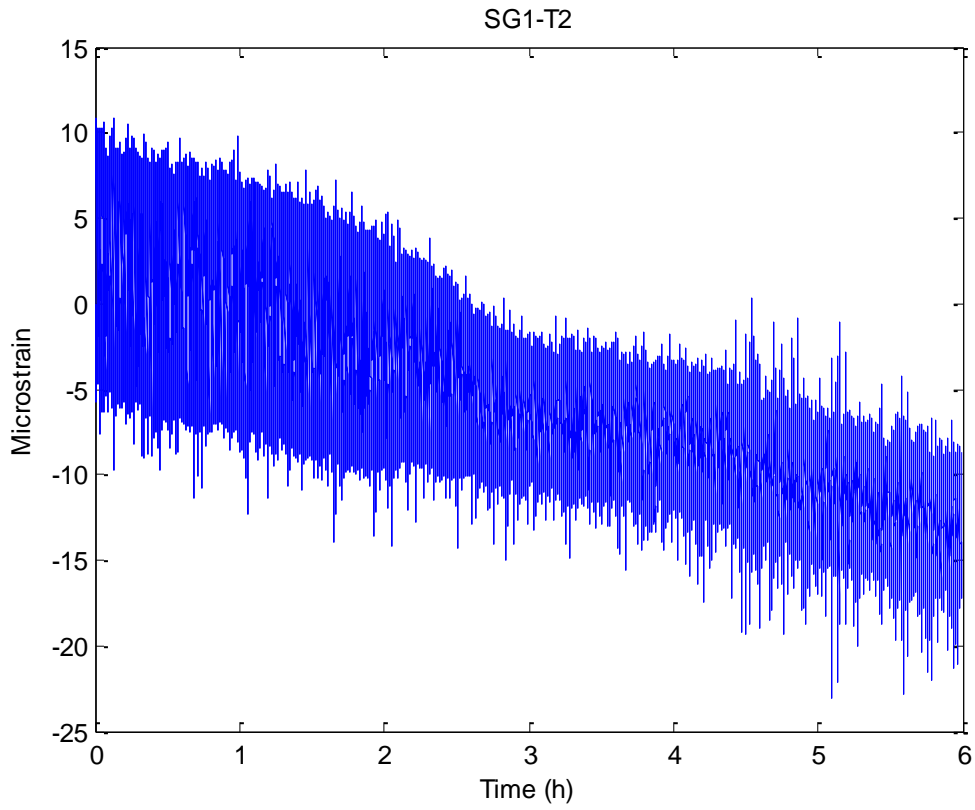
Figure 50

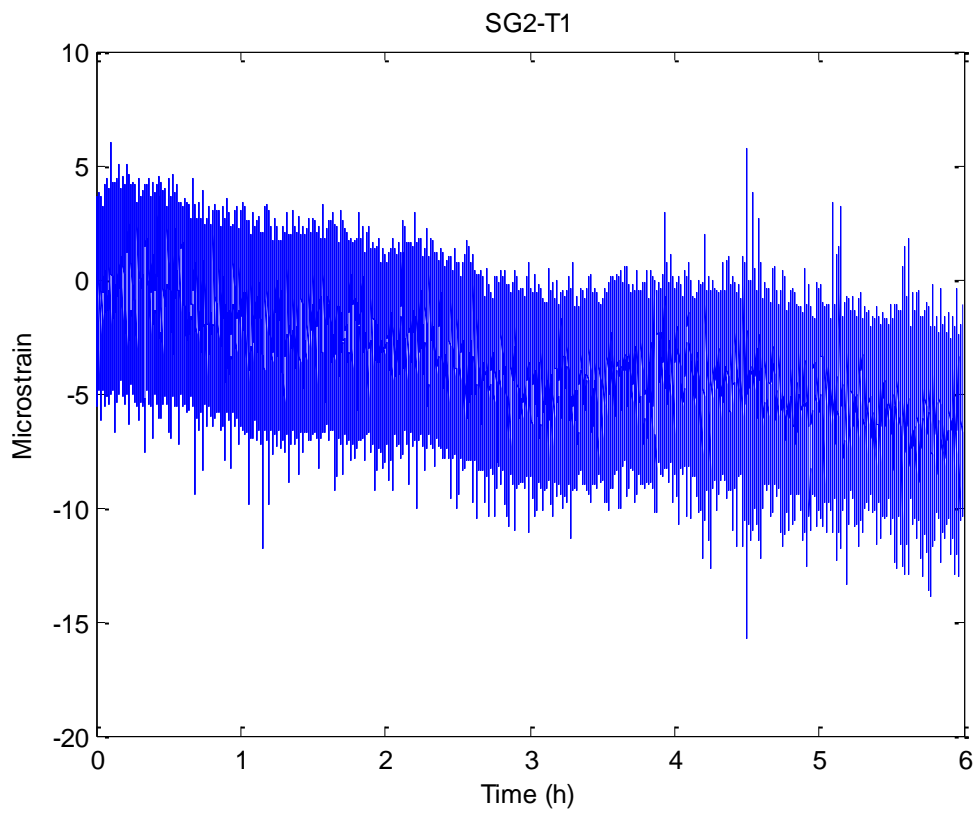
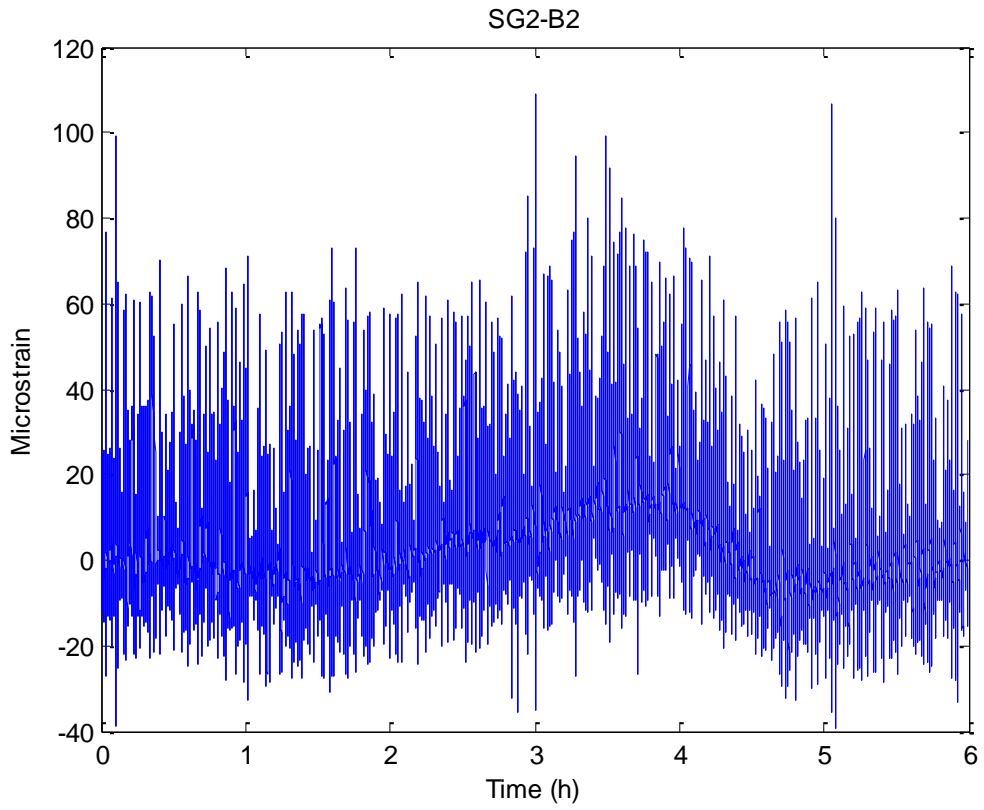
Sensor locations for the monitored spans of the I-10 Twin Span Bridge

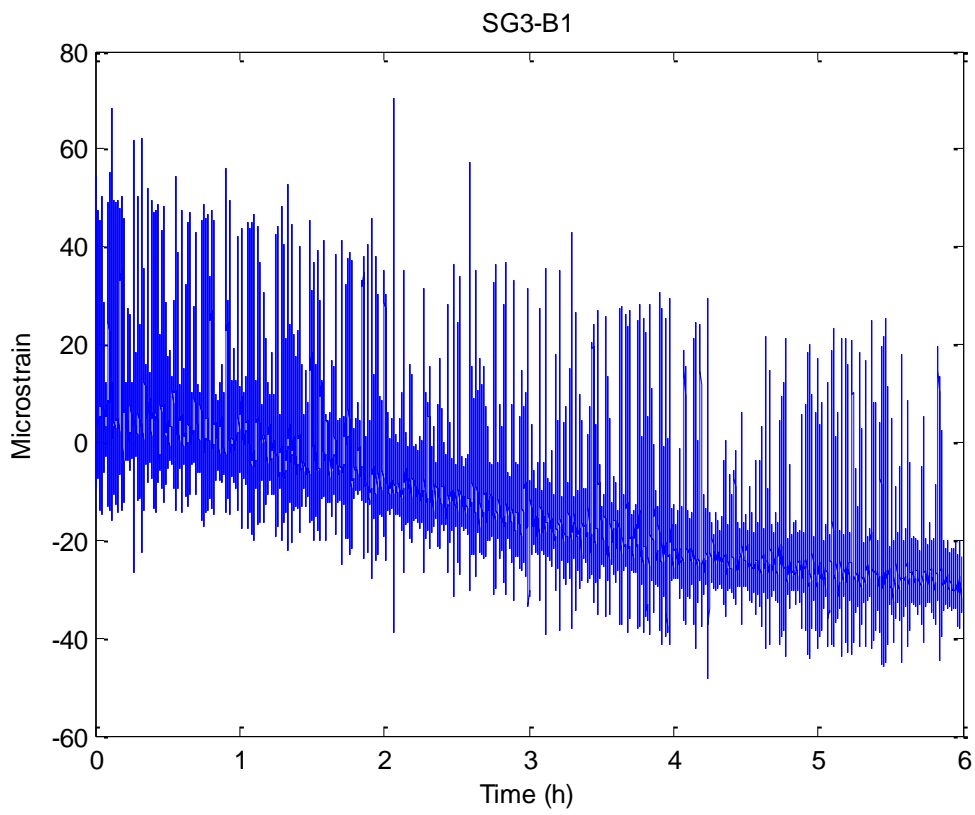
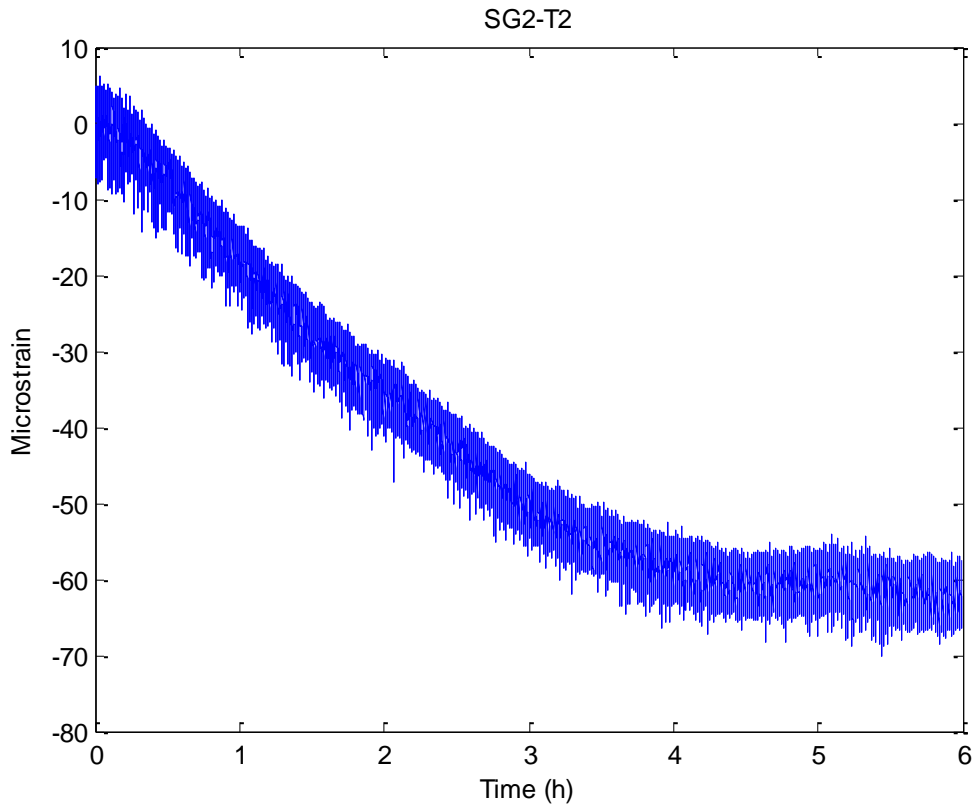
Sample time histories of all sensors shown in Figure 50 are plotted below where S=steel, C=concrete, G=girder. B=bottom, T=top:

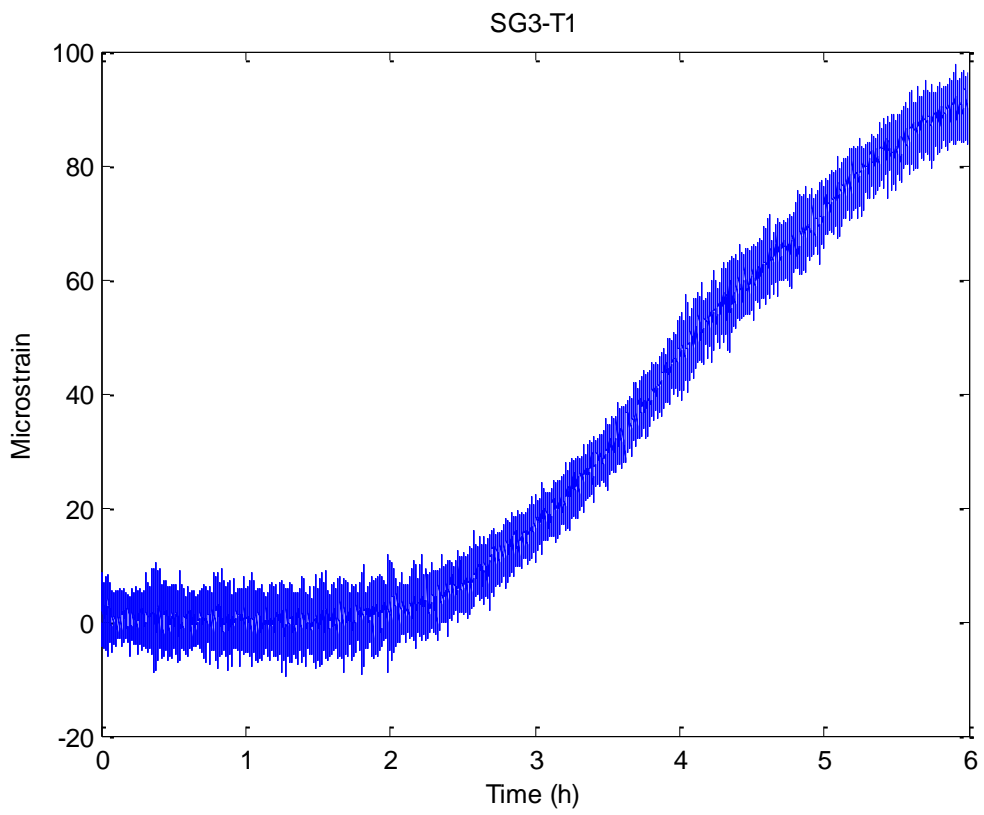
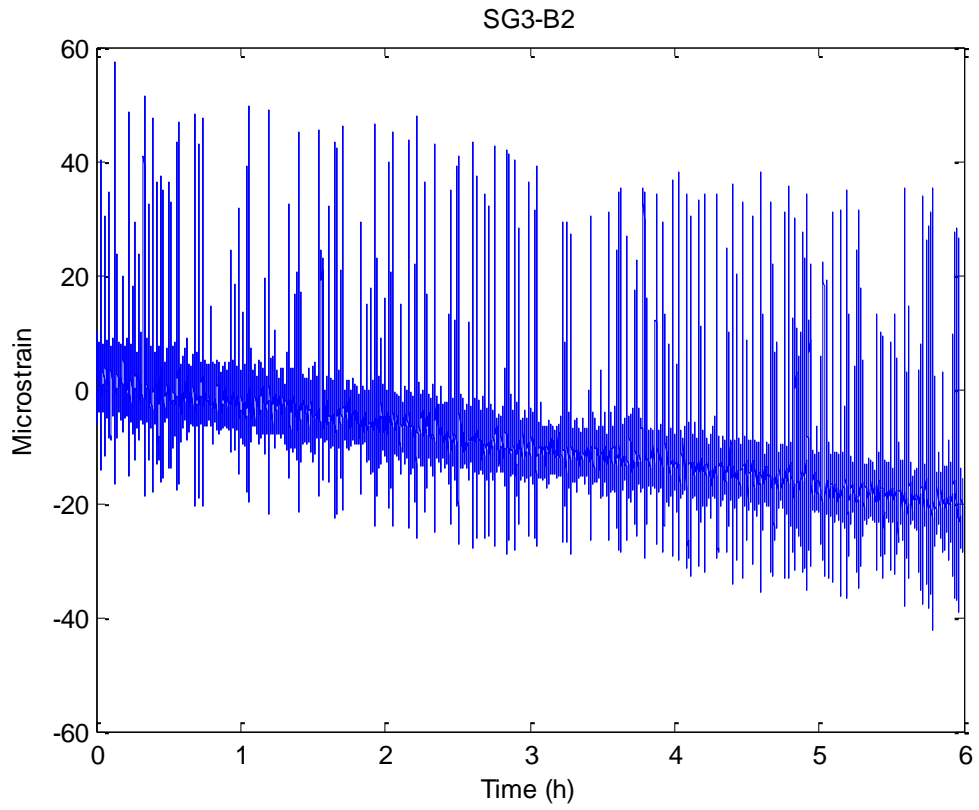


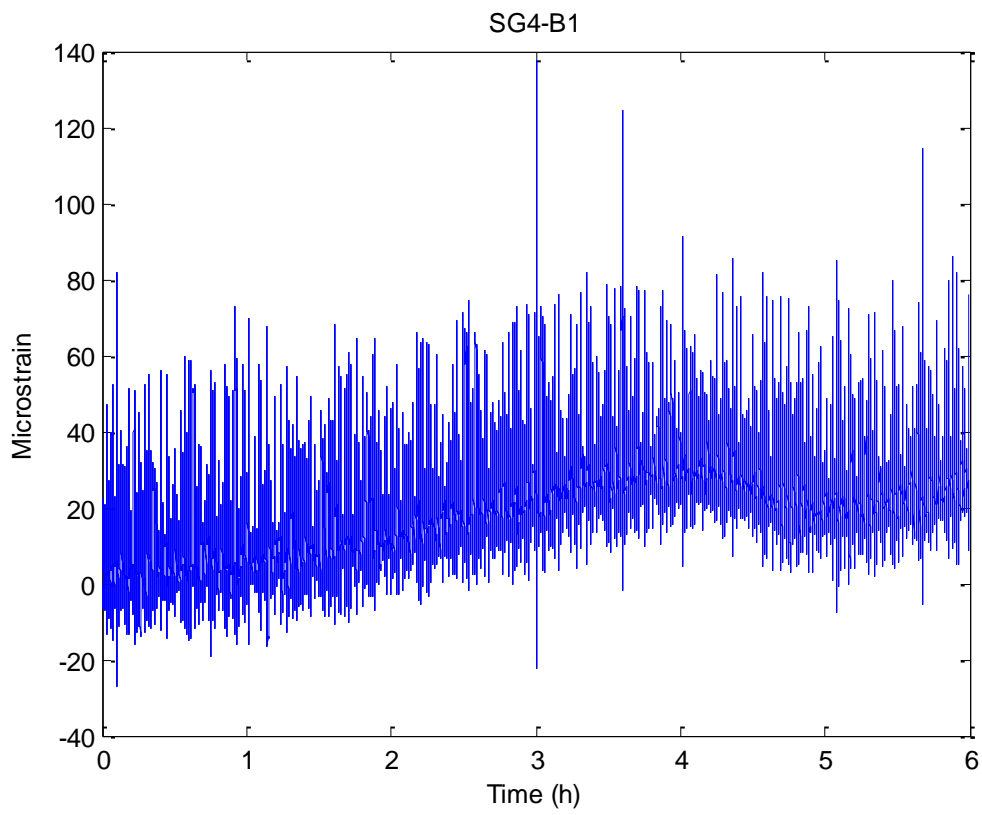
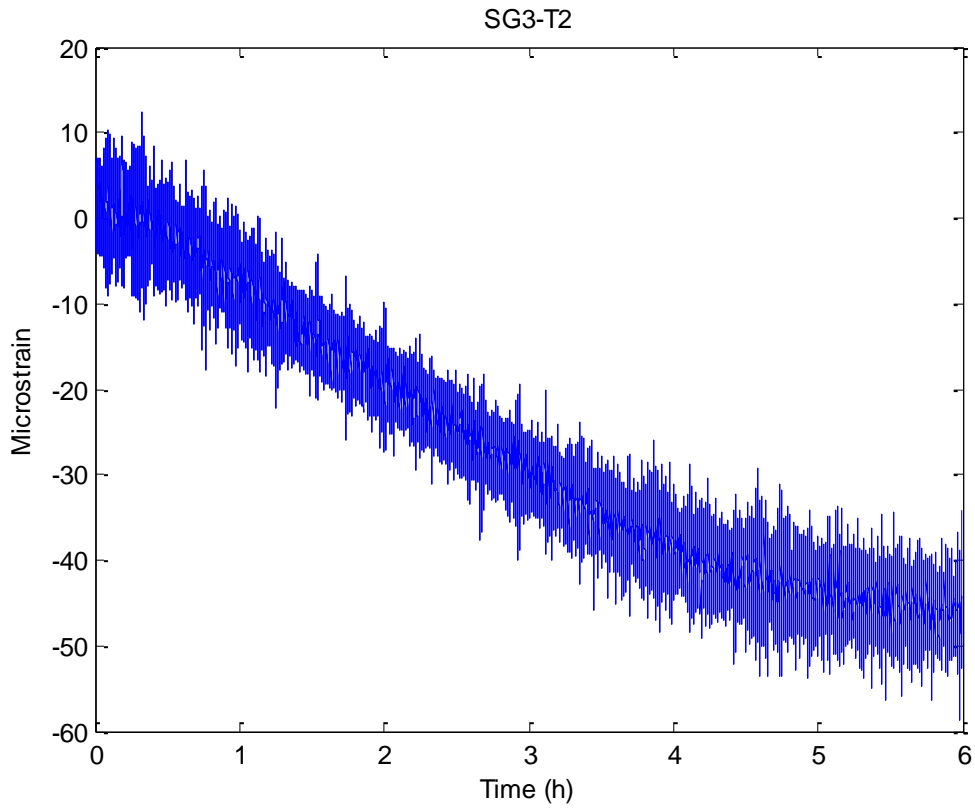


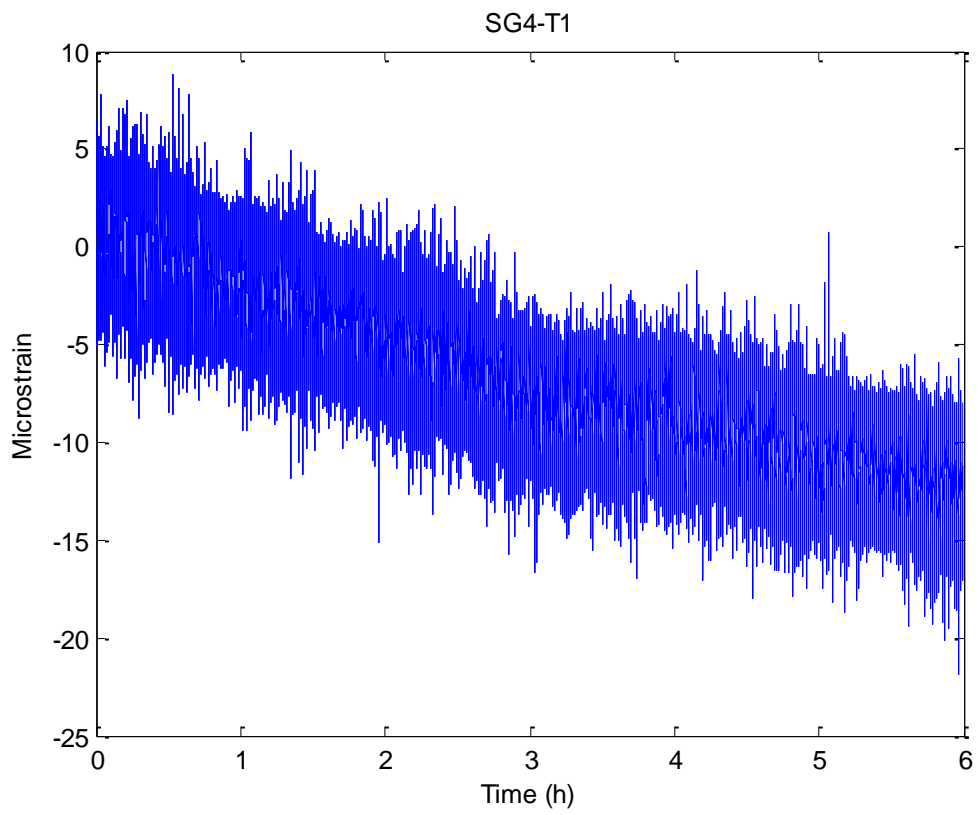
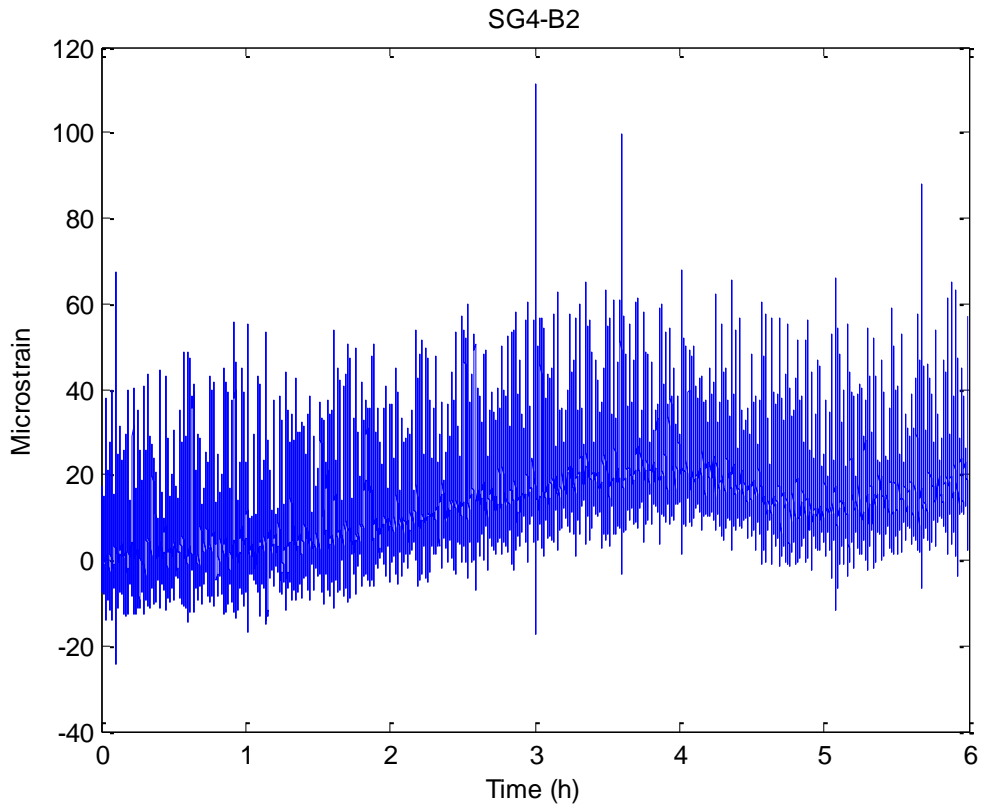


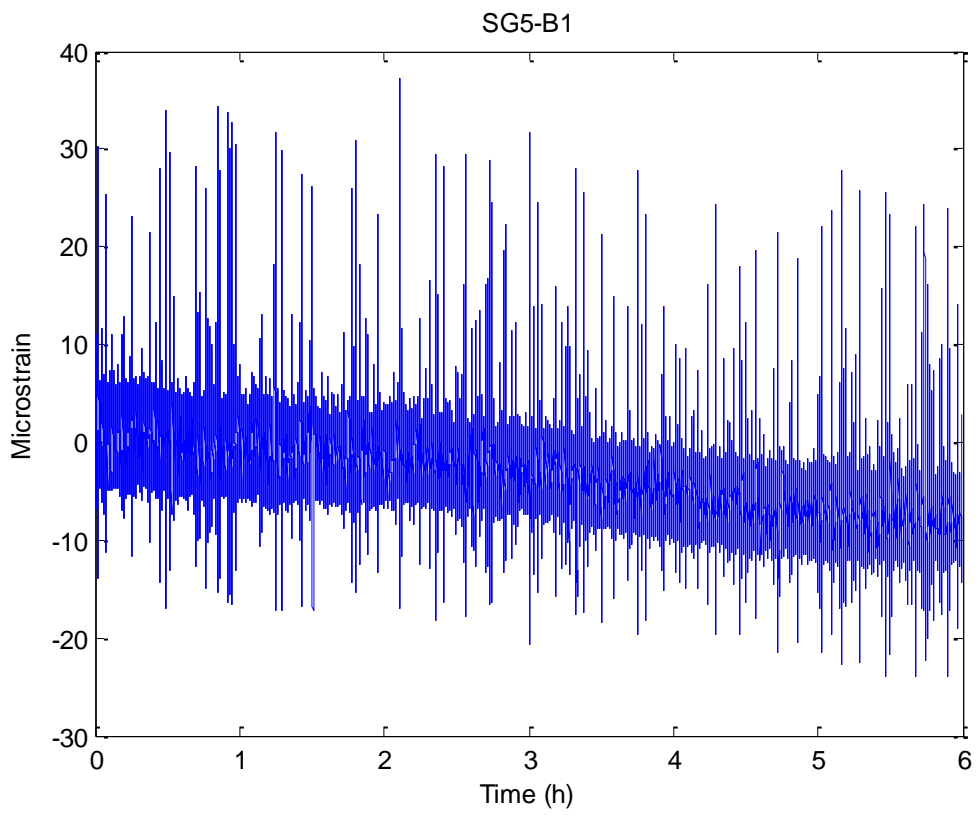
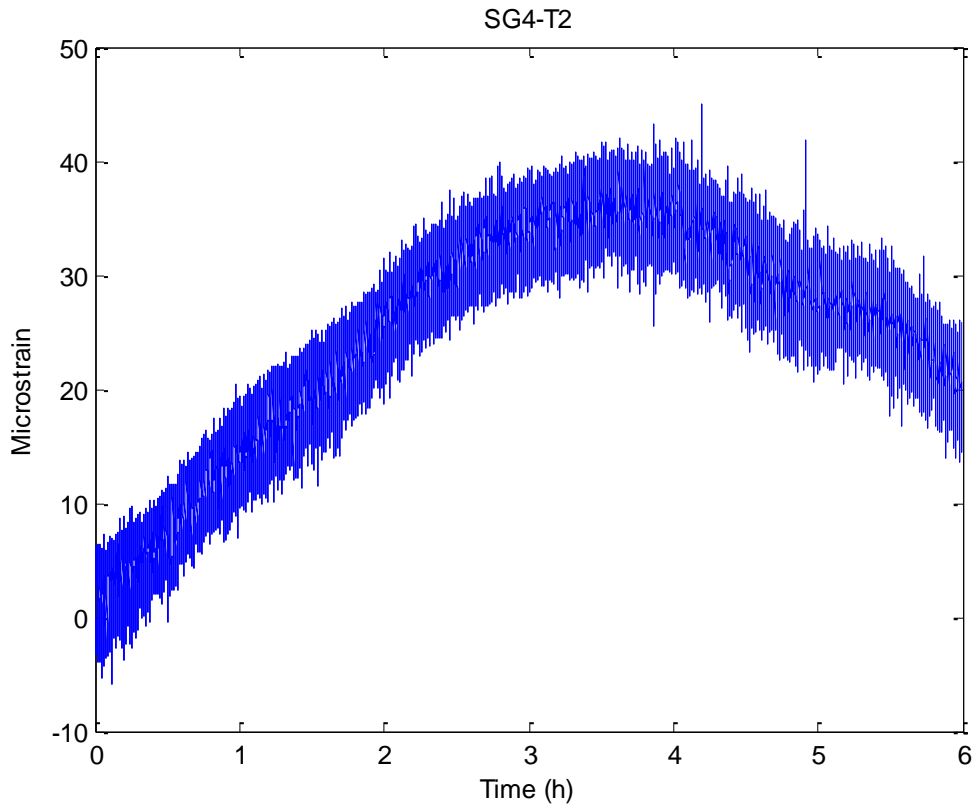


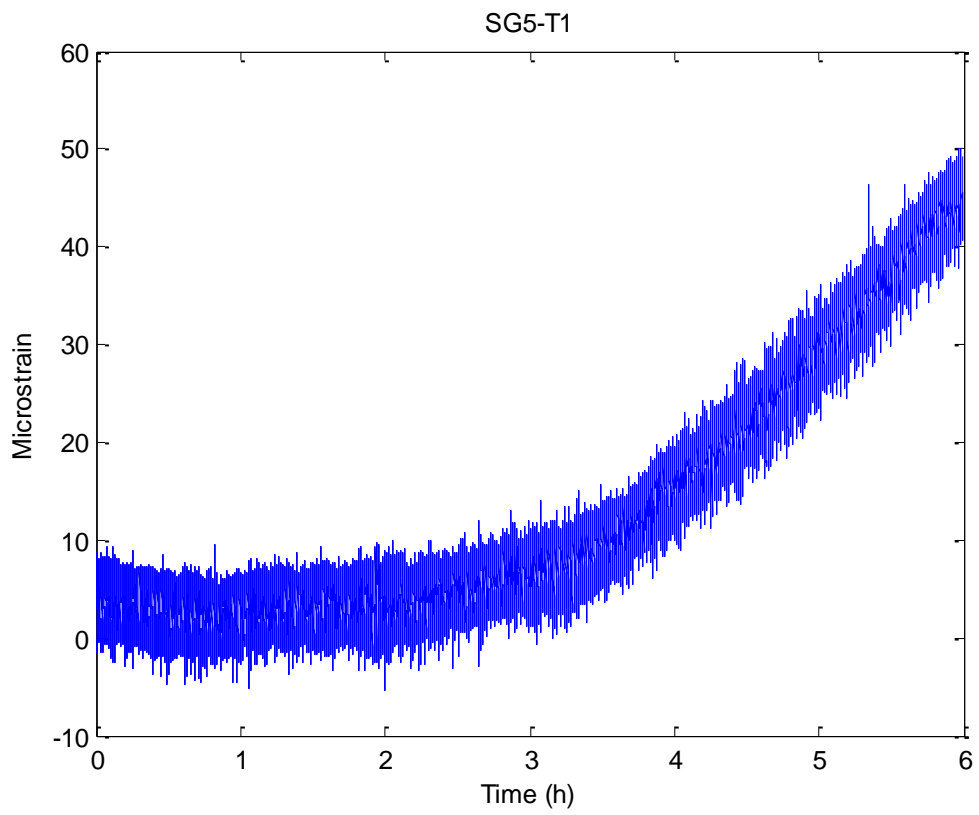
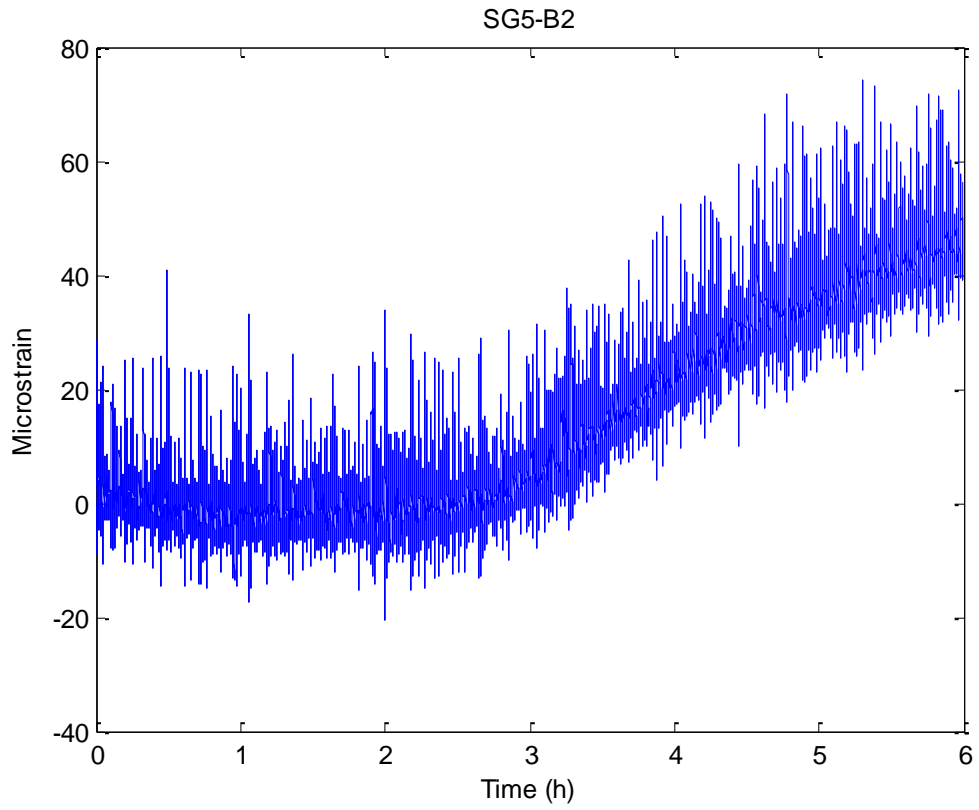


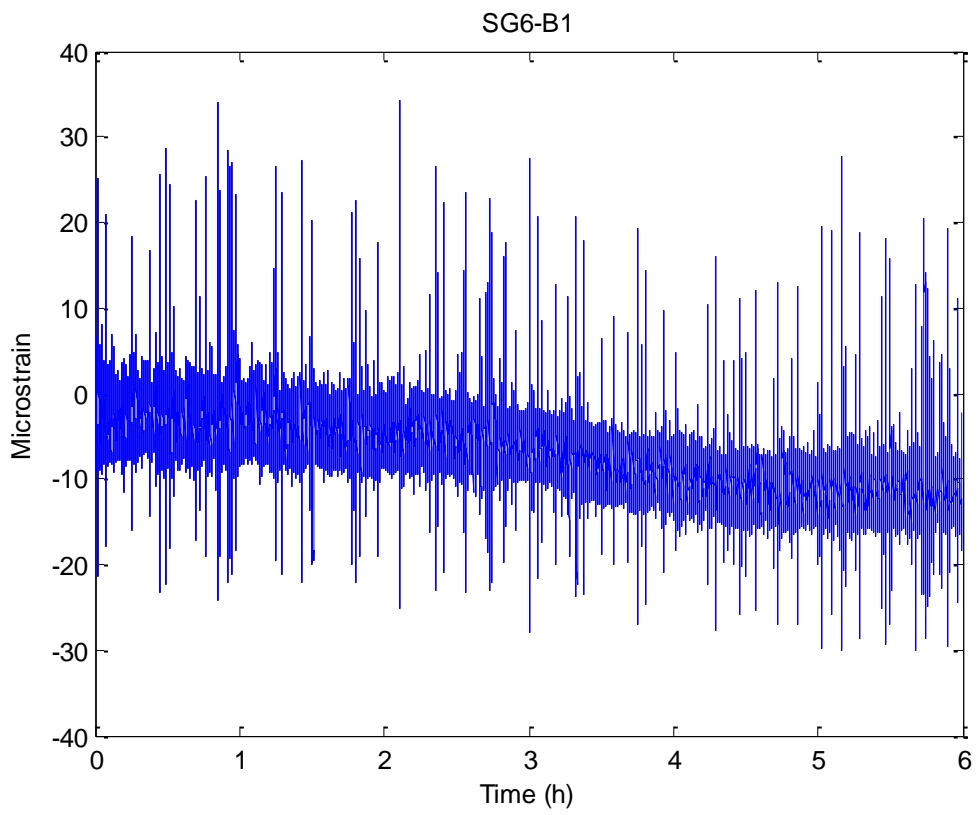
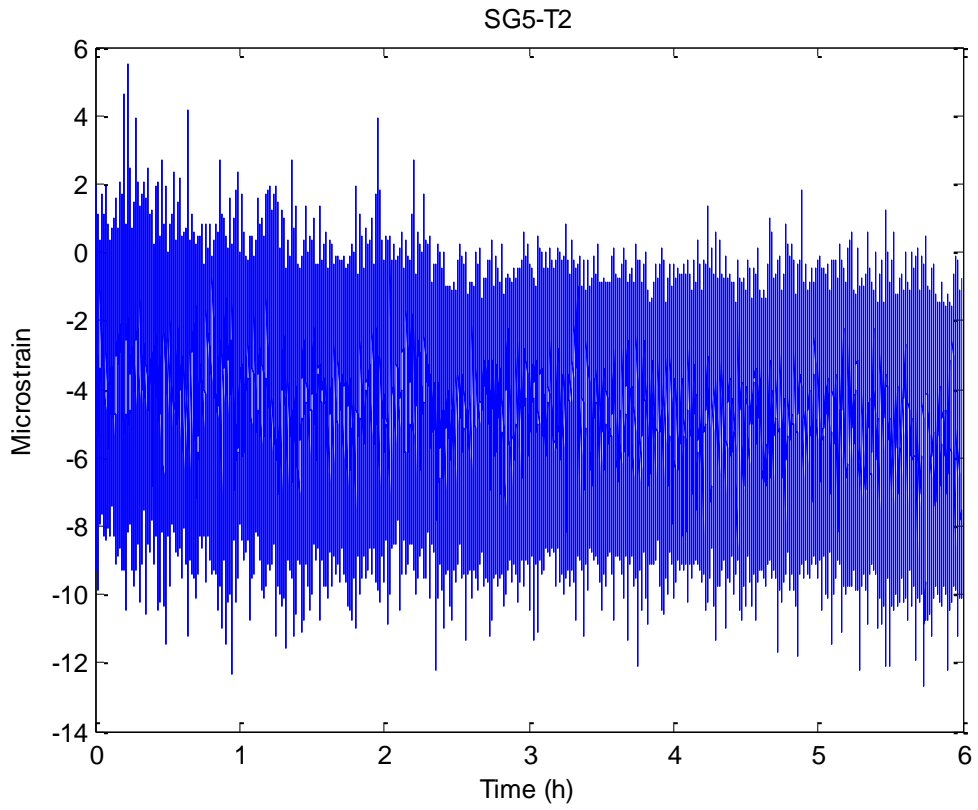


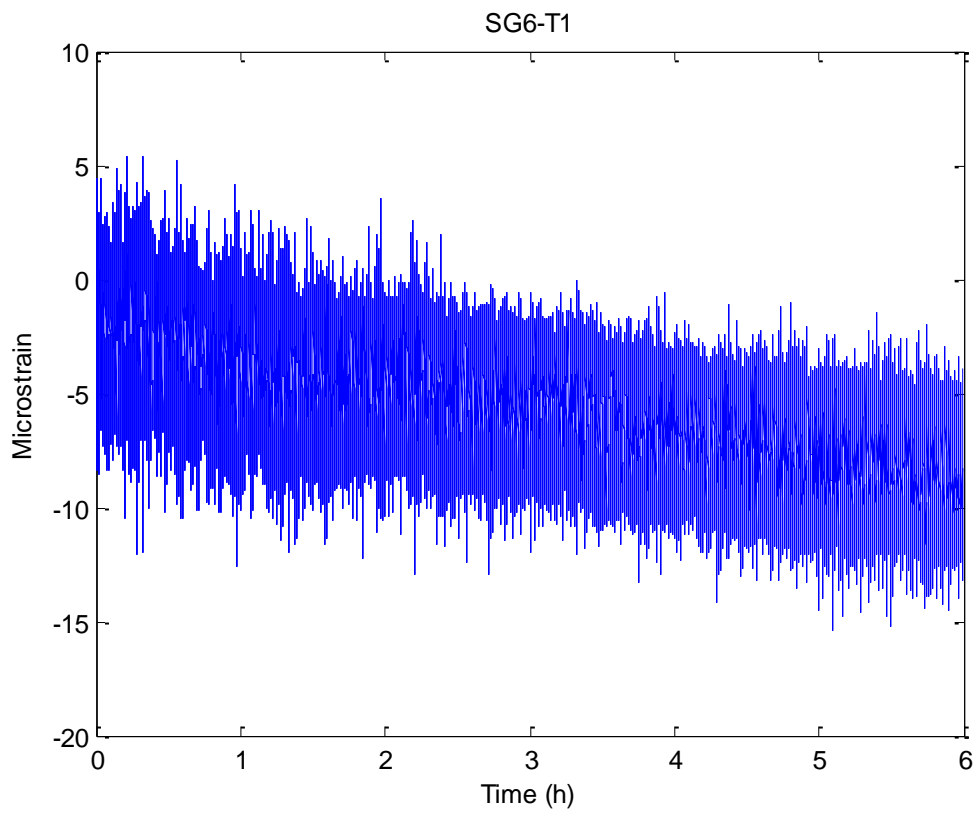
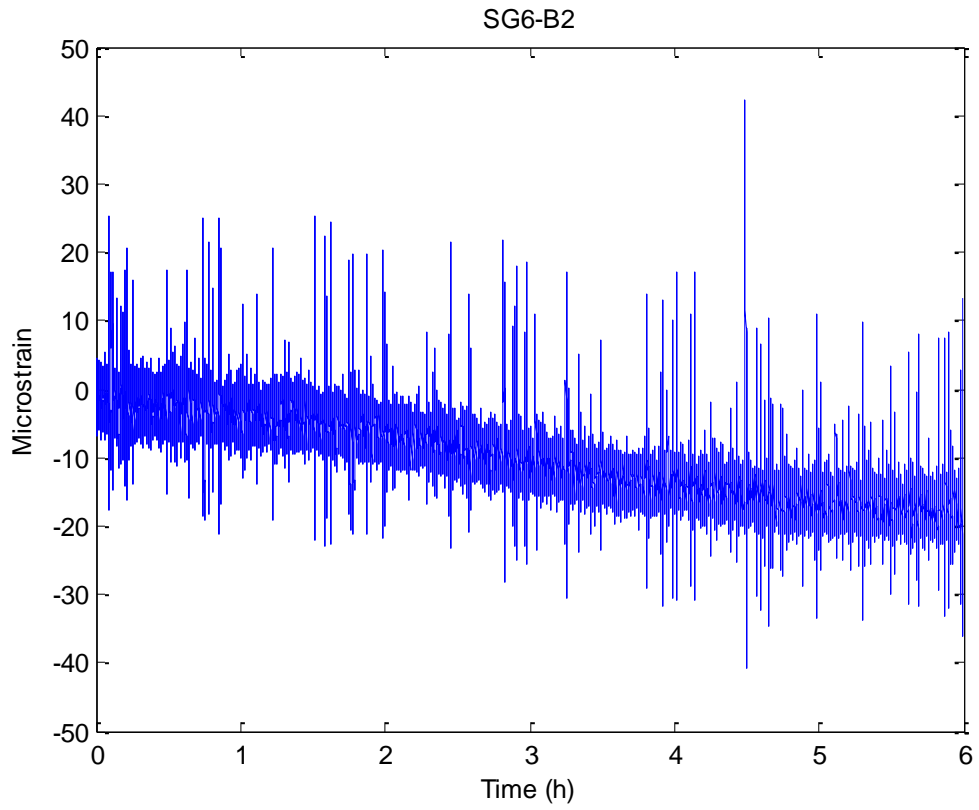


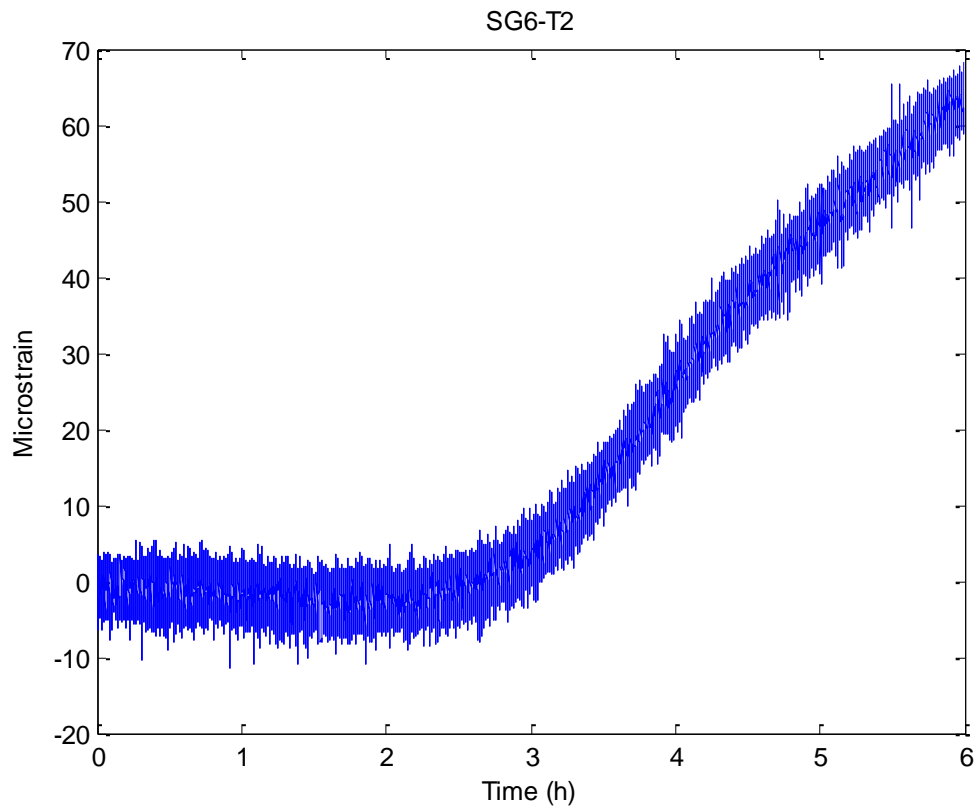


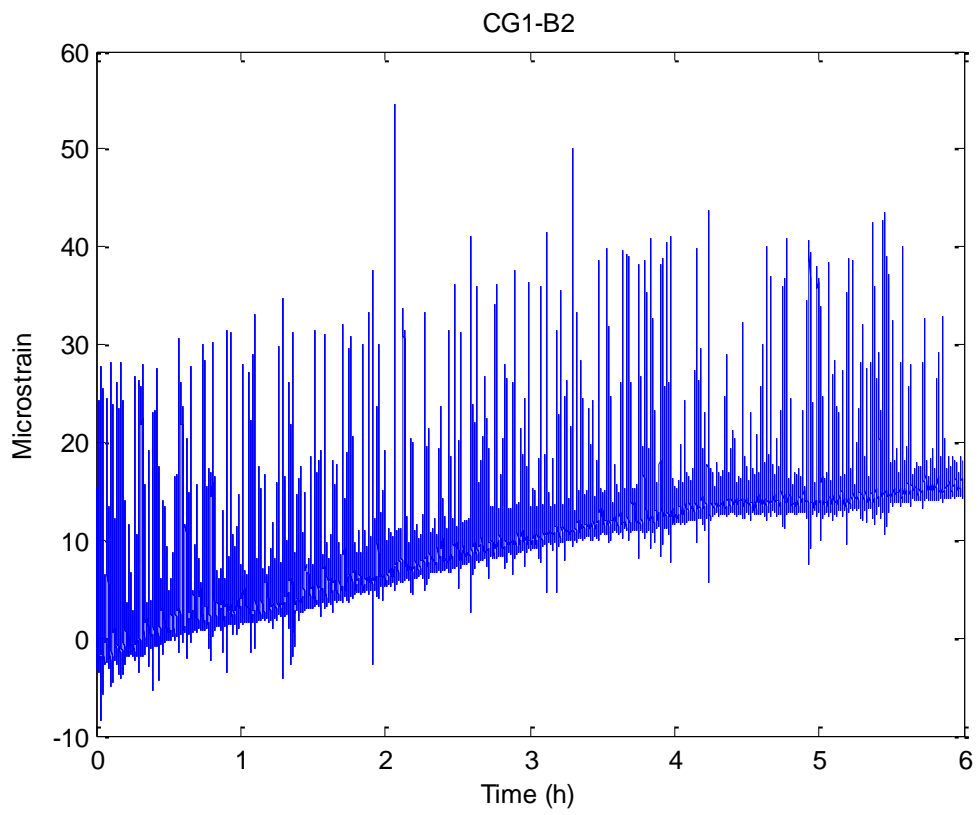
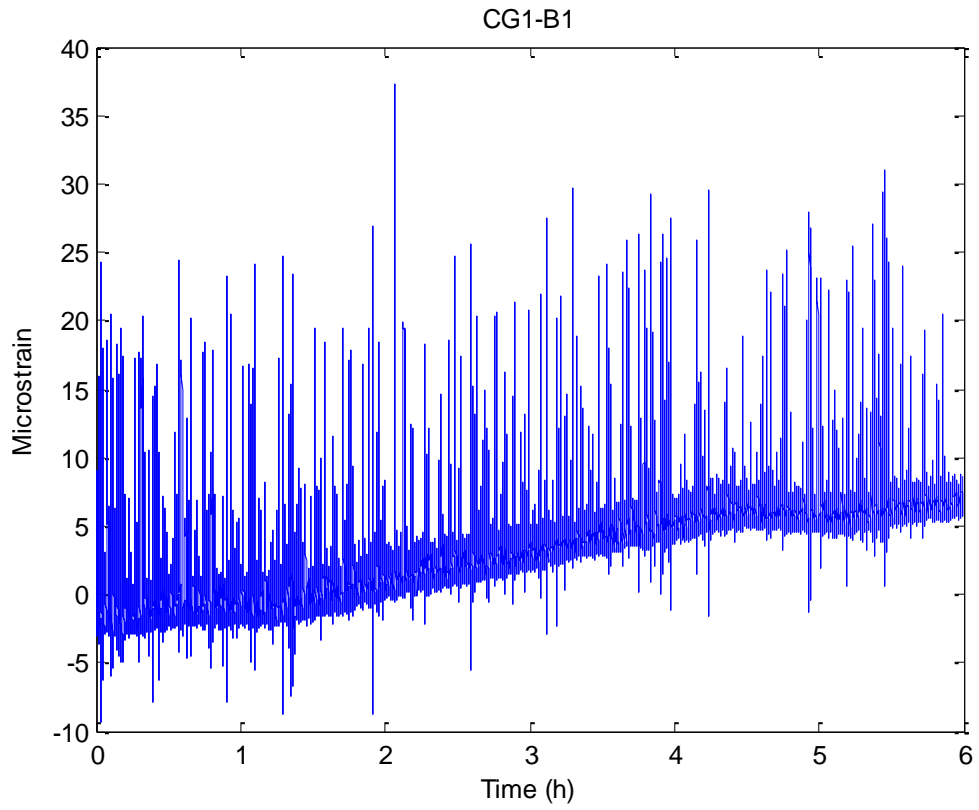


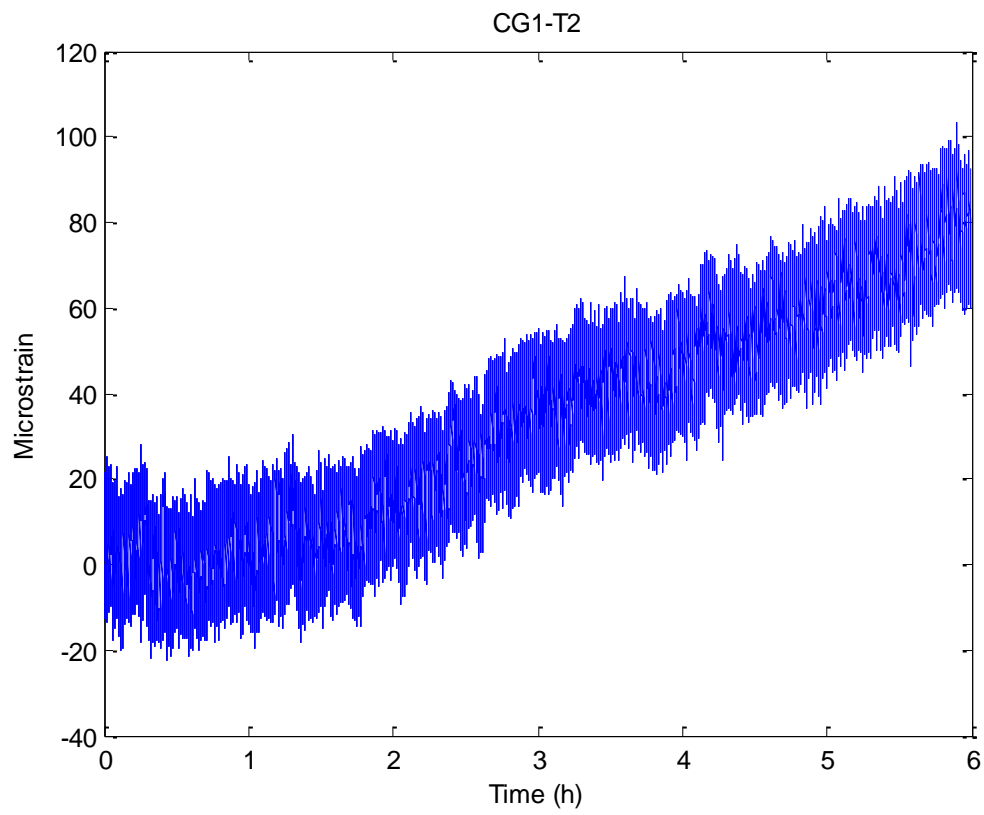
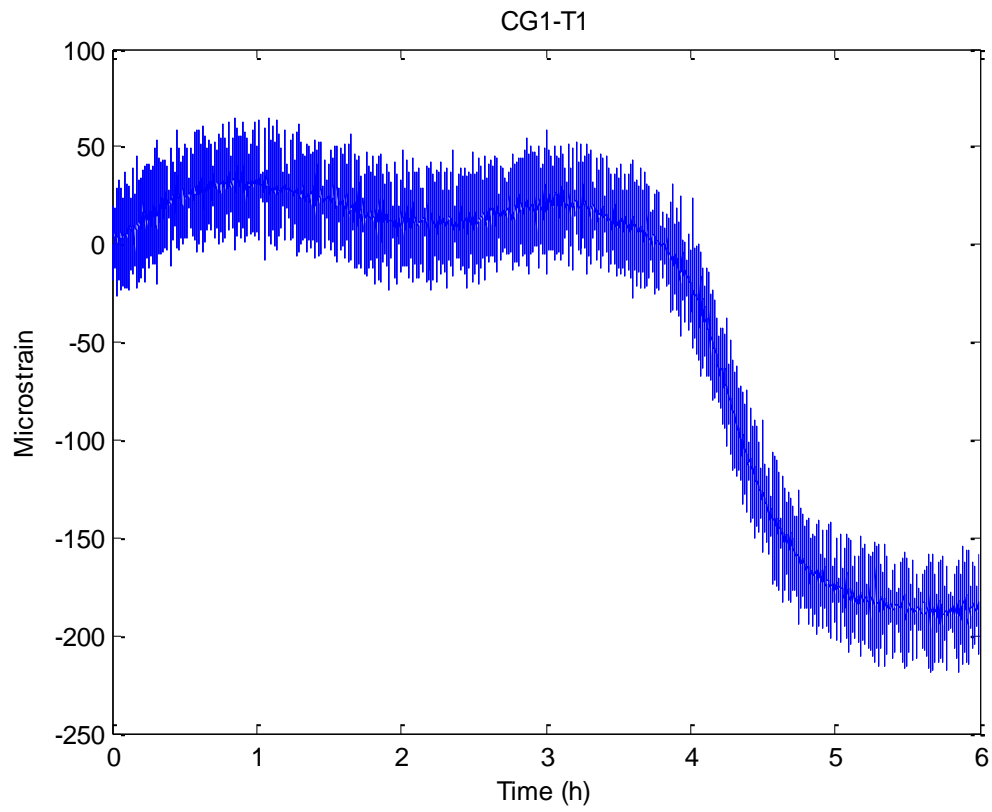


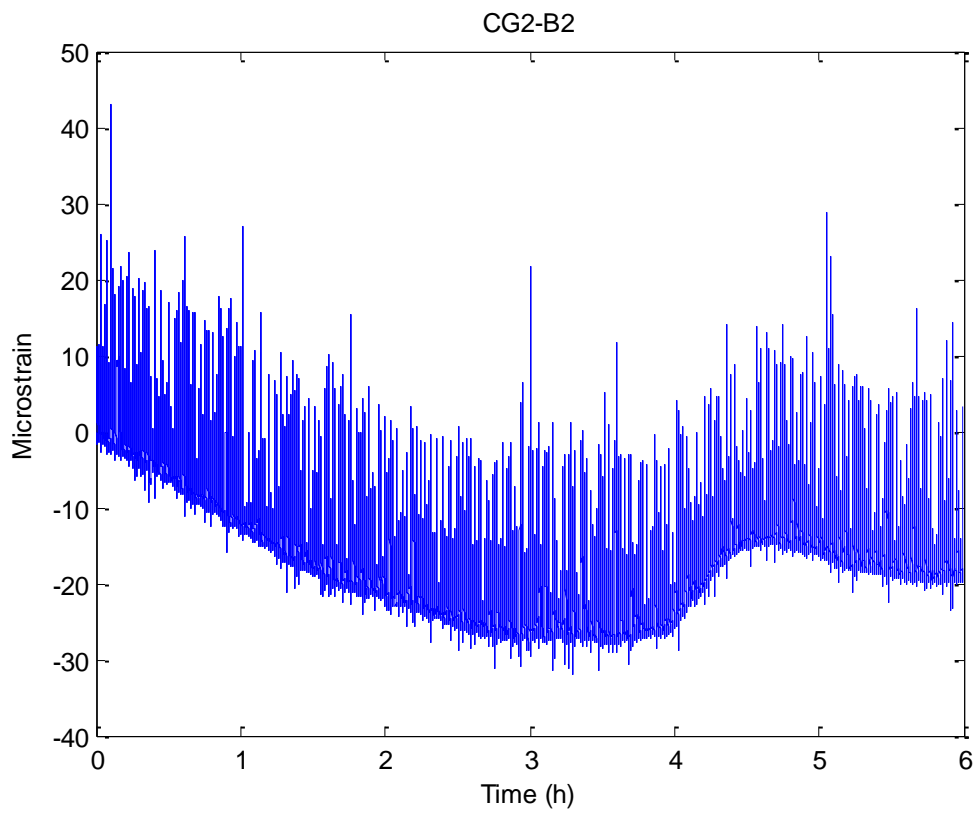
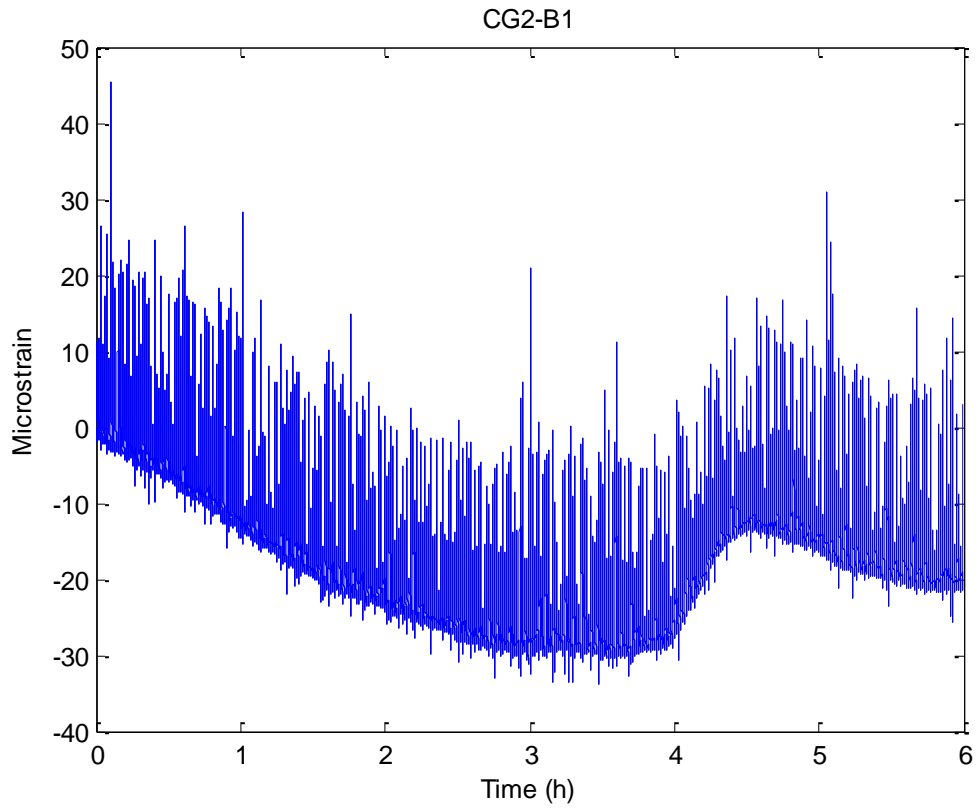


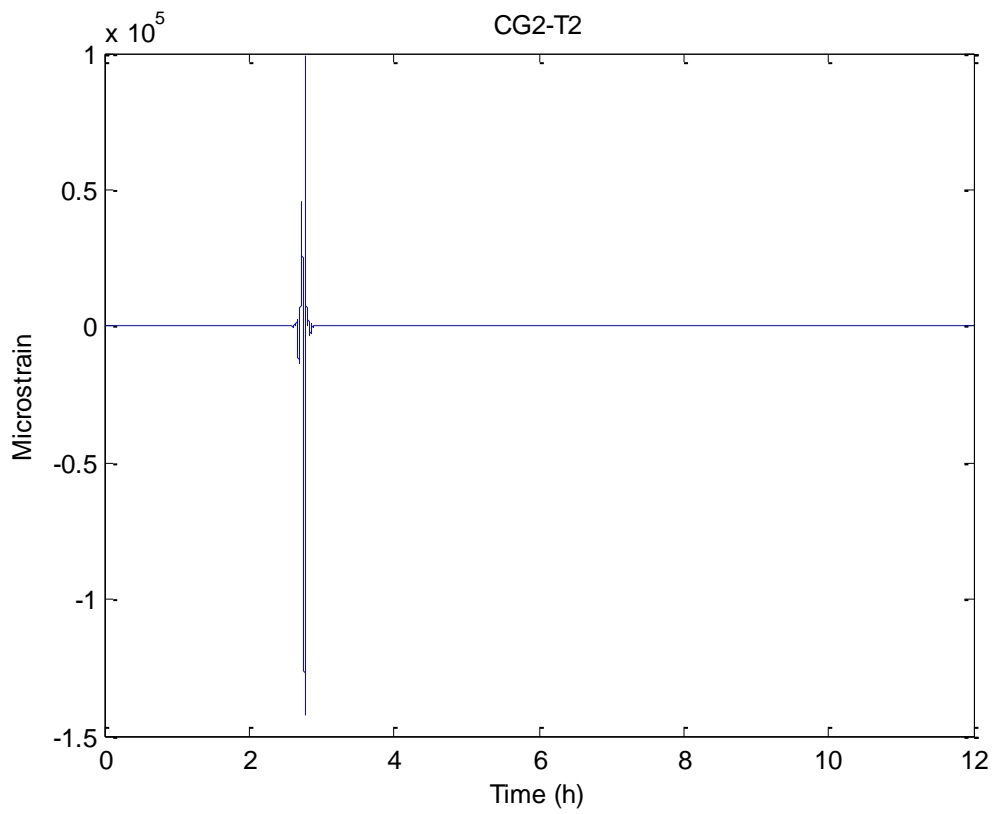
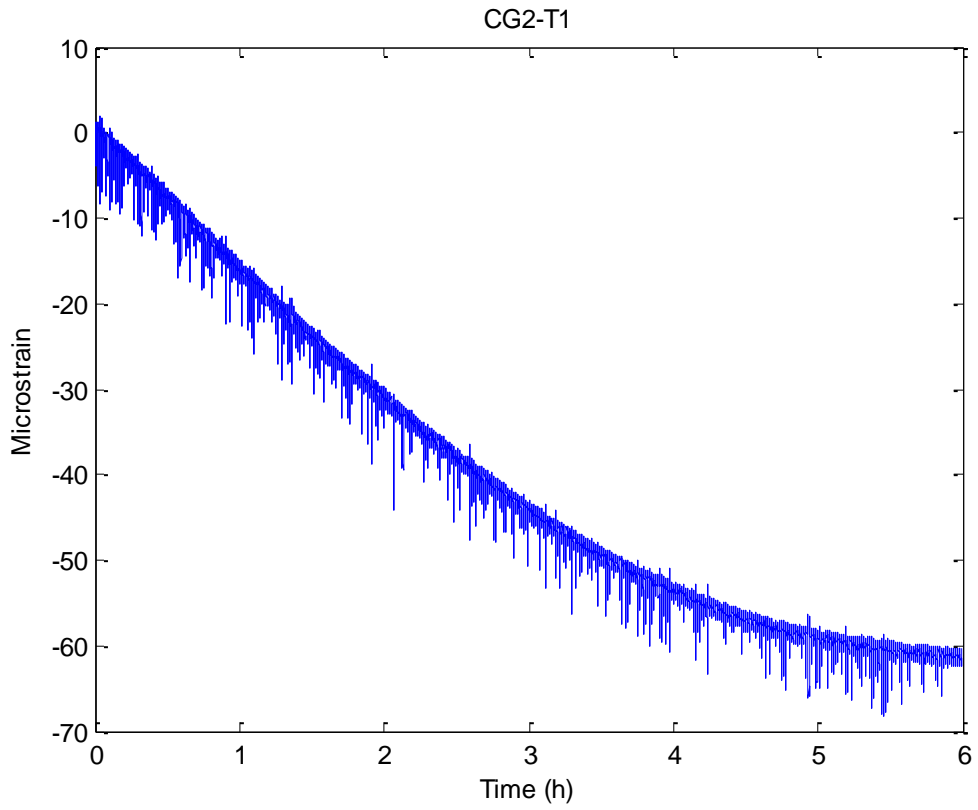


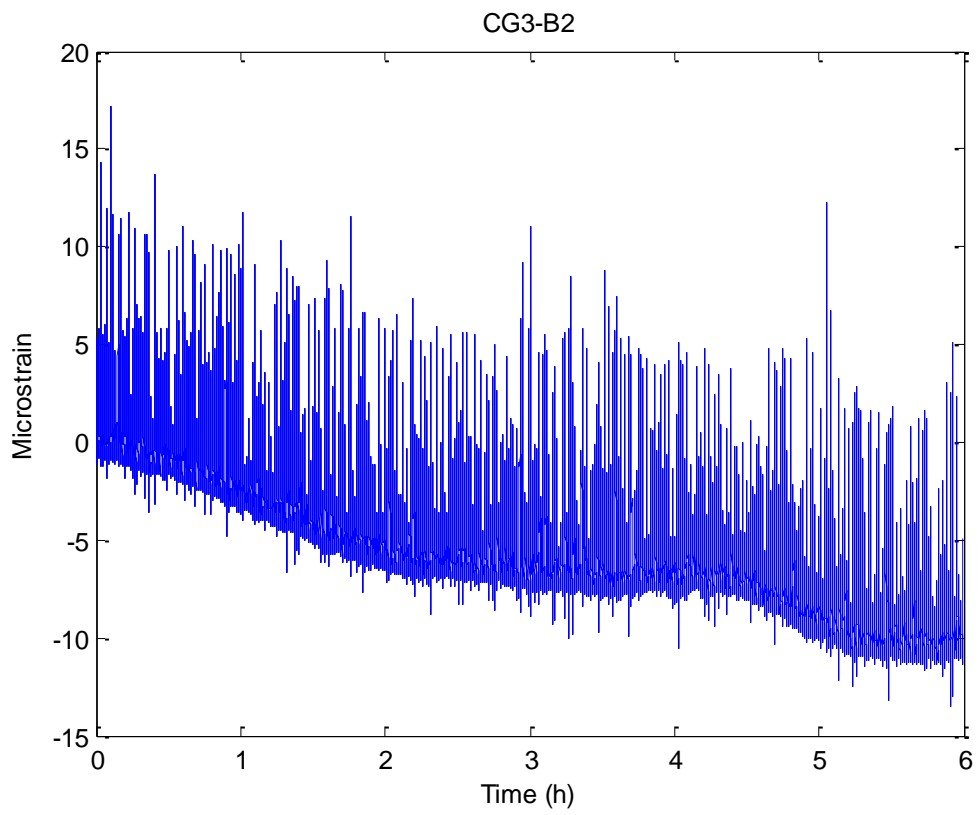
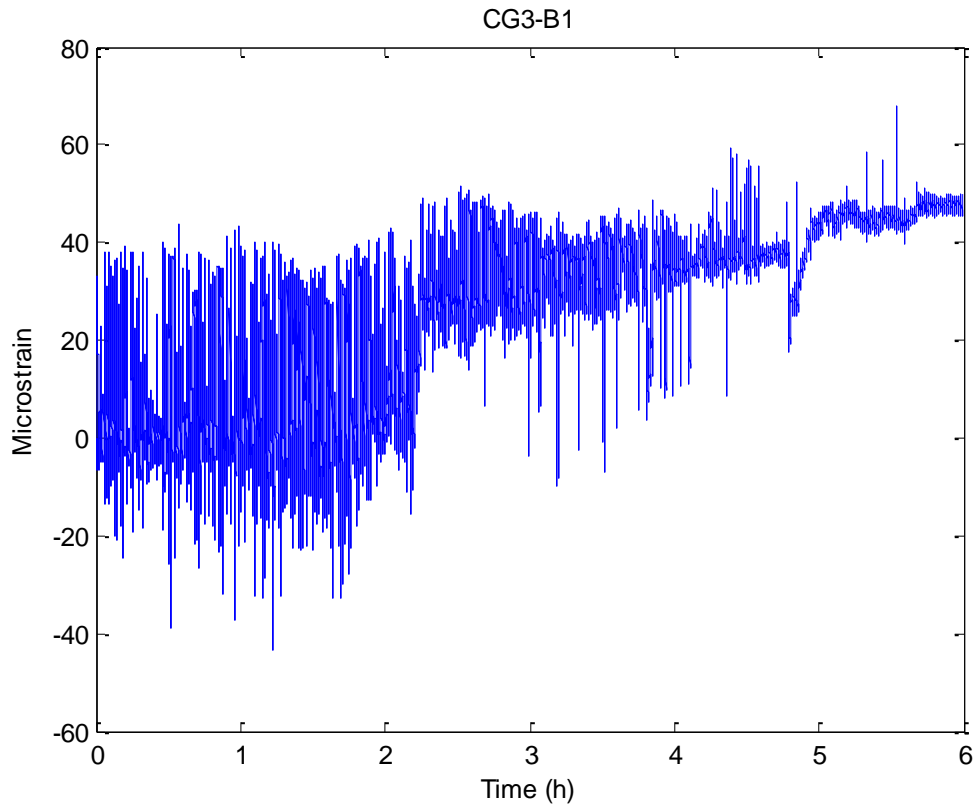


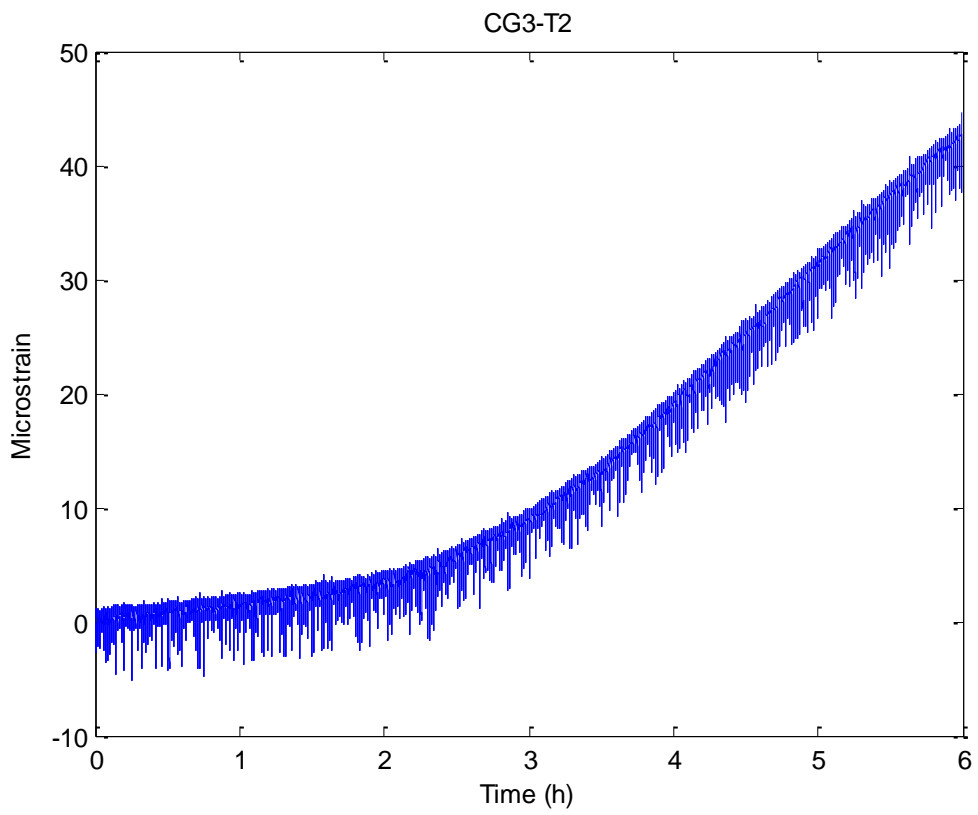
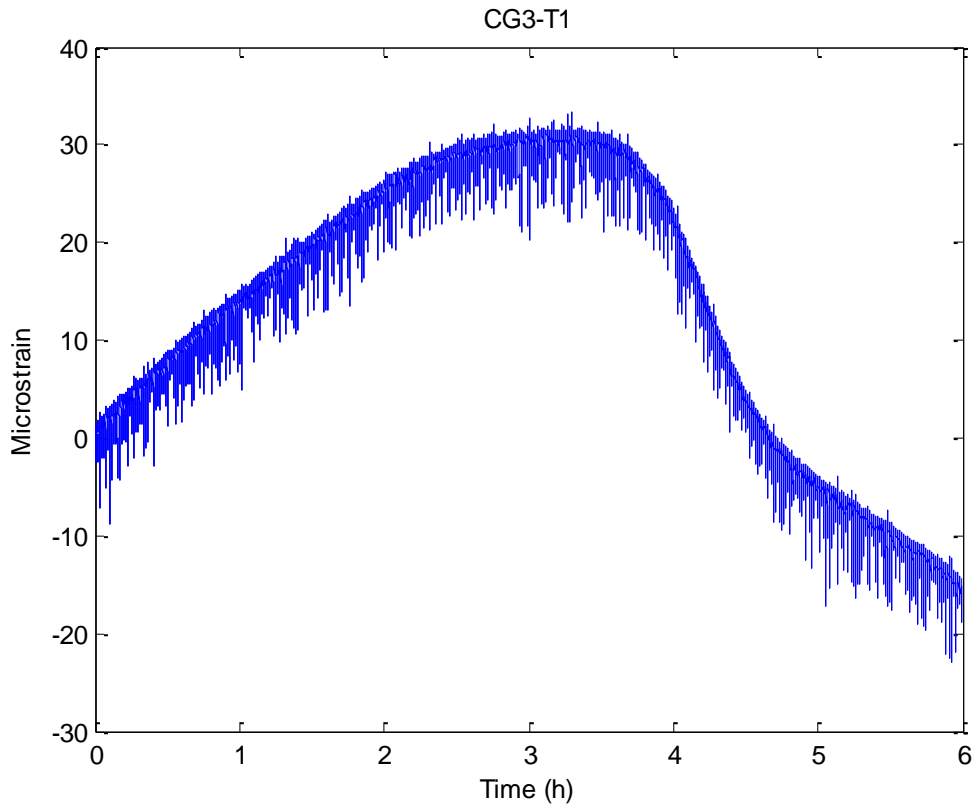


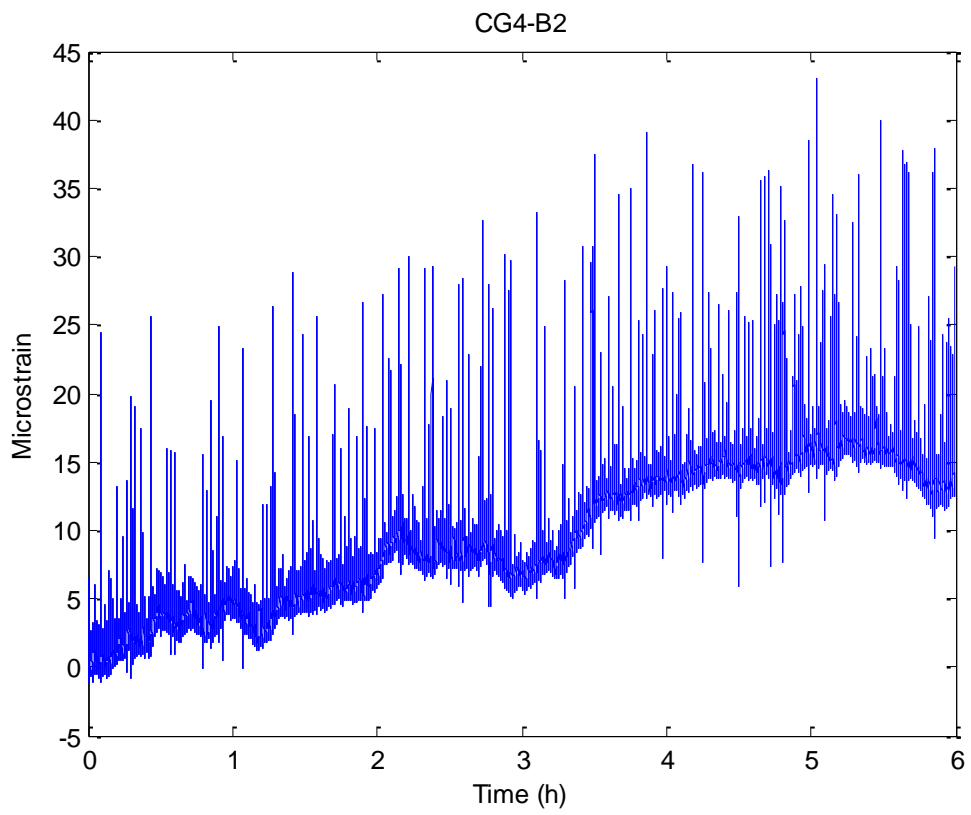
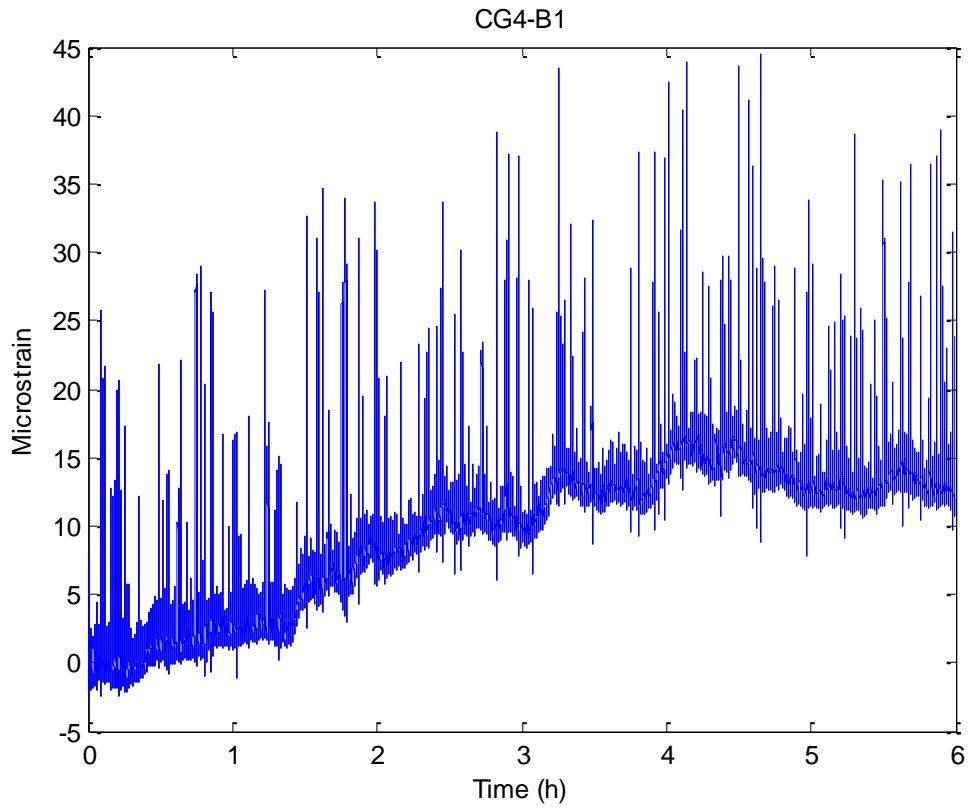


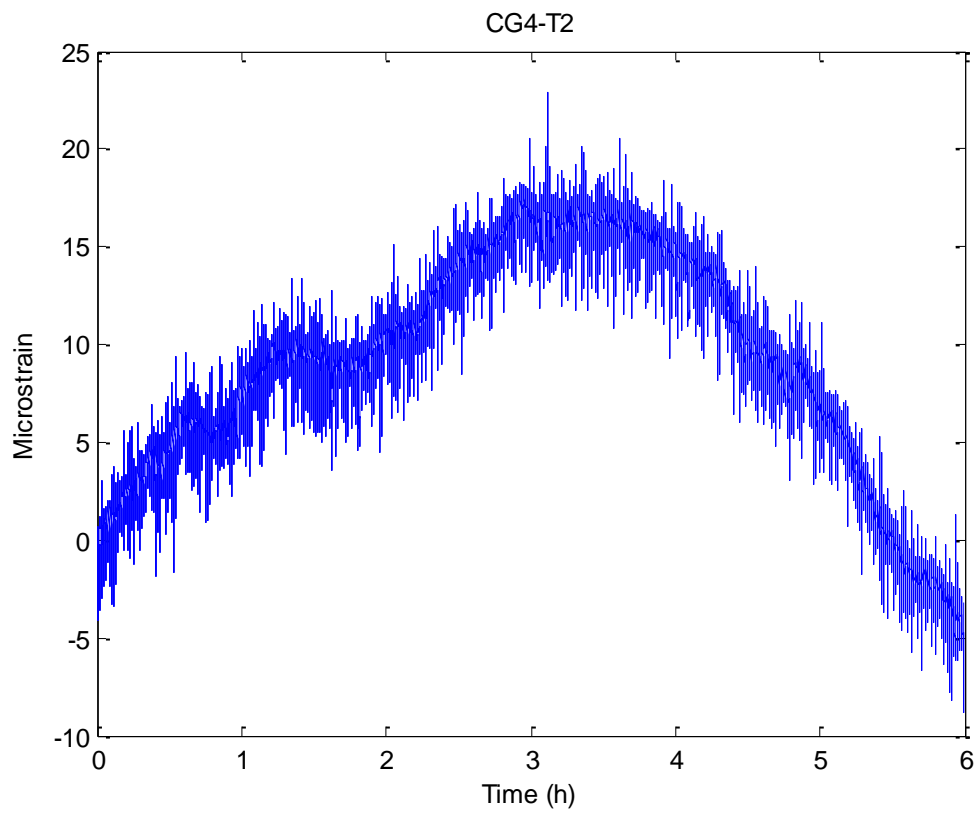
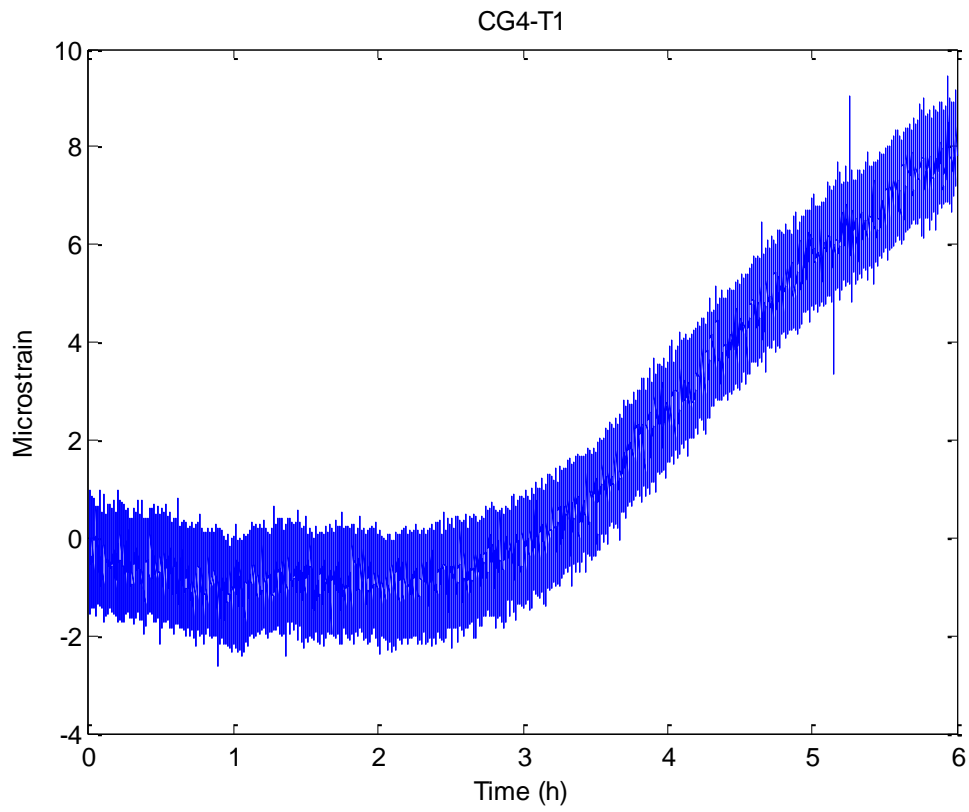


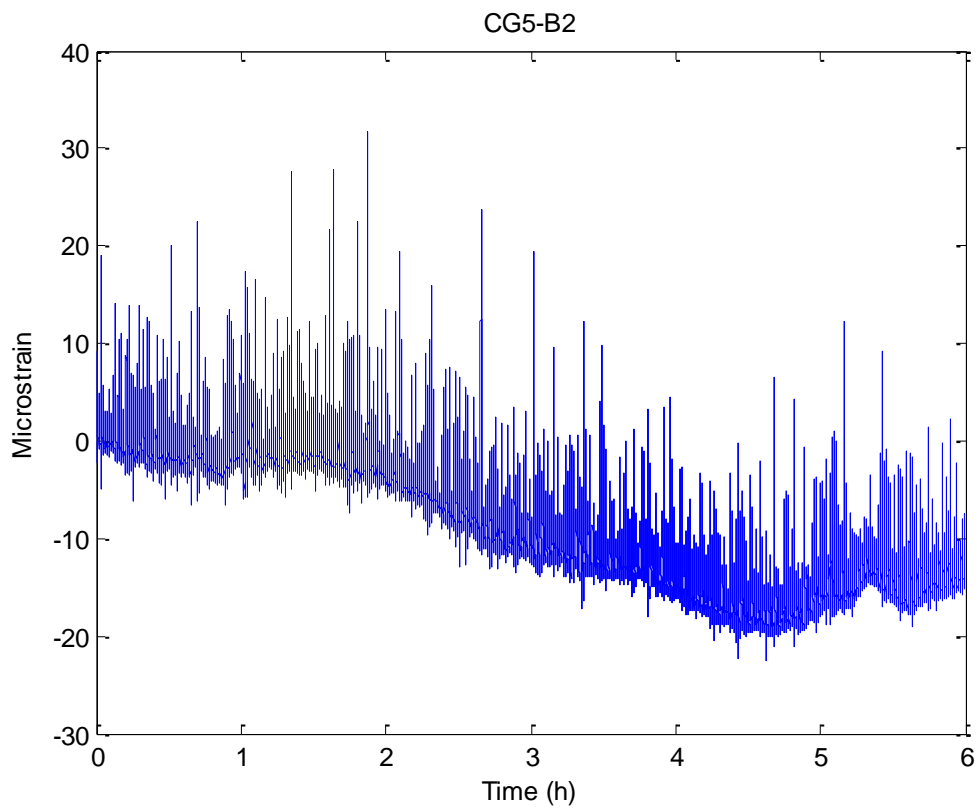
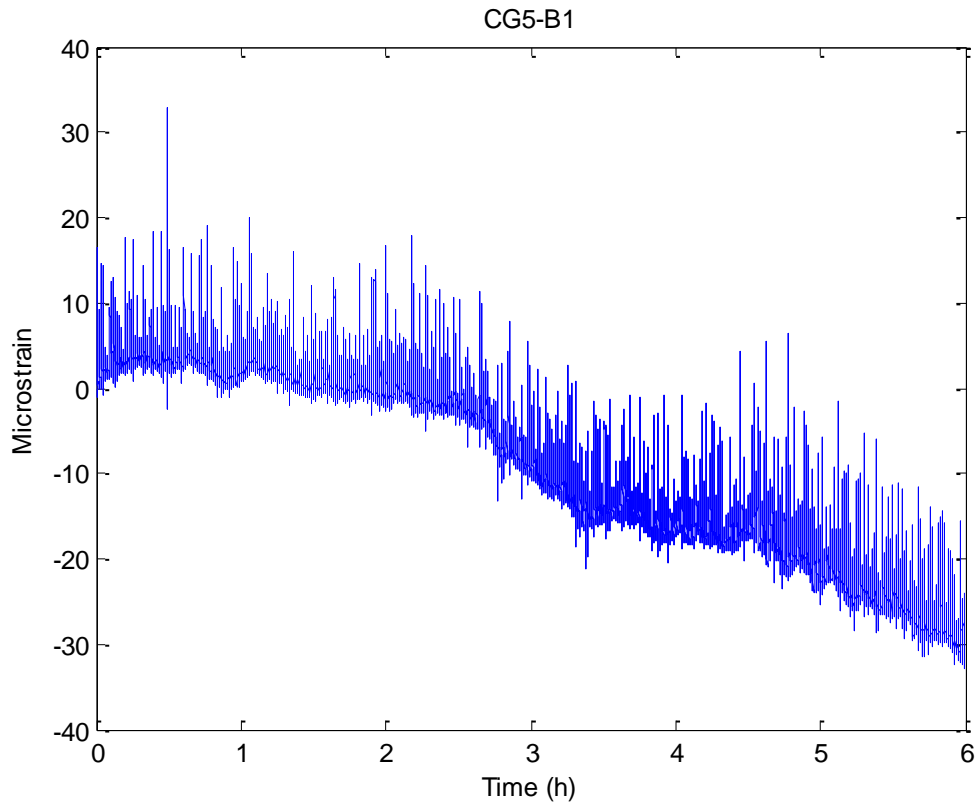


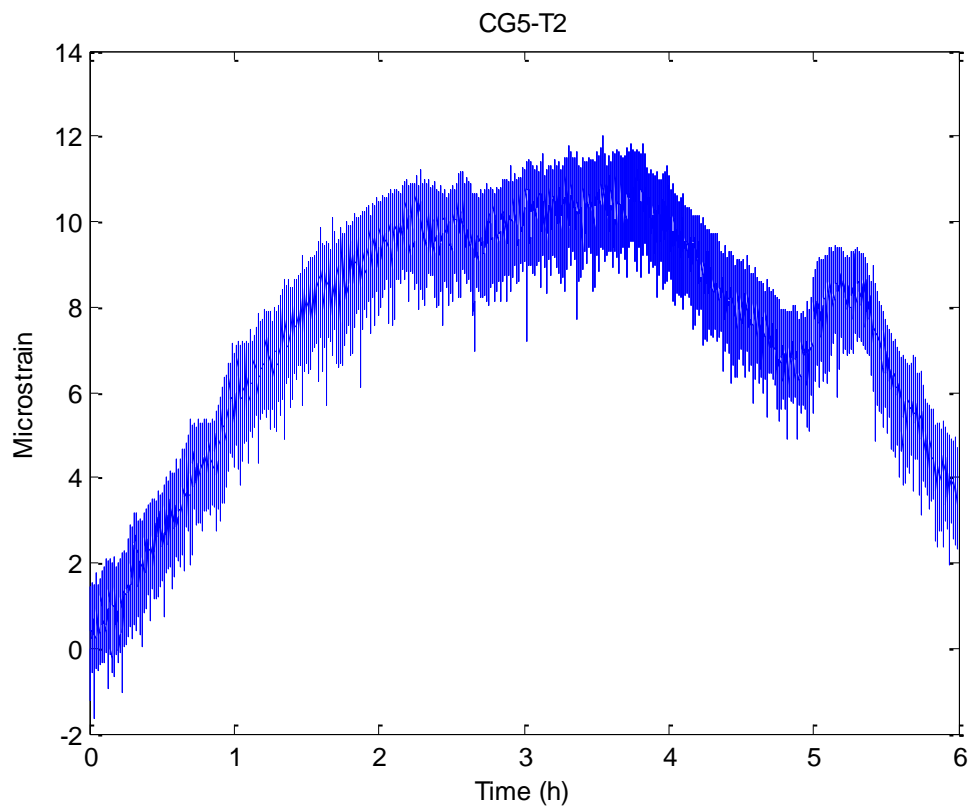
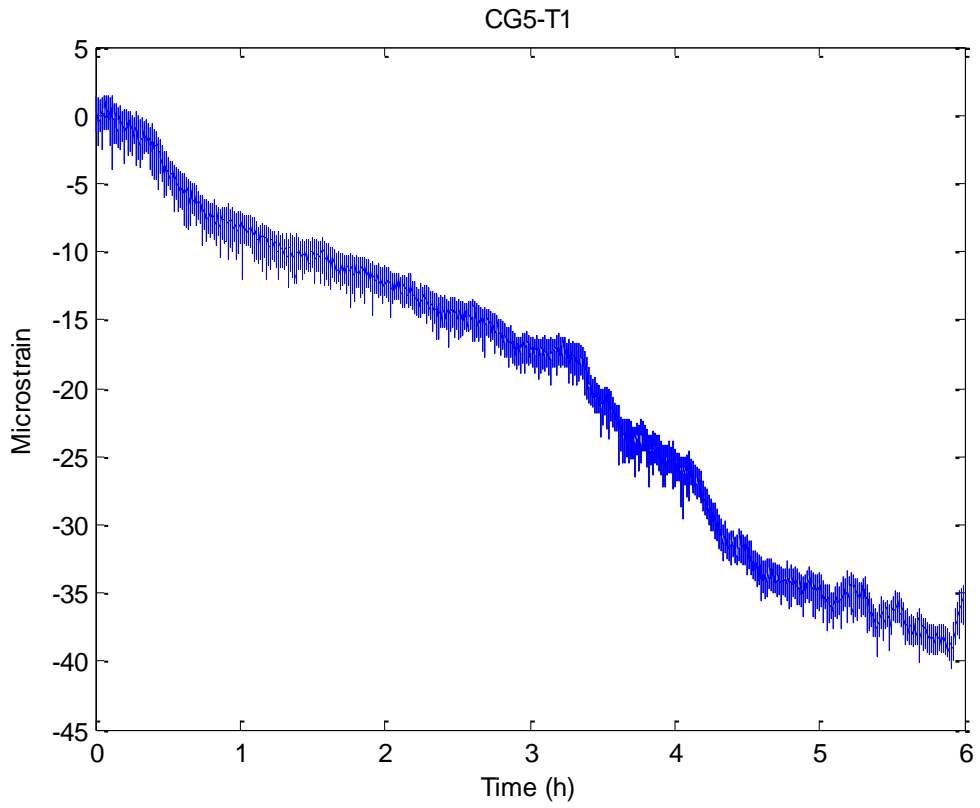


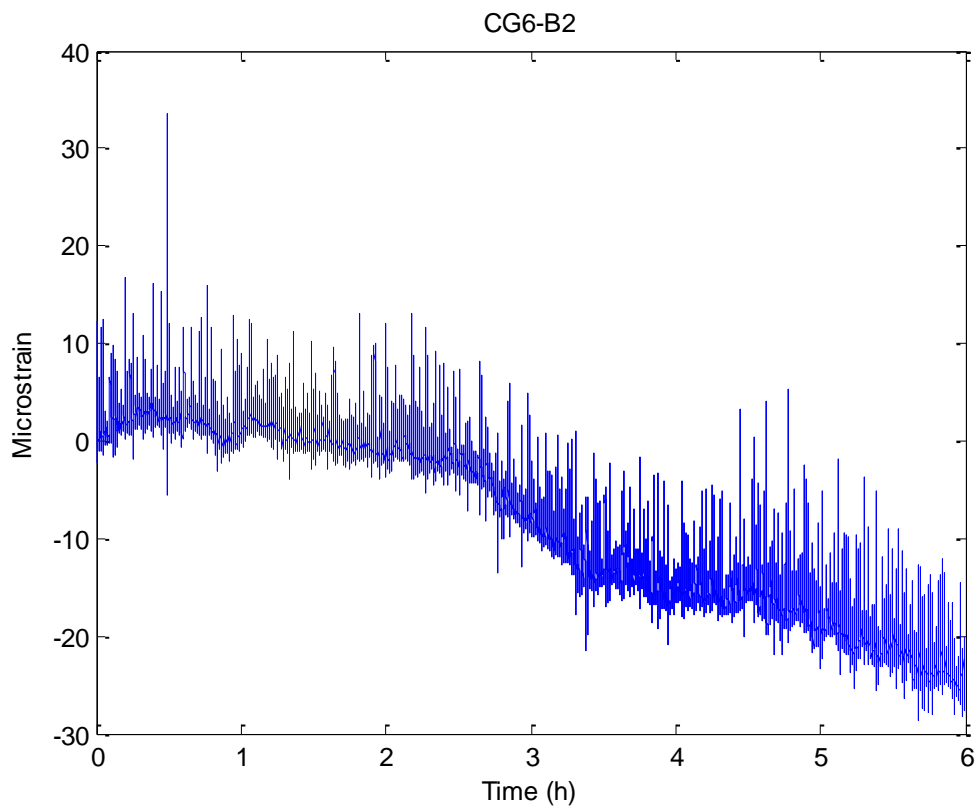
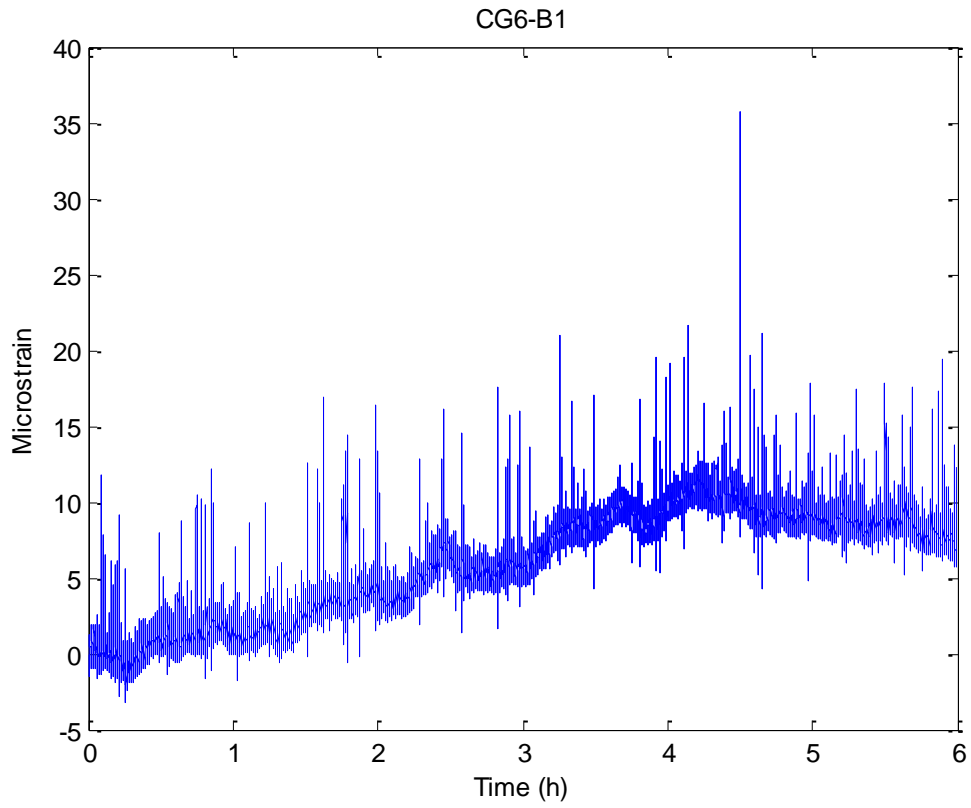


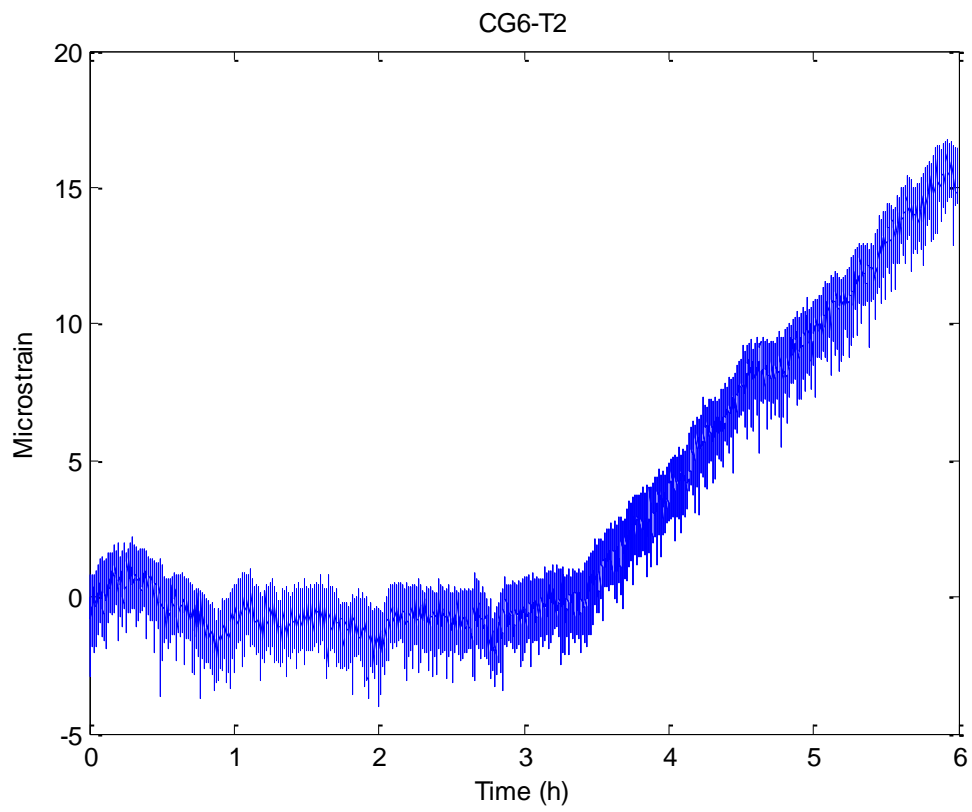
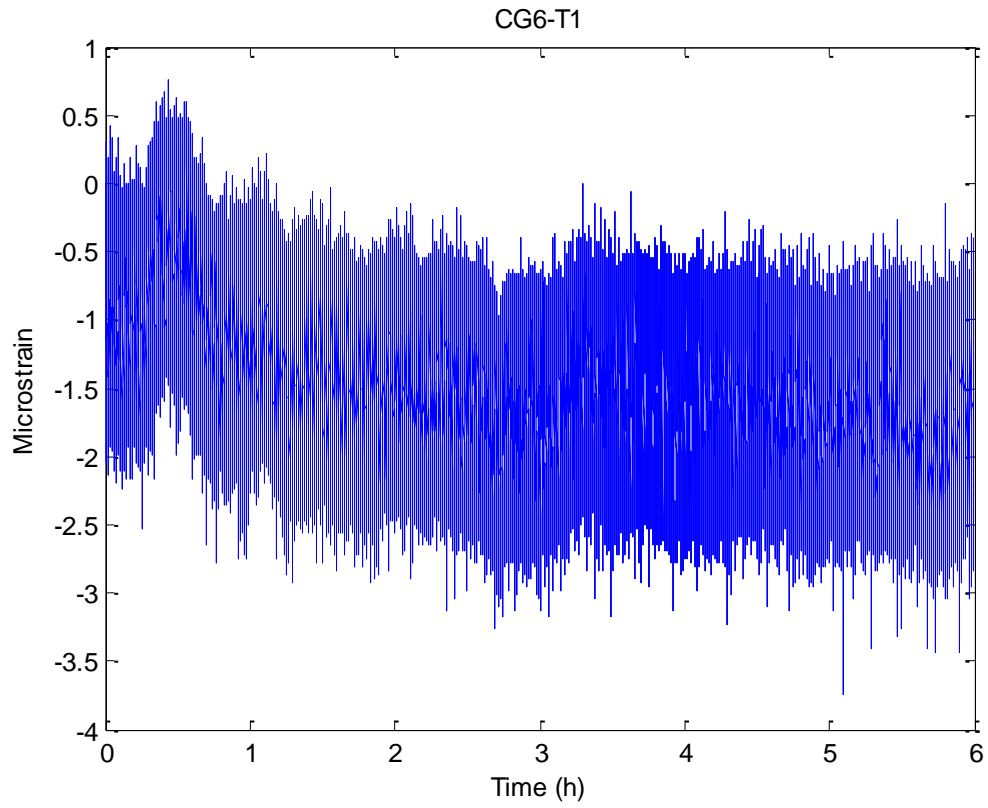








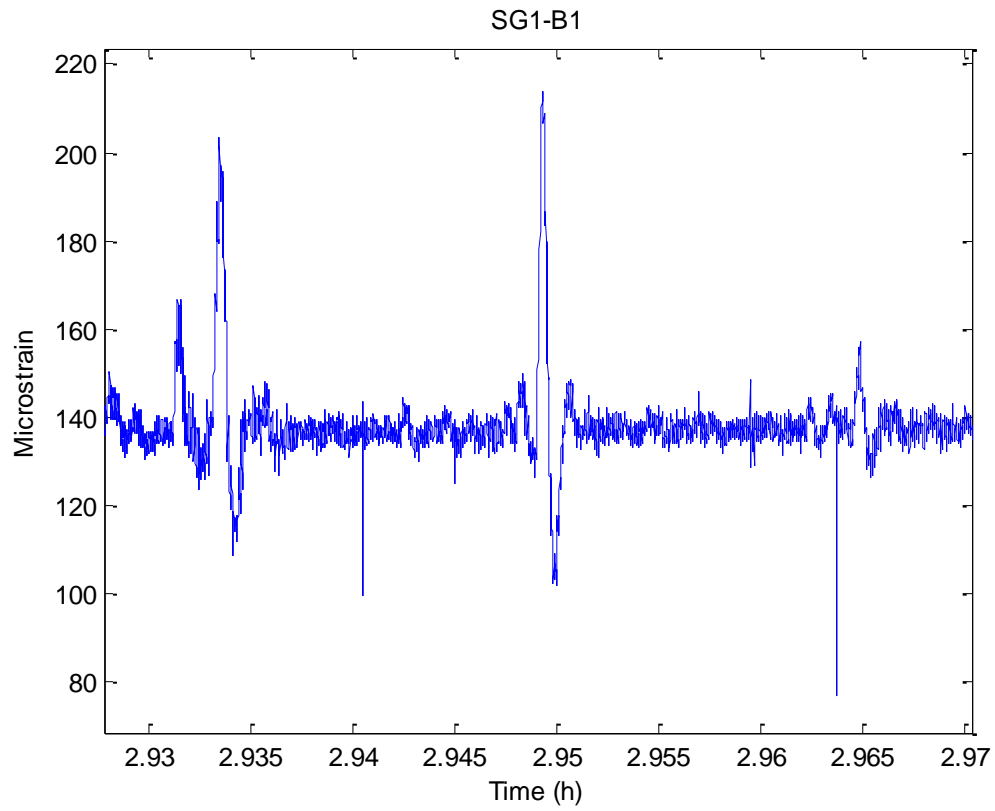


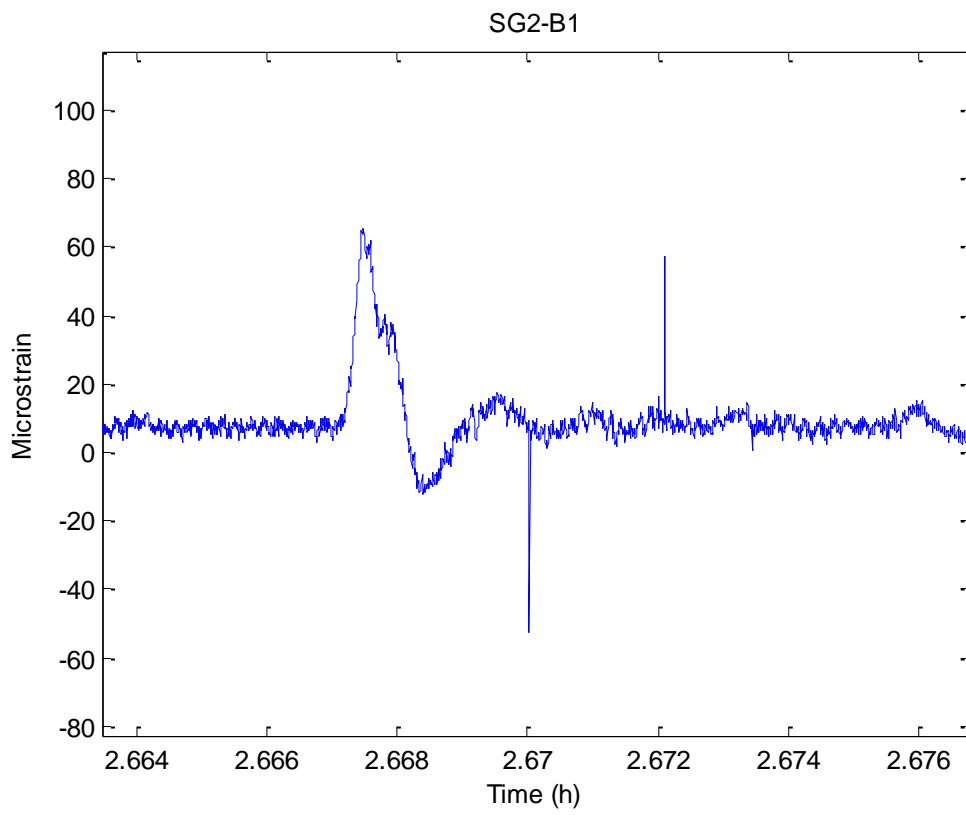
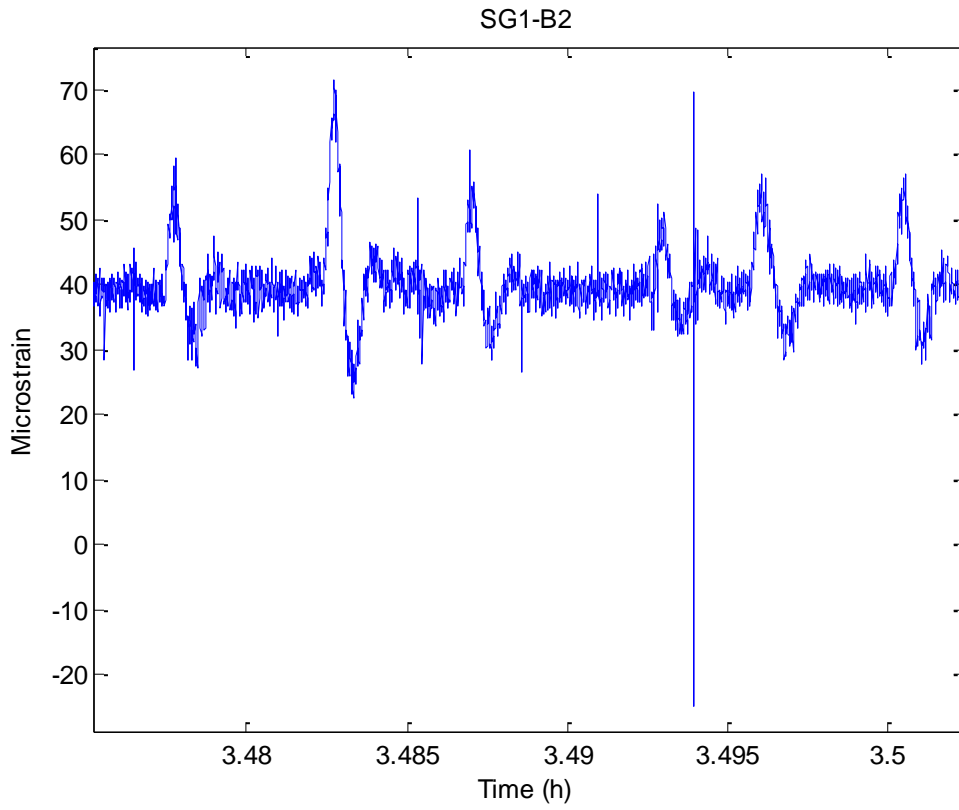


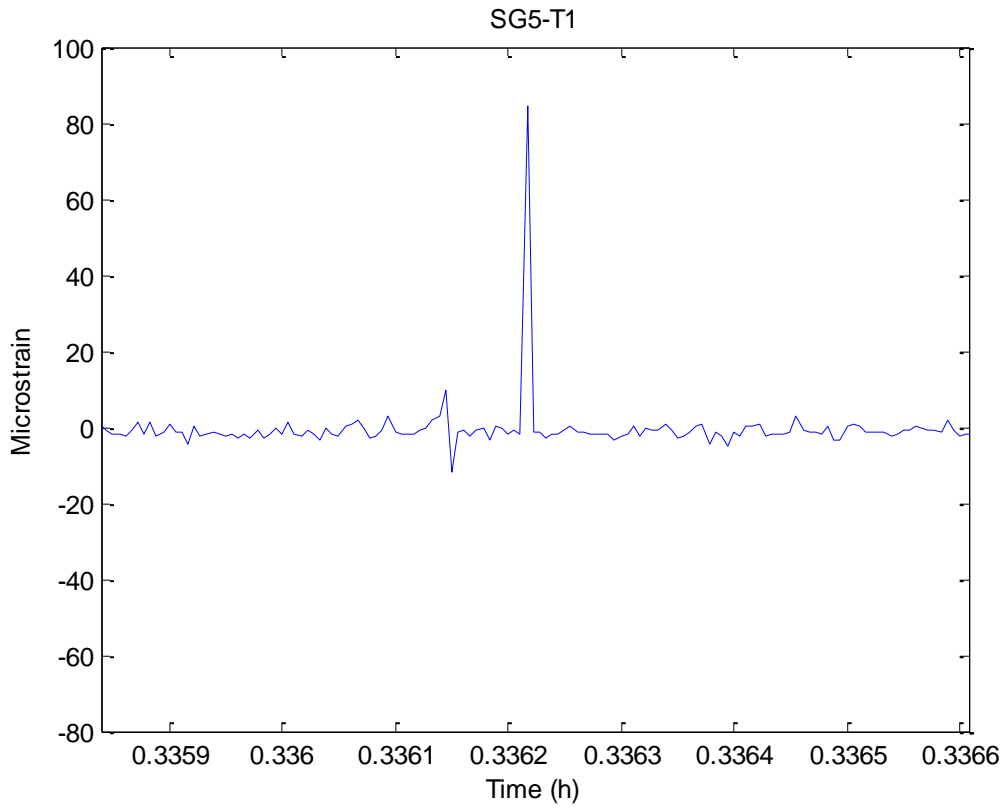
Signal issues

Unknown sharp peaks:

The peaks duration is much smaller than the peaks caused by truck crossing as can be shown from the figure below.







This public document is published at a total cost of \$250. 42 copies of this public document were published in this first printing at a cost of \$250. The total cost of all printings of this document including reprints is \$250. This document was published by Louisiana Transportation Research Center to report and publish research findings as required in R.S. 48:105. This material was duplicated in accordance with standards for printing by state agencies established pursuant to R.S. 43:31. Printing of this material was purchased in accordance with the provisions of Title 43 of the Louisiana Revised Statutes.